NNT : 2017SACLS019

Thèse de doctorat de l'Université Paris-Saclay préparée à l'Université Paris-Sud

Ecole doctorale n°579
Sciences mécaniques et énergétiques, matériaux et géosciences
Spécialité : Mécanique des fluides

par

M. Shreyas ACHARYA NEELAVARA

Numerical study of transition to turbulence in plane Poiseuille flow in physical space and state space

Thèse présentée et soutenue au LIMSI-CNRS, Orsay, le 18 Janvier 2017.

Composition du Jury :

M.	Jean-Christophe ROBINET	Professeur DynFluid Laboratory	President
M.	Uwe EHRENSTEIN	Professeur IRPHE	Rapporteur
M.	Carlo COSSU	Directeur de recherche IMFT	Rapporteur
M.	Christian TENAUD	Directeur de recherche LIMSI-CNRS	Examinateur
M.	François LUSSEYRAN	Directeur de recherche LIMSI-CNRS	Directeur de thèse
M.	Yohann DUGUET	Chargé de recherche LIMSI-CNRS	Co-encadrant de thèse

Contents

List of Figures

Abstract

This thesis numerically investigates the dynamics of turbulence in plane Poiseuille flow driven by a fixed pressure gradient. The focus is especially on computations carried out within the minimal flow unit (M.F.U.), a concept introduced by J. Jimenéz and P. Moin (1991) to unravel the dynamics of near-wall structures in the absence of outer large-scale motions.

In the first part, turbulent simulations are carried out in spatially periodic channels with large domain size, for a range of Reynolds numbers Re_τ. The turbulent regime features multiple pairs of streaks near both walls of the channel. Relevant statistics indicate that these solutions scale in inner units as expected for turbulent flows. Similarly, turbulent simulations are carried out in M.F.U.s for a wider range of Re_τ. In these simulations, the turbulent activity appears to be localised near one wall for considerable time durations, and the long term dynamics features abrupt reversals.

In the next part, we look numerically for exact coherent states in the M.F.U. system, extending the concepts from other shear flow studies. We compute edge states in M.F.U.s using bisection in order to investigate the boundary between the laminar and the turbulent regimes. A process of "quotienting" is carried out to reduce the continuous symmetries inherent to the system, leading to better visualisations in physical space. The edge states, visualised in physical space, typically exhibit a single pair of streaks along with streamwise vortices. For $Re_\tau \leq 80$ the energy signals of these states appear periodic, with the alternation between a calm and a bursting phase. The burst in energy is accompanied by a phase shift of the streaks in the spanwise direction. The streaks in these edge states are localised near only one wall at all times. Different state space representations and phase portraits were constructed using appropriately chosen variables. The dynamics along a turbulent reversal is organised around transient visits to a subspace of (almost) symmetric flow fields. Continuing our search for other exact coherent states in the system, we look for steady states and periodic orbits by recurrence analysis. A nearly-symmetric exact travelling wave (TW) solution was found. Stability analysis of the TW revealed that its unstable eigenvectors separate the state space into two symmetric basins.

In the last part of this thesis, the self-similarity of the different non-trivial equilibrium flow regimes computed in this work, is addressed. The r.m.s. velocity profiles of the turbulent solutions in the M.F.U.s, when appropriately averaged, are self-similar and scale in inner units. Contrarily to most studies focusing on symmetric solutions, the present study suggests that inner scaling is relevant for the description of edge regimes as well although the self-similarity is not as satisfactory as for the turbulent regimes.

Key words : turbulence, plane channel, transition, exact coherent structures

Résumé

Cette thèse contient une étude numérique des régimes turbulents au sein d'un écoulement de Poiseuille plan forcé par un gradient de pression constant. L'accent est porté sur le concept d'unité minimale introduit par J. Jimenéz et P. Moin afin d'étudier la dynamique des structures cohérentes de proche paroi en l'absence des structures à plus grande échelle.

Dans une première partie, des simulations en régime turbulent ont été conduites dans une géométrie périodique, pour de grands domaines de calcul et pour plusieurs valeurs du nombre de Reynolds Re_τ. Les régimes associés sont caractérisés par des paires de stries à proximité des parois. L'analyse statistique révèle une loi d'échelle basée sur les unités de paroi. De la même façon, les simulations turbulentes ont été conduites dans une unité minimale pour une plus grande gamme de valeurs de Re_τ. Initialement, les statistiques dans ce cas indiquent que ces solutions ne semblent pas respecter les lois de similitudes, que ce soit en utilisant les unités de paroi ou les unités rapportées aux dimensions du système (unités extérieures). La cause de ce comportement réside dans la convergence des statistiques. En effet, dans ces simulations, l'activité turbulente est localisée alternativement à proximité d'une des parois, et la dynamique à temps long s'organise donc autour de renversements abrupts entre ces deux positions. C'est pourquoi, des variables basées sur la symétrie ont été définies permettant d'identifier la localisation des structures turbulentes à chaque instant sur l'une ou l'autre des parois. Les moyennes conditionnelles basées sur les variables de symétrie convergent et permettent de retrouver les lois de similitudes des profiles exprimés en lois de paroi comme attendu.

Dans la deuxième partie on cherche des solutions exactes des équations pour des calculs en unité minimale, en se basant sur les concepts utilisés pour d'autres écoulements cisaillés. Des états dits de frontière (*edge states*) ont été ainsi trouvés par une méthode de dichotomie, qui par application répétée permet de converger vers une solution particulière, ni laminaire ni turbulente. Une technique de quotientage a été developée pour réduire les symétries continues du système, technique indispensable pour révéler la continuité temporelle et spatiale de ces solutions. Ces états de frontière, visualisés dans l'espace physique, sont caractérisés par une unique paire de stries et de tourbillons longitudinaux. Pour $Re_\tau \leq 80$, leur dynamique est périodique en temps, avec l'alternance entre une phase calme et une phase active. Ces stries sont toujours localisées à proximité d'une seule paroi. Des représentations et portraits dans l'espace des phases sont reconstruits à l'aide de divers observables. En particulier le choix des variables de symétrie pour la représentation dans l'espace des état apparaît révéler au mieux la physique de l'écoulement. La dynamique d'un renversement s'articule autour de visites transitoires à un espace de solutions quasi-symétriques. La recherche de solutions exactes de type stationnaire ou periodique est effectuée par une analyse de récurrences. Une onde progressive exacte, instable et quasi-symetrique a ainsi été identifiée. L'analyse de stabilité

révèle que ses vecteurs propres séparent l'espace des phases en deux basins distincts.

La dernière partie remet en question l'auto-similarité des différents régimes d'équilibre de l'écoulement. La plupart des études se sont concentrées jusqu'à présent sur la recherche de solutions en gardant les dimensions du domaine de calcul fixes en termes d'unités extérieures, alors que dans ce travail les dimensions du domaine de calcul sont aussi conservées, mais en termes d'unités de paroi. Contrairement aux études récentes qui se concentrent sur des solutions à structure symétrique imposée, nos résultats suggèrent que les unités de parois sont également pertinentes pour les états de frontière lorsqu'ils sont localisés près d'une paroi, même si l'auto-similarité n'est pas aussi flagrante que pour les régimes turbulents.

Mots-clés : turbulence, canal plan, transition, structures cohérentes exactes

Chapter 1

Introduction

1.1 Motivation

The motion of a fluid, known as flow can be broadly categorised as being laminar or turbulent. The orderly flow of fluid in parallel layers, is known as laminar flow whereas chaotic unpredictable motion of a fluid is known as turbulence. Most flows observed in nature are turbulent. How does the flow which is smooth and orderly undergo a change to chaotic flow? This is a question that has intrigued researchers for a very long time. In his seminal paper of 1883 titled "*An Experimental Investigation of the Circumstances Which Determine Whether the Motion of Water Shall Be Direct or Sinous, and of the Law of Resistance in Parallel Channels*", Reynolds [2] addressed the question of why a fluid flow (seeded with a colored dye for the sake of visualisation) in a pipe driven by a pressure gradient changes from a laminar state to a turbulent one. Shown below in Fig. 1.1 are two sketches from [2] representing the laminar flow where Reynolds observed a single streak of dye and the turbulent flow where the dye was mixed with the surrounding fluid and spread throughout the domain.

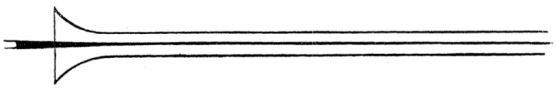

(a) Laminar flow : "Streak of colour extended in a beautiful line" [2]

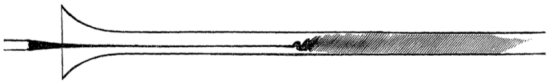

(b) Turbulent flow : "Colour band would all at once mix up with surrounding water, and fill the rest of the tube with a mass of coloured water" [2]

Figure 1.1: Sketches from the paper by Reynolds in 1883 [2] showing the different ways the dye was distributed in (a). laminar flow and (b). turbulent flow

"French physicist Jean Poiseuille [18] [19] studied the resistance of a fluid when flowing through a circular pipe in small capillaries and thereby concentrated unwittingly on the steady unidirectional laminar flow invariably realized." [20]

In different types of flows, is turbulence sustained indefinitely once it is achieved, or does the flow revert back to being laminar eventually? What are the conditions under which turbulence is sustained? Are laminar flow and turbulence necessarily two separate flow regimes, or do they co-exist? These are some of the questions that have motivated researchers for a long time and they form the broad motivation for this thesis as well.
More specifically, we are interested in flows which are bounded by walls also known as wall-bounded shear flows, for example, the flow in a channel, the flow in a pipe etc., and the transition to turbulence and relaminarisation in this context. The study of transition to turbulence in wall-bounded fluid flows also has a lot of practical applications, some of them being the transport of oil in pipelines, the transport of blood in arteries etc... Fig. 1.2 contains the Moody chart which shows the relation between the Darcy-Weisbach friction factor f_D (the normalised pressure loss in a pipe), and the Reynolds number of the flow Re. Re, which represents the ratio of inertial forces to the viscous forces in the fluid is the governing parameter of the flow.

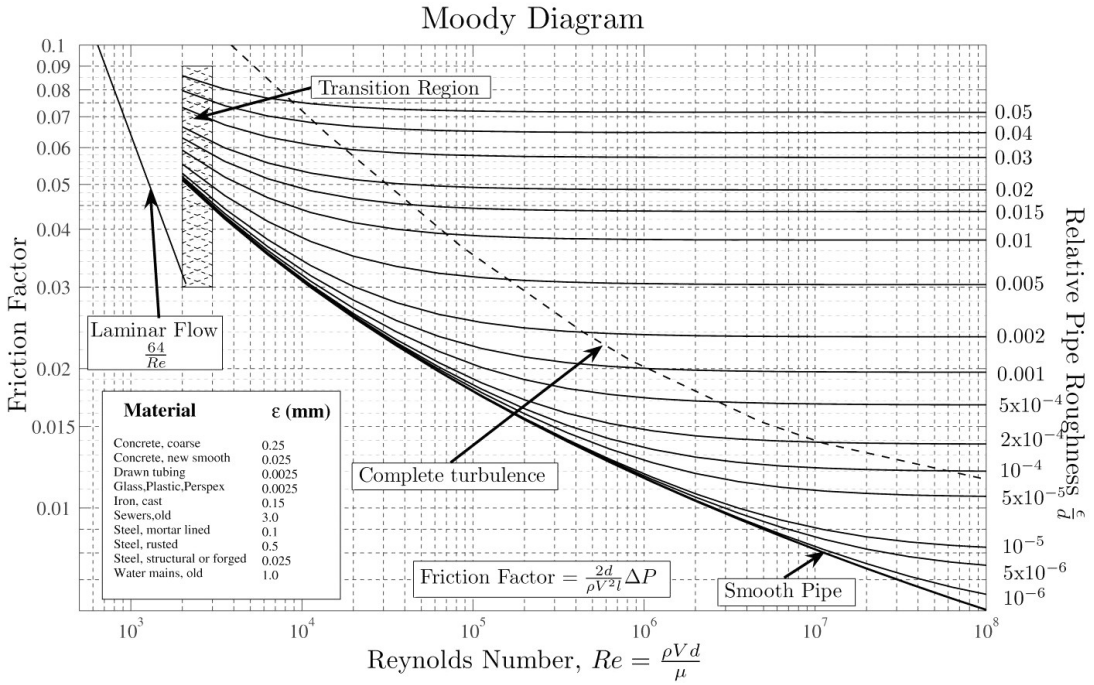

Figure 1.2: Moody diagram showing the plots of f_D vs Re for pipe flow, taken from the work of S.Beck and R.Collins, University of Sheffield

When the flow driven by a fixed mass flux undergoes a transition from laminar flow to turbulence, the state of the flow changes from being on the solid line to the left in the plot (which represents the laminar flow) to the turbulent curve on top at the same Re. Hence, there is a huge increase in the friction factor, indicating that there is a large pressure drop associated with the transition to turbulence, hence more energy is needed to transport the same amount of fluid in turbulent flow. Correspondingly, if a flow driven by a fixed pressure gradient undergoes transition to turbulence, there is a drop in the flow rate, and again more energy has to be spent in transporting the fluid as compared to the laminar case. In general, the transport of fluid is more costly in the turbulent regime than in the laminar regime. This makes the transition an interesting field of study for applications like the oil industry where oil has to transported over large distances in pipelines (as it

is in their interest to minimise energy losses due to turbulence). It has to be noted that these curves are obtained taking into effect the roughness of the wall as a factor whereas in our study, we do not consider a wall roughness (a perfectly smooth wall is assumed) and curvature/entrance effects (a fully developed flow is considered).

1.2 Plane Poiseuille flow

We consider the plane Poiseuille flow which is the flow of a fluid in a channel driven either by a fixed mass flux or a uniform pressure gradient imposed in the streamwise direction. A schematic of the flow is shown in Fig. 1.3

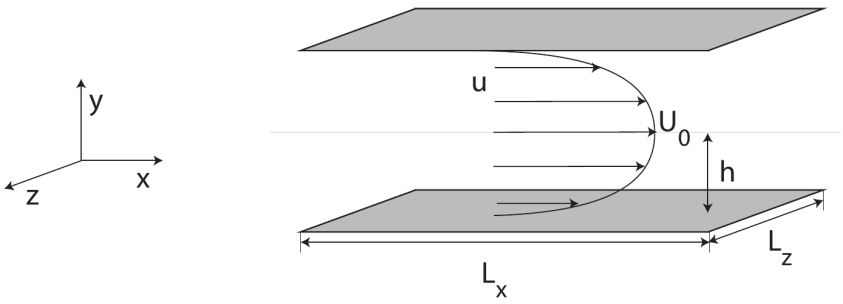

Figure 1.3: A schematic representing the channel in which the flow is driven in the streamwise (x) direction

A pressure gradient $-dP/dx$ is imposed in the streamwise direction which gives rise to a flow $\boldsymbol{u} = (u, v, w)$, where u, v and w represent the streamwise, wall-normal and spanwise components of the full velocity field $\boldsymbol{u}$ respectively. The streamwise and spanwise extent is infinite and walls are located at $y = \pm h$.
The flow of a viscous incompressible Newtonian fluid is governed by the Navier-Stokes equations,

$$\frac{\partial \boldsymbol{u}}{\partial t} + (\boldsymbol{u} \cdot \nabla)\boldsymbol{u} = -\frac{1}{\rho}\nabla \boldsymbol{p} + \nu \nabla^2 \boldsymbol{u} \tag{1.1}$$

$$\nabla \cdot \boldsymbol{u} = 0 \tag{1.2}$$

where $\boldsymbol{p}$ represents the pressure of the system, ρ the density and ν the kinematic viscosity of the fluid. We consider that the fully developed laminar base flow in a channel is

- steady, i.e. $\dfrac{\partial \boldsymbol{u}}{\partial t} = 0$
- independent of the spanwise co-ordinate, i.e. $\dfrac{\partial \boldsymbol{u}}{\partial z} = 0$
- unidirectional in the streamwise direction, i.e. $\boldsymbol{u} = u\boldsymbol{e}_x$ (a consequence of the continuity equation) ,

The Eqns. 1.1 and 1.2 reduce to

$$\begin{pmatrix} \frac{1}{\rho}\frac{\partial p}{\partial x} \\ \frac{\partial p}{\partial y} \\ \frac{\partial p}{\partial z} \end{pmatrix} = \begin{pmatrix} \nu\frac{\partial^2 u}{\partial^2 y} \\ 0 \\ 0 \end{pmatrix} \tag{1.3}$$

$$\frac{\partial u}{\partial x} = \frac{\partial v}{\partial y} = \frac{\partial w}{\partial z} = 0. \tag{1.4}$$

This means that the pressure force driving the flow is being balanced by the volumetric viscous force represented by the right hand side of the Eqn. 1.3 when the flow is steady. Since we have a uniform pressure gradient, the term on the left hand side of Eq. 1.3 is constant, thereby also making the term on the right hand side a constant.
Integrating Eqn. 1.3 and applying the no-slip boundary conditions at the wall $\boldsymbol{u}_{|walls} = 0$ i.e. $\boldsymbol{u}_{|\pm h} = 0$ and with the imposed pressure gradient $dp/dx < 0$, we get the laminar flow profile of the plane Poiseuille flow pointing in the $x > 0$ direction :

$$\begin{pmatrix} u \\ v \\ w \end{pmatrix} = \begin{pmatrix} U_{cl}(1 - y^2/h^2) \\ 0 \\ 0 \end{pmatrix} \tag{1.5}$$

where U_{cl} is the centreline velocity representing the maximum velocity of the laminar parabolic profile occuring at $y = 0$. U_{cl} is related to $\frac{dp}{dx}$ as

$$U_{cl} = -\frac{dp}{dx}(\frac{h^2}{2\mu}), \tag{1.6}$$

μ being the dynamic viscosity of the fluid.

1.3 Coexistence of laminar and turbulent regimes

The profile of the laminar flow in the channel geometry is given in Eqn. 1.5. But we also know from experiments about the existence of turbulence in channels. The existence of several solutions for the same problem means that the coexistence of different flow regimes in the same domain is also possible. Some of the simplest structures that represent this coexistence of laminarity and turbulence in the same domain are called 'spots'. These spots are spatially localised zones of turbulence. They can grow in size and contaminate the entire domain leading to fully turbulent flow. Some of the visualisations and plots of the earlier experimental and numerical computations are included in this section.
Fig. 1.4 shows the formation of a spot in an experimental study of transition to turbulence in plane Poiseuille flow by Carlson *et al.* [3] in 1982. They used water as the working fluid in a channel which was $4.10m$ long, had a wall-normal depth (2h) of $0.006m$ and a cross-section of $0.8m$ (an aspect ratio of around 133) at $Re = 1000$. Oblique waves were observed at the spanwise tips of the turbulent spot which developed at Re far below a threshold known as critical Reynolds number Re_c which is explained in detail in section 1.4. The spot development along the direction of its propagation is illustrated in the visualiasations in Fig. 1.4. Fig. 1.4 (a) shows the presence of a region of small scale

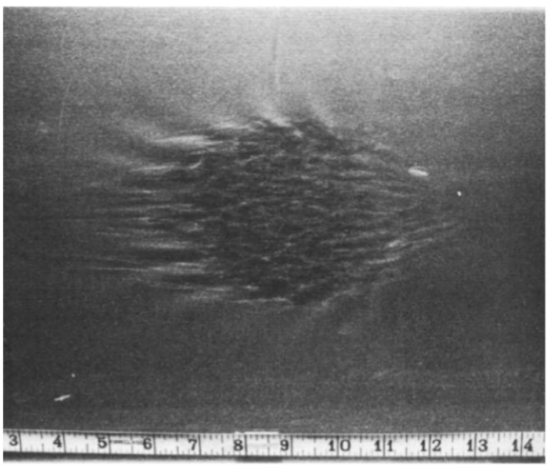

(a) Spot at $x/h = 50$

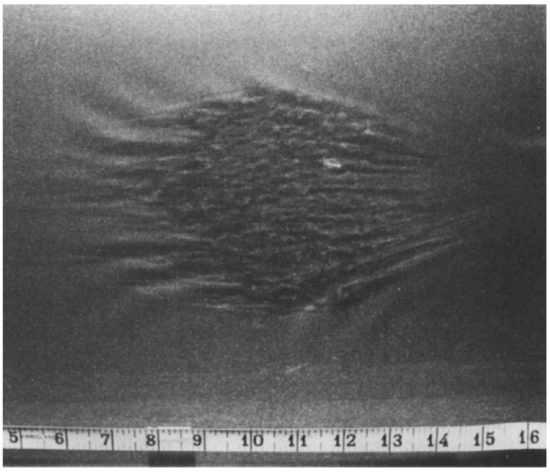

(b) Spot at $x/h = 64$

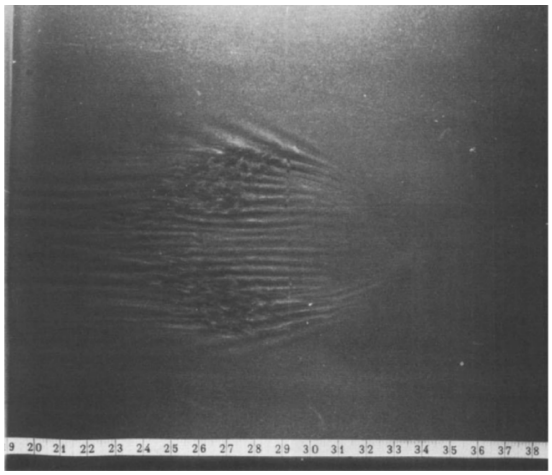

(c) Beginning of spot splitting at $x/h = 132$

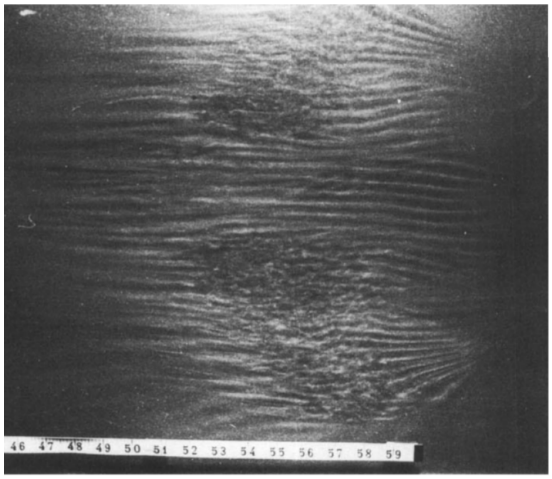

(d) Spot at $x/h = 260$

Figure 1.4: Visualisations of the xz plane showing the stages of spot formation and breakdown leading to turbulence as observed by Carlson *et al.* [3] in plane Poiseuille flow in a channel of domain size $4.10m \times 0.006m \times 0.8m$ at $Re = 1000$

turbulence, streaks and oblique waves; 1.4 (b) shows much stronger oblique waves; 1.4 c.) shows the turbulent spot further downstream. In Fig. 1.4(c) the region of small scale turbulence with the longitudinal streaks and the waves are clearly seen, but the front tip is not so clearly visible. Finally in 1.4 (d), we see the presence of two spots separated by a set of longitudinal streaks, leading to the spread of turbulence in the domain.
Alavyoon *et al.* [4] carried out experiments in a channel which was $2m$ long, $0.83m$ wide and with a channel height (2h) of either $0.003m$ or $0.005m$ thereby having an aspect ratio of either 277 or 166, with an aim to extend the Re range of the study by Carlson *et al.* [3] to higher Re and to obtain data on essential spot features, such as spreading rate and propagation velocities. Fig. 1.5 shows the visualisation of the spot in their channel.

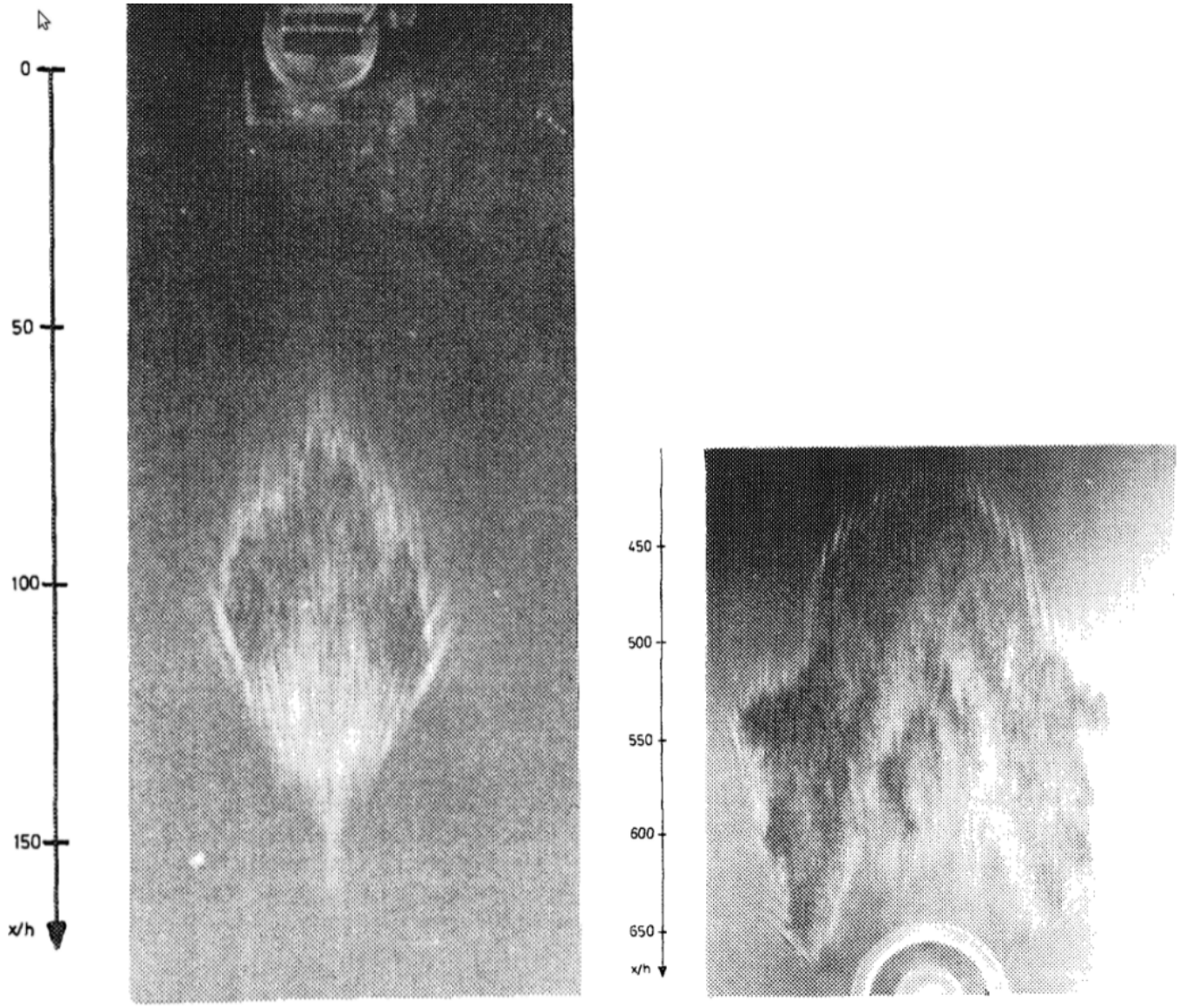

Figure 1.5: Visualisations of the turbulent spot as observed by Alavyoon *et al.* [4] in plane Poiseuille flow in a channel of domain size $2m \times 0.003m \times 0.83m$ for $Re = 1650$ (a) close to the triggering, (b) at the downstream end of the channel.

The demarcation between the turbulent and the laminar flow was clearly distinguished. Sano and Tamai [5] considered a channel of dimensions $2352h \times 2h \times 360h$ where the wall-normal depth is $2h = 5mm$ for their experiments in plane Poiseuille flow. As opposed to earlier experiments by Carlson [3] and Avila [21] where the turbulent spots were obtained by local perturbations, Sano and Tamai obtain turbulent flow through continuous injection at the inlet. Their considerably larger domain size with large aspect ratio allows them to visualise spots in their flow down to $Re = 798$, with the typical size of the spots being about $40 - 80h$. Fig. 1.6 shows the schematic of their experimental set up, and the spots observed by them in their flow.

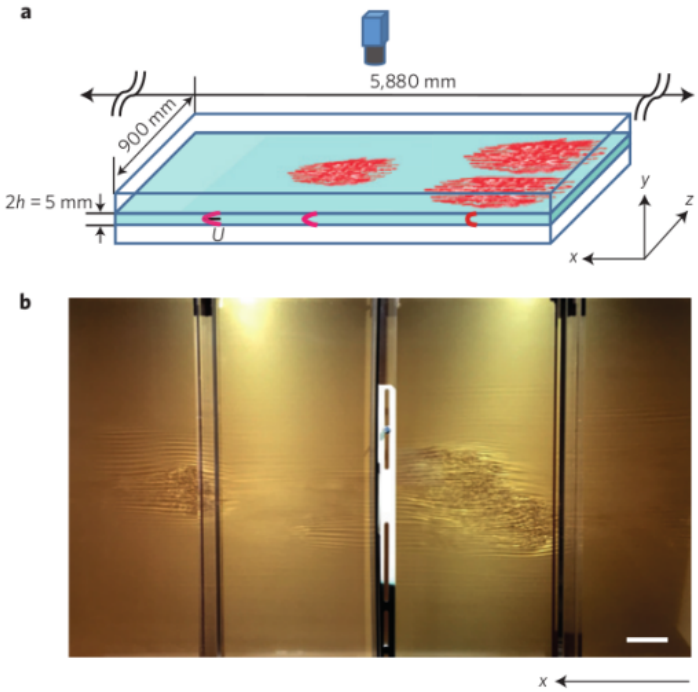

Figure 1.6: (a)The schematic of the experimental set up of plane Poiseuille flow by Sano and Tamai [5] consisting of a channel of dimensions $2352h \times 2h \times 360h$ with $2h = 0.005m$ and (b) the turbulent spots observed in their flow at $Re = 810$

Most of the turbulence injected at the inlet decay quickly to laminar flow, and the surviving turbulence is visible as localised turbulent spots characterised by finer-scale disordered eddies surrounded by several streaks and laminar flow. For lower Re, $Re \simeq 798$, turbulent spots decayed as they propagate with the mean flow, but at higher Re, $Re \geq 830$ splitting and spreading of spots was observed leading to turbulent clusters. For sufficiently large values of Re, $Re > 900$, turbulent flow was sustained. In Fig. 1.6, the laminar-turbulent interface of the spots appear oblique with respect to the streamwise direction, and resembles stripes. Stripes have been observed in channel flows by Tsukahara *et al.* [22], in plane Couette flow by Duguet *et al.* [23] and in Kolmogorovian flows by Chantry *et al.* [24].

Coming back to spots in channel flow, Lemoult *et al.* [6] performed experiments in a channel of much smaller aspect ratio whose dimensions are $220h \times 2h \times 15h$ where the half-height, $h = 10mm$, where they concentrate on the large-scale flow surrounding a turbulent spot in the flow. They speculate on the presence of a travelling-wave (TW) like

structure close to the trailing edge of the spot. They have access to the all the velocity components in a plane and make 3D stereoscopic PIV visualisations. The spot and a zoom on the TW-like structure are shown in Fig. 1.7 and 1.8, respectively.

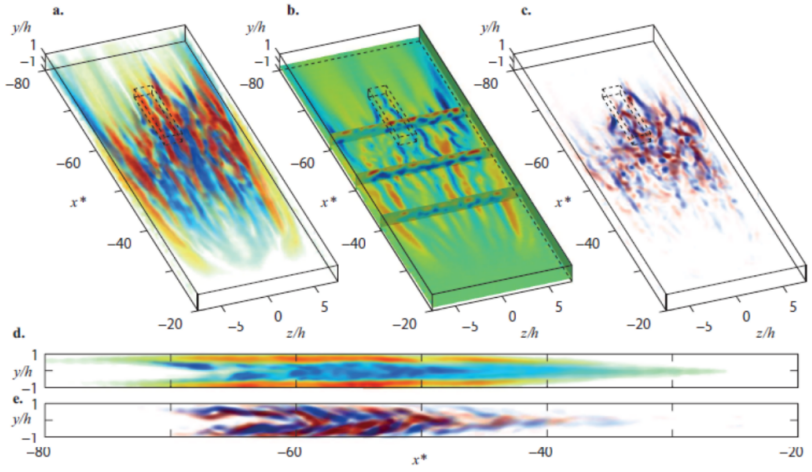

Figure 1.7: Reconstructed fields in the channel of dimensions $220h \times 2h \times 15h$ with $h = 0.001m$ showing the presence of a spot. (a) and (d) represent streamwise fluctuations. (b) and (e) represent streamwise vorticity. (c) shows streamwise fluctations in specific wall-normal and streamwise planes. Taken from [6]

In the box indicated by dotted lines in Fig. 1.7 near the trailing edge of the spot, they observe a TW-like structure as shown in Fig. 1.8.

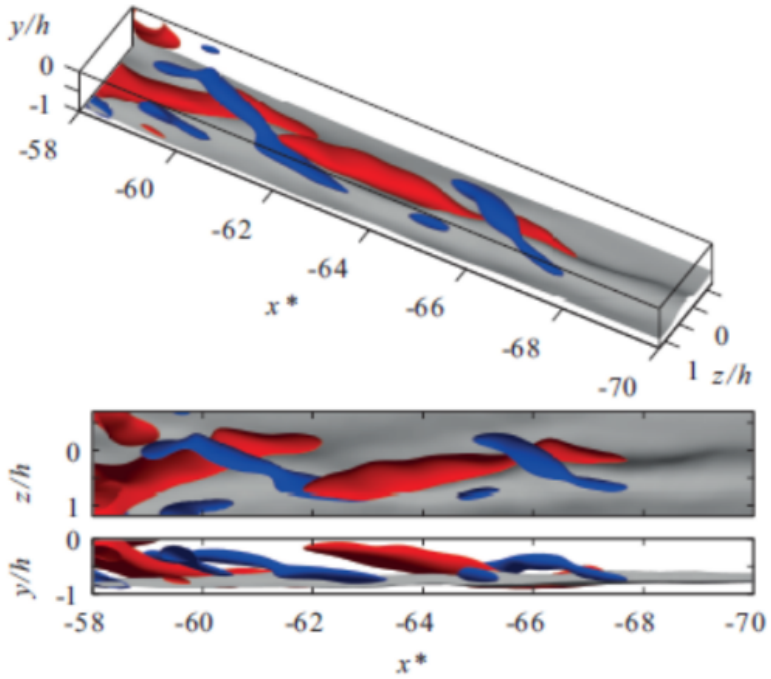

Figure 1.8: A TW-like structure close to the trailing edge of the spot. Blue and red represent different iso-surfaces of streamwise vorticity, and grey represents the iso-surface of streamwise velocity. Taken from [6]

1.4 Modal linear stability theory

The earliest approaches to understand transition to turbulence in shear flows was based on linear stability theory. A flow is said to be linearly stable if, upon addition of a disturbance of small or moderate amplitude, the flow returns to its original laminar state. If the disturbance amplifies, and changes the flow state from laminar to a different one, the flow is considered to be unstable [25]. Infinitesimally small perturbations were added to the base flow to check whether they would make the flow unstable. It was found numerically that plane Poiseuille flow was linearly stable until a critical Reynolds number of $Re_c = 5772$ [26]. Re, a non-dimensional quantity is the governing parameter of the flow and is defined in this case as $Re = \frac{Uh}{\nu}$ where U is the centreline velocity U_{cl}, and h the half-width of the channel. For $Re > Re_c$, any small disturbance leads to exponentially growing eigenmodes which manifest in the form of two-dimensional Tollmien-Schlichting (TS) waves. The TS waves undergo a secondary instability and a series of bifurcations eventually leading to turbulence. One of the strong limitations of linear stability analysis is that the disturbance is always assumed to be small, and hence linear equations govern the evolution of disturbances. As the disturbance velocities grow, nonlinear effects come into picture, and the linear stability analysis fails at describing the later evolution of the disturbances. It is seen from [27], [28], [29] and [30] that whereas the instabilities leading to TS waves give rise to spanwise vortices, the vortical structures which are actually observed in turbulent flows correspond to streamwise vortices, which cannot be explained using TS waves. It has been found that plane Poiseuille flow undergoes transition to turbulence without the involvement of TS waves at $Re = 1000$, which is much lower than Re_c. Consequently, the transition bypasses the classical scenario of TS waves and was termed as "subcritical transition" or "bypass transition".

1.5 Non-modal linear stability analysis

Schmid and Henningson, in their classical book [7] on shear flows describe nonmodal growth mechanisms as another path to turbulence which could justify energy growth even in the absence of exponentially growing eigenmodes. Instead of treating the stability analysis as an eigenvalue problem, they investigate the equations in the form of an initial value problem. The example taken is the system

$$\frac{d}{dt}\begin{pmatrix} v \\ \eta \end{pmatrix} = \begin{pmatrix} -\frac{1}{Re} & 0 \\ 1 & -\frac{2}{Re} \end{pmatrix}\begin{pmatrix} v \\ \eta \end{pmatrix} \tag{1.7}$$

with initial conditions $v(t = 0) = v_0$ and $\eta(t = 0) = \eta_0$. The general solution of this system is :

$$\begin{pmatrix} v \\ \eta \end{pmatrix} = v_0 \begin{pmatrix} 1 \\ Re \end{pmatrix} exp[-t/Re] + (\eta_0 - v_0 Re)\begin{pmatrix} 0 \\ 1 \end{pmatrix} exp[-2t/Re] \tag{1.8}$$

using the eigenvalues and eigenvectors of the evolution matrix. Looking only at the eigenvalues of this system $-\frac{1}{Re}, -\frac{2}{Re}$, it seems that v and η decay exponentially and indeed the asymptotic decay for $t \to \infty$ is expected. But looking at the η-variable separately, we have

$$\eta(t) = \eta_0 exp[-2t/Re] + Re\ v_0(exp[-t/Re] - exp[-2t/Re]). \tag{1.9}$$

The first term on the right-hand side of Eqn. 1.9 represents the evolution of the initial condition η_0 in time. The second term represents the response in η to the driving by v, and can be expanded for small times using the Taylor series as

$$\begin{aligned} Re\ v_0(exp[-t/Re] - exp[-2t/Re]) &= v_0 Re(1 - \frac{t}{Re} + \frac{t^2}{4Re^2} - ... - 1 + \frac{2t}{Re} - \frac{4t^2}{4Re^2} + ...) \\ &= v_0 t - \frac{3v_0}{4Re} t^2 + ... \end{aligned} \tag{1.10}$$

which shows that for small times $t < \mathcal{O}(Re)$ the η-component can experience "algebraic growth". This shows that the superposition of two exponentially decaying terms does not necessarily decay at all times and can generate finite algebraic growth. This is due to the non-orthogonality of the eigenvectors, whose phase difference is found to be

$$cos\Phi = \frac{Re}{\sqrt{1 + Re^2}}. \tag{1.11}$$

It is seen clearly that $\lim_{Re \to \infty} \Phi = 0$, i.e. the two eigenvectors approach each other as Re increases. This is depicted pictorially in 1.9.

Hence a combination of two eigenvalues that are exponentially decreasing (and hence, should not lead to instability ideally according to linear stability analysis) can give rise to a transient increase in the amplitude of an initial condition, even if the amplitude eventually vanishes for $t \to +\infty$

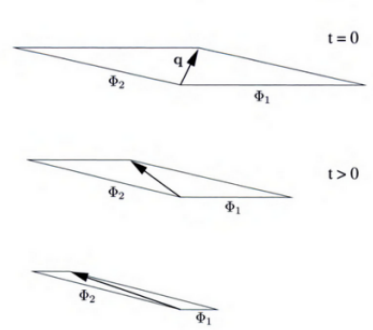

Figure 1.9: Sketch illustrating transient growth due to nonorthogonal super-position of two vectors that decay at different rates as time evolves in plane Poiseuille flow, taken from Schmid and Henningson [7]

Fig. 1.9 shows two eigenfunctions represented by the vectors Φ_1 and Φ_2 and an initial condition q which is expressed as a nonorthogonal superposition of the two eigenvectors. The diagonal of the resulting parallelogram represents the solution. While individually both the eigenvectors decrease with time, as is seen by the shortening of the length of Φ_1 and Φ_2, the initial condition does not monotonically decrease. The initial condition q undergoes a transient growth because of the phase difference between the two eigenvectors, and then eventually decays. This initial transient growth overshadows the asymptotic

behaviour predicted by the eigenmodes. Hence, in the description of the dynamics of general initial conditions, eigenvectors and the phase difference between them are as important as the eigenvalues themselves.

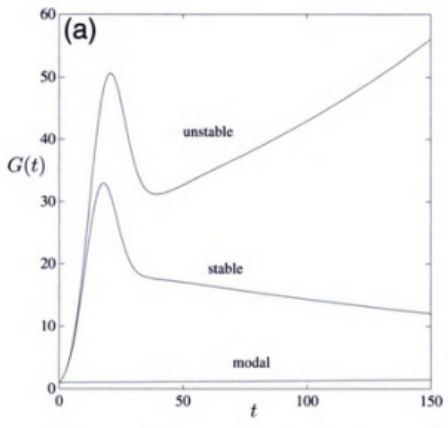

Figure 1.10: Growth functions in plane Poiseuille flow; stable case corresponds to $Re = 5000$; the unstable case to $Re = 8000$ and the modal refers to $Re = 8000$ but with the initial velocity being the normalized eigenfunction corresponding to the unstable eigenvalue, taken from Schmid and Henningson [7]

Specifically, for plane Poiseuille flow, the growth functions $G(t) = \underset{E_0 \neq 0}{max} \frac{E(t)}{E_0}$ for stable and unstable flows are shown in Fig. 1.10. $E(t)$ is the kinetic energy associated with the flow, and $E_0 = E(t = 0)$. For small times, the growth function is qualitatively the same for both stable (corresponds to $Re = 5000$) and unstable (corresponds to $Re = 8000$) flows even in the transient phase. The transient growth is much smaller for the stable case whereas the higher transient growth in the unstable case results in the flow eventually becoming unstable. The curve that is marked "modal" refers to the case where the initial perturbation velocity is the normalised eigenfunction associated with the unstable eigenvalue for $Re = 8000$. From this plot, it is seen clearly that it is not necessarily the unstable mode that achieves the highest energy growth but another initial condition which happens to be a linear combination of several eigenfunctions.
To conclude, perturbations grow through either the modal or the non-modal linear mechanism, but their nonlinear evolution is still unknown, and hence this by no means predicts whether there will be turbulence or not. Regardless of the linear stability (or not) of the base flow, finite-amplitude disturbances can be transiently amplified up to a level where nonlinearity effects cease to be negligible. Obviously a fully nonlinear theory is required at this stage to describe the later evolution of such a disturbance.

1.6 Self-sustaining process

All these linear approaches attempted to explain turbulence by defining a base flow (the laminar state), and observing the evolution of disturbances to this base flow in its immediate neighbourhood. How big the deviation of the base flow needed to be in order to escape the laminar basin and become turbulent was the question which was generally investigated. But aren't there other so-called "attractors" in the huge phase space of fluid

states which are not in the immediate neighbourhood of the laminar flow, and if so, how are they to be explained? In his seminal paper in 1997 [8], Fabian Waleffe suggested a theory wherein he explains that a "self-sustaining process where streamwise rolls redistribute the mean shear to create streaks that break down to recreate the rolls", is responsible for turbulence in canonical shear flows.

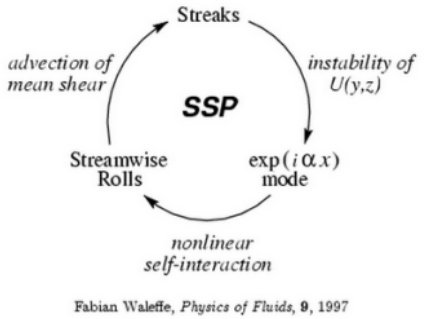

Figure 1.11: A schematic of the self-sustaining process, taken from [8]

The self-sustaining process consists of three distinct phases. The first phase corresponds to the "formation of streaky flow". Streamwise vortices/rolls $[0, v(y,z), w(y,z)]$ decouple from the streamwise velocity $[u(y,z), 0, 0]$ and undergo a slow viscous decay. However the streamwise rolls redistribute the streamwise velocity in the yz planes. The resulting spanwise fluctuations, $u(y,z) - \bar{u}(y)$ (where $\bar{u}(y)$ represents the base flow of the system) are called "streaks". These streaks then undergo a wave-like instability in which three-dimensional disturbance of the form $e^{i\alpha x}v(y,z)$ develops. Finally this gives rise to nonlinearities which feeds energy back into the original streamwise rolls, thereby making the process self sustained.
In summary

- Streamwise rolls induce streaks by redistribution of mean momentum in the yz plane.
- Streaks undergo an inflectional-type instability that gives rise to streamwise undulation.
- Nonlinear effects arising from the instability re-energize the streamwise rolls.

The S.S.P. theory justifies the existence of exact solutions such as steady states and periodic orbits disconnected from the base flow. The next step in this development is a nonlinear theory organised around such solutions.

1.7 Dynamical systems theory

1.7.1 Classical approach

In the recent years, there has been a lot of focus on understanding transition to turbulence, especially in shear flows through the lens of dynamics systems theory [14] [31] [32] . The fluid flow governed by the Navier-Stokes equations which are partial differential equations (P.D.E.s) is understood as a dynamical system,

$$\frac{d\boldsymbol{X}}{dt} = \boldsymbol{F}(\boldsymbol{X}), \boldsymbol{X} \in \mathbb{R}^N \tag{1.12}$$

$$\boldsymbol{X}(t=0) = \boldsymbol{X}_0 \ (\textit{Initial condition}) \tag{1.13}$$

where $\boldsymbol{X}$ is the state of the system, in our case the velocity field $\boldsymbol{u}$. The state space of the system comprises all the velocity fields $\boldsymbol{u}$. The dynamical system represented in Eqn. 1.12 is strictly equivalent to the partial differential equation (P.D.E.) system represented in equations 3.1 and 3.2, i.e. the dynamical system is not any reduced order approximation of the P.D.E. system and one can go back and forth from one description to the other. Formally, the dimension of this state space N is infinite, but the presence of viscous dissipation makes an infinite-dimensional system redundant, and introduces a limit to the dimensionality of the system. Discretisation for numerical computation reduces the dimensions of the state space $\approx \mathcal{O}(10^6)$ in our case.
Hopf [33] formulated the idea that Navier-Stokes turbulence can be expressed in terms of unstable invariant solutions. In this framework, the turbulent region of state space consists of numerous solutions connected by a web of homoclinic (connection of a solution to itself) and heteroclinic (connection between two different solutions) connections. For instance, a chaotic trajectory transiently approaches an unstable solution and stays in its neighbourhood for a while before being repelled along its unstable manifold and towards another solution as shown in Fig. 1.12 [9]. The trajectory can eventually leave this tangle of solutions and approach the (stable) laminar fixed point. In such a case, the flow has relaminarised and the turbulence lifetime is finite [10] [34] [35].

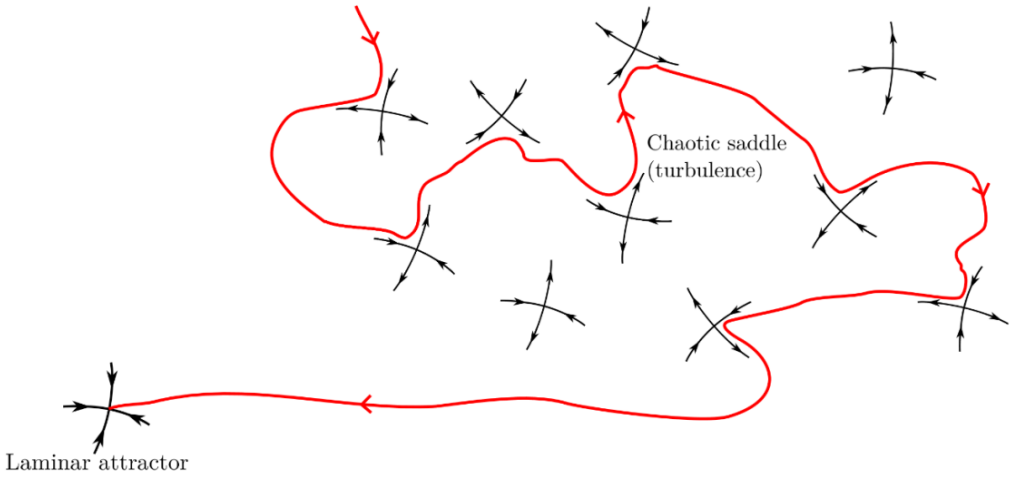

Figure 1.12: A schematic taken from [9] showing a transient turbulent trajectory in state space. The trajectory approaches unstable solutions along their stable manifolds, stays in the neighbourhood for a while and gets repelled along their unstable manifolds.

The classical deterministic approach nowadays is to find the invariant sets which are solutions of the system shown in Eqn. 1.12. These invariant sets could be fixed points (also referred to as equilibria) to which regions of initial conditions in their neighbourhood asymptote to as time increases. If a dynamical system is defined as (M, ϕ) where M represents the state space of all the possible states of the system, and the function ϕ

represents the flow or dynamics, the state at an arbitrary time t is determined by the initial state at time t_0 and the governing function ϕ as

$$x(t) = \phi^t(x_0) \tag{1.14}$$

and fixed points are defined as all points $x \in M$ in the system which satisfy

$$\phi^t(x) = x, \ for\ all\ t. \tag{1.15}$$

Other important invariant sets are the periodic orbits i.e. all points $x \in M$ such that,

$$\phi^t(x) = \phi^{t+T_p}(x), \ for\ a\ given\ minimum\ period\ T_p\ and\ for\ all\ t \tag{1.16}$$

A periodic orbit p is the set of points $M_p \subset M$ swept out by a trajectory that returns to the initial point in a finite time. It is considered that periodic orbits form the skeleton of any chaotic attractor or saddle, and that every point on the attractor or saddle is approached arbitrarily close by a periodic orbit [36]. Kawahara and Kida [37] identified in plane Couette flow an exact periodic orbit, which in physical space corresponds to the cyclic regeneration of streaks involving a bursting event and vorticity redistribution. Most of these unstable solutions emerge from saddle-node bifurcations.
Nagata [38] computed the first 3D exact solutions of plane Couette flow which happened to be steady states, by tracking a 3D exact solution from Taylor-Couette flow to plane Couette flow. The two solutions found by Nagata are equilibria that are created in a saddle-node bifurcation, and lie on the lower branch and the upper branch of the bifurcation diagram as shown in Fig. 1.13.

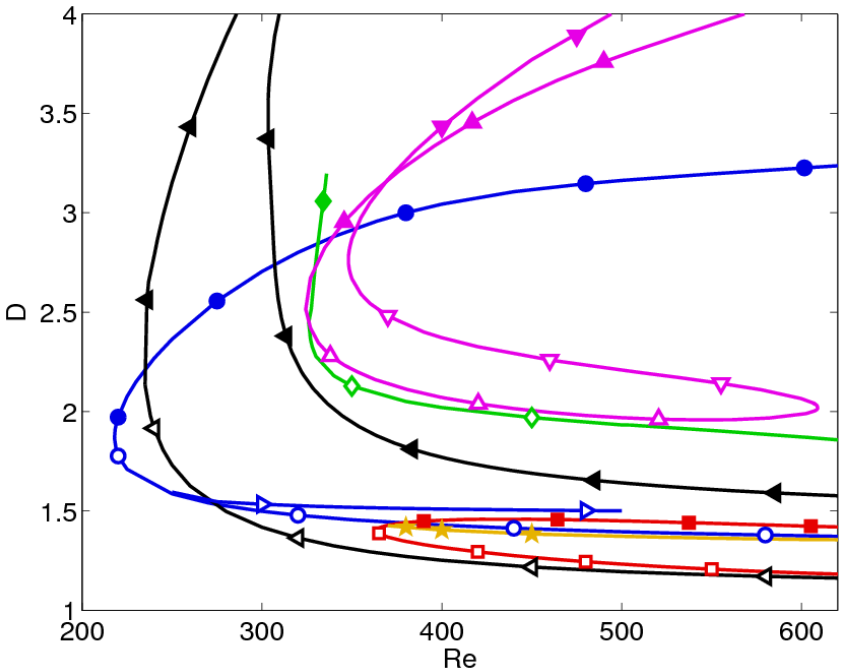

Figure 1.13: Saddle-node bifurcation diagram in blue depicting the Nagata lower branch and upper branch solutions, the blue dots are upper branch equilibria and the blue circles are lower branch equilibria; taken from [10]

Fig. 1.13 shows the dissipation D as a function of Re for the solutions of plane Couette flow computed by Nagata among others. The solutions marked by blue dots represent the Nagata upper branch equlibria the blue circles represent the Nagata lower branch equilbria in plane Couette flow. A visualisation of these solutions in plane Couette flow by Gibson *et al.* taken from Chaosbook [10] is shown in Fig. 1.14.

((a) The lower branch equilibrium) ((b) The upper branch equilibrium)

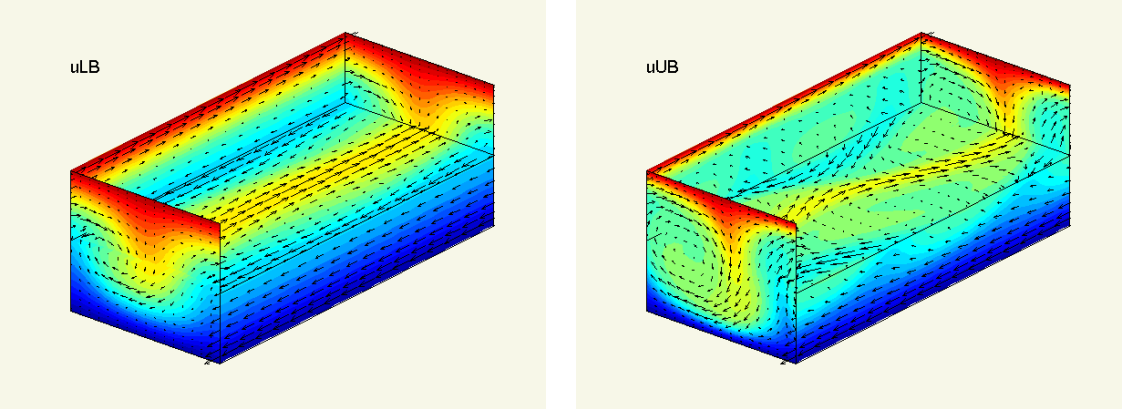

Figure 1.14: Visualisation of the Nagata solutions in plane Couette flow by Gibson *et al.* taken from [10], colours represent u, vectors represent v and w

Fig. 1.14(a) corresponds to the blue circles in Fig. 1.13 and Fig. 1.14(b) corresponds to the blue dots in Fig. 1.13.

1.7.2 Presence of continuous symmetries

Symmetries play an important role in studying the transition to turbulence in parallel shear flows, especially in periodic domains [10]. Parallel shear flows like plane Poiseuille flow have continuous symmetries associated with possible translations along the streamwise and spanwise directions. This gives rise to flow states that differ just by a translation or a shift along the streamwise or spanwise directions but are dynamically equivalent. We generally write that two fields u and v are related by a shift σ when $\sigma u = v$. For instance, if $\forall x$, $u(x-y) = v(x)$, then u and v are related by σ, which is here a translation by $-y$. The generalisation of steady states (equlibria) in the presence of continuous symmetries are travelling waves (relative equilibria) defined by

$$\phi^t(x) = \sigma_{(t)} x \ for \ all \ t \tag{1.17}$$

with $\sigma_{(t)}$ representing a shift by $\vec{c}t$, where $\vec{c}$ is the velocity of the wave. Similarly, periodic orbits get generalised into relative periodic orbits defined as all x such that

$$x = \sigma \Phi^{T_p}(x) \tag{1.18}$$

where σ again represents a shift in the spatial direction/s.
The presence of continuous symmetries makes it difficult to find steady states and periodic orbits. Steady states are generalised as travelling waves, and periodic orbits as relative periodic orbits. In systems with continuous symmetries, it becomes necessary to visualise

the dynamics in the absence of continuous symmetries in order to identify steady states and periodic orbit solutions of the quotiented system, but also in order to shed light on the actual dynamics.

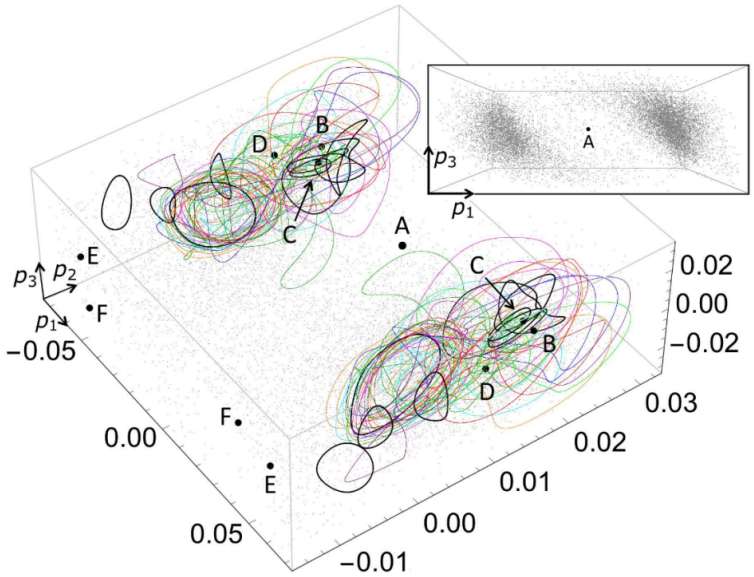

Figure 1.15: Phase portrait of relative equilibria in pipe flow, taken from [11]

Fig. 1.15 shows the relative periodic orbits and travelling waves found in pipe flow, taken from [11]. All solutions here are 'relative equilibria' and not equilibrium solutions. This is because of the inherent continuous symmetries in the form of translations along the axial and azimuthal directions, and reflections in the azimuthal direction.
Duguet *et al.* [31] found relative periodic orbits bifurcating from travelling waves in pipe flow. Fig. 1.16 shows the different saddle-node bifurcations of mirror-symmetric travelling waves found in pipe flow by [12].

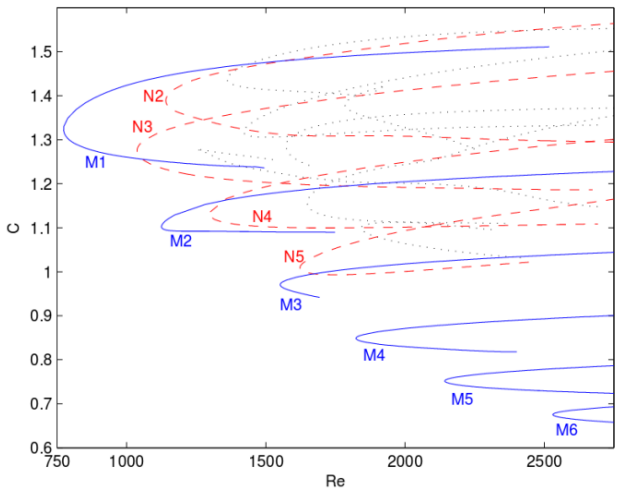

Figure 1.16: Plot of phase speed C against Re showing the different saddle-node bifurcations in mirror-symmetric travelling waves found in pipe, taken from [12]

In Fig. 1.16, the curves in blue and red represent different classes of shift-reflect symmetric travelling waves found by [12]. With increasing Re, there are more and more families of exact solutions (in this case, the travelling waves) populating the state space, which indicates that turbulence at higher Re tends to be more complex.
The search for exact coherent states in plane Poiseuille flow in fact started a long time ago, and the first three-dimensional solutions in plane Poiseuille flow were described in [39] in 1991. Ehrenstein and Koch found three-dimensional travelling waves below the saddle-node point of the two-dimensional Tollmien-Schlichting waves from which they bifurcate and studied their dependence on the streamwise and spanwise length. There were also other subsequent studies identifying many other three-dimensional exact coherent states in plane Poiseuille flow [40, 41, 42, 43, 44, 45, 46]. In particular, the dependence of particular solutions on the streamwise and spanwise wavelengths is studied in [41] and [42].

1.7.3 Special invariant sets - Edge states

In subcritical transition, we know that there is coexistence of two flow regimes in state space : the laminar state and the chaotic attractor (we disregard the possibility for finite lifetimes here) called turbulence. Is there a boundary that separates the initial conditions that evolve towards either of these attractors? One of the focuses in recent years has been on identifying the boundary regime that separates the laminar and the turbulent regimes. Skufca *et al.* [47] found in their study of a 9D model that a boundary indeed exists in state space between the laminar and the turbulent flow regimes as a hypersurface. They termed this boundary the 'edge of chaos'. It forms the stable manifold of an attractor on the boundary, which they termed 'edge state'. The edge state is an invariant set with an unstable direction of dimension 1 transversal to the edge, and all stable directions lying within the edge of chaos. Edge states are helpful in giving a clear picture of the structure of the phase space, and also in understanding the physical processes responsible for the sustenance of non-trivial dynamics in the system. The first numerical investigations of edge states were performed in the context of minimal flow units (M.F.U.) [1] [48]. The classical method to find the edge state is the bisection approach, first used in channel flow by Toh and Itano [49]. Fig. 1.17 [13] shows a schematic of how the bisection process restricts a trajectory to the edge.

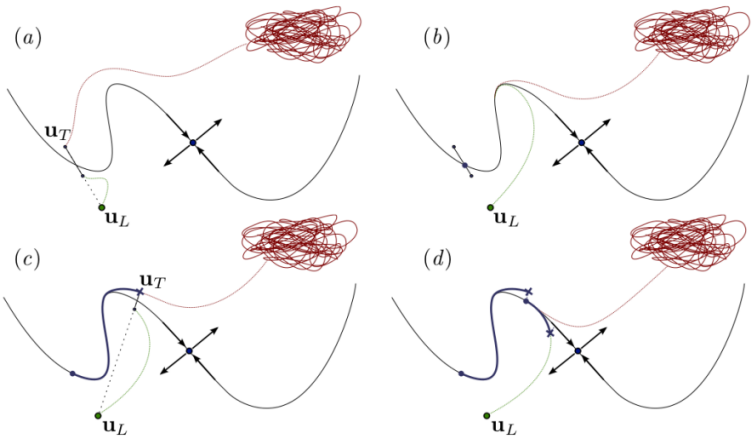

Figure 1.17: A schematic to illustrate the edge-tracking algorithm using the bisection process, taken from [13]. The black solid line represents the edge separating the laminar attractor in green, and the turbulent attractor in red.

Fig. 1.17 considers two arbitrary initial condtions $\boldsymbol{u_T}$ and $\boldsymbol{u_L}$ straddling the edge (which is represented by the solid black line). With evolution in time, all trajectories starting from $\boldsymbol{u_L}$ laminarise and those starting from $\boldsymbol{u_T}$ become turbulent. Knowing that the edge lies between these two sets of initial conditions, a bisection is performed along the line connecting the two initial conditions : we consider the family of initial condtions $\boldsymbol{u} = \boldsymbol{u_L} + \lambda(\boldsymbol{u_T} - \boldsymbol{u_L})$, where λ is the bisection parameter ranging between 0 and 1, and DNS is initialised. A relevant scalar observable is chosen and thresholds are set to designate if the trajectory deviates from the edge towards either the laminar or the turbulent regimes. Depending on which side the trajectory eventually ends up, a new initial condition is chosen by rescaling λ, and the process is repeated. At the end of bisection, we obtain an initial condition on the line between $\boldsymbol{u_L}$ and $\boldsymbol{u_T}$ which lies closest to the edge. However, the trajectory starting from this initial condition is not exactly on the edge and eventually deviates because of the limited numerical accuracy in fixing the initial condition on the edge, and the natural instability of the edge. To continue on the edge, the whole process of bisection is repeated by choosing new appropriate values for $\boldsymbol{u_L}$ and $\boldsymbol{u_T}$. The piecewise continuous trajectory obtained shadows the edge, and eventually approaches the attractor on the edge, i.e. the edge state.
Trajectories that are restricted to the edge via this algorithm eventually converge to the edge state, which can be a fixed point like in spatially periodic plane Couette flow [50], a travelling wave like in spanwise extended plane Couette flow [51], [52], a travelling wave in cylindrical pipe flow [53] [54], a relative periodic orbit like in channel flow [55] or more generically a chaotic object in full pipe flow [56]. Edge states were also found in boundary layer flows in [57, 58, 59, 60]. All these edge states in shear flows typically consist of streamwise streaks and vortices, and seem to follow the self-sustaining process proposed by Waleffe [8].

1.7.4 Global state space description

The Navier-Stokes equations have been represented as a deterministic nonlinear system of the generic form $d\boldsymbol{X}/dt = \boldsymbol{F}(\boldsymbol{X})$. The confinement by the periodic boundary conditions indeed makes the original system spatially correlated, which justifies such an approach

rather than a fully spatiotemporal approach. In this paradigmatic view, tools borrowed from dynamical systems theory have proven useful to describe accurately the structure of the associated phase space [61]. This state space is formerly of infinite dimension, though in practice dissipation coupled with numerical truncation makes it a finite, yet very high-dimensional state space [62]. This accurate description, more descriptive than truly quantitative, relies on numerical identification of the invariant sets, among them fixed points, periodic orbits and their connecting manifolds [63]. Invariant sets such as travelling waves, periodic orbits and relative periodic orbits form the backbone of turbulent dynamics in wall-bounded shear flows. Populating the phase space with exact coherent states gives us interesting insights into the underlying dynamics through the connections between different solutions.

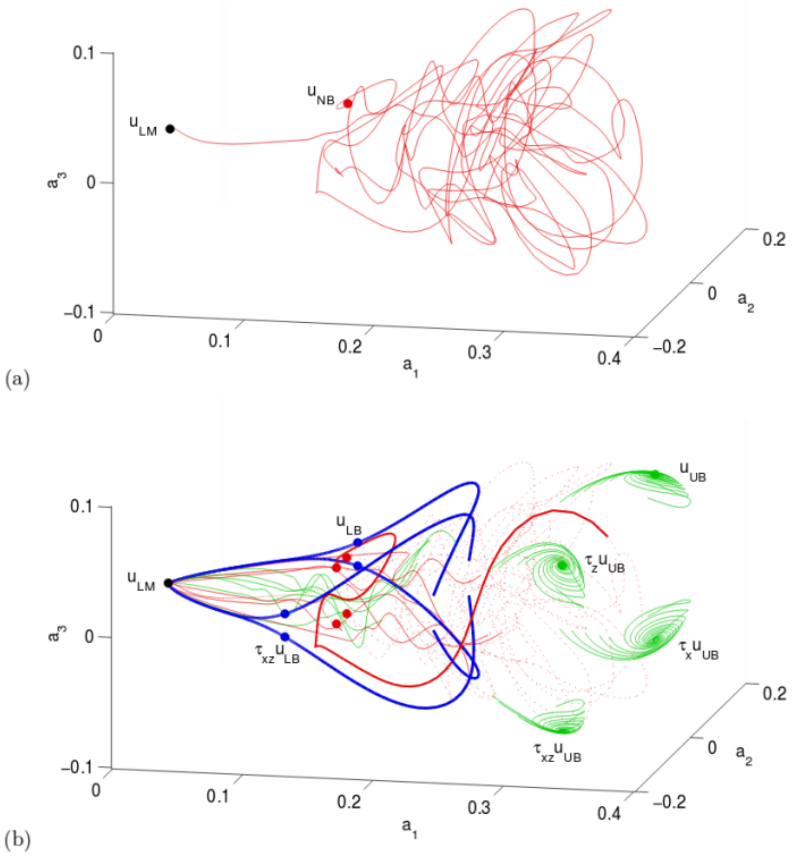

Figure 1.18: Phase portrait of a transient turbulent trajectory with respect to (w.r.t.) the exact coherent states found in plane Couette flow, taken from [14]

Fig. 1.18 shows a state space representation of the different exact solutions found by [14] in plane Couette flow. The details of the construction of the projection basis consisting of the basis vectors a_1, a_2, a_3 and a_4 shown in Fig. 1.18 have been explained in sec.5.3.1. It is interesting to note that Gibson *et al.* found a new exact solution represented by u_{NB} in Fig. 1.18(a) by observing the different unstable manifolds and heteroclinic connections between the different exact solutions u_{LB} and u_{UB} earlier obtained by them.
The goal of the present work is to investigate the state space visualisation of plane Poiseuille flow with an aim of understanding better, the underlying dynamics in the transition of flows to turbulence in this flow. It is also our aim to develop tools to visu-

alise the dynamics in physical space in the absence of continuous symmetries. Chapter 2 introduces earlier studies of turbulence at high Reynolds numbers in channels of different domain sizes. Chapter 3 introduces the numerical tools and techniques, used and developed in this study. The results of turbulent computations in the present study, including their properties, visualisations and statistical analyses are introduced in Chapter 4. Chapter 5 introduces the exact coherent states identified in the course of this study, details the mechanisms by which they were identified and/or computed and proposes a state space representation to represent the different flow regimes computed in the course of this study. Chapter 6 contains statistical analysis of turbulent computations in one of our domains, and a discussion about the kind of scaling observed in the different flow regimes computed in this study. Finally, Chapter 7 contains the summary of the present work along with conclusions and perspectives for further work in this regard.

Chapter 2

Turbulence in channel flow

2.1 Inner units definition

The streamwise velocity profile of plane Poiseuille flow close to the walls is almost linear at first order and can be considered similar to that seen in plane Couette flow. A schematic of the zoomed profile near the walls is shown in Fig. 2.1.

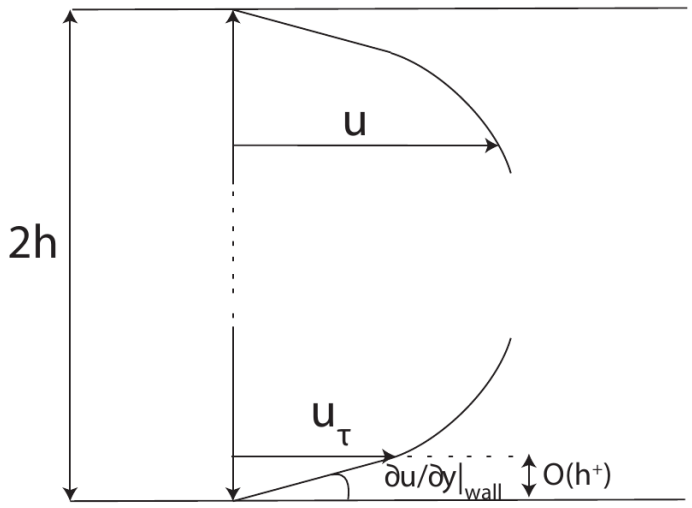

Figure 2.1: Schematic showing the linearised profile of plane Poiseuille flow close to the wall

The only information directly known at the wall is the shear stress $\mu \frac{du}{dy}|_{wall}$ and the kinematic viscosity ν of the fluid. With this information, the only length scale that can be defined is

$$h^+ = \frac{\nu}{u_\tau} \tag{2.1}$$

where the friction velocity u_τ is defined as $u_\tau = \sqrt{\nu \frac{\partial u}{\partial y}|_{wall}}$
We then define a Reynolds number based on this friction velocity, the friction Reynolds number Re_τ as follows

$$Re_\tau = \frac{u_\tau h}{\nu} = \frac{h}{h^+}. \tag{2.2}$$

Re_τ measures in effect the ratio of the largest scales ($\mathcal{O}(h)$) to the smallest scales ($\sim \mathcal{O}(h^+)$) and is thus an indicator of the scale separation in the flow. A high value of Re_τ indicates that $h >> h^+$, meaning there is a very large scale separation in the wall-normal direction and the flow is turbulent with a wide hierarchy of scales.
Conversely, at lower Re_τ we see that the large scales and the small scales are almost the same.
In the scenario where the driving mechanism is the constant pressure gradient dp/dx ($dp/dx < 0$ yields a flow in the positive streamwise direction), the following relation between the Re_τ, and the dp/dx holds :

$$Re_\tau = \frac{h}{\nu}\sqrt{\frac{-dp}{dx}} \tag{2.3}$$

Correspondingly, the channel dimensions originally L_x and L_z (defined in units of the channel half-width h), can be expressed in inner units in terms of Re_τ as

$$L_x^+ = L_x \times Re_\tau \tag{2.4}$$

$$L_z^+ = L_z \times Re_\tau \tag{2.5}$$

2.2 Fully developed turbulence in channel flow

We now address the properties of fully-developed turbulence in channel flow at very high Re_τ.

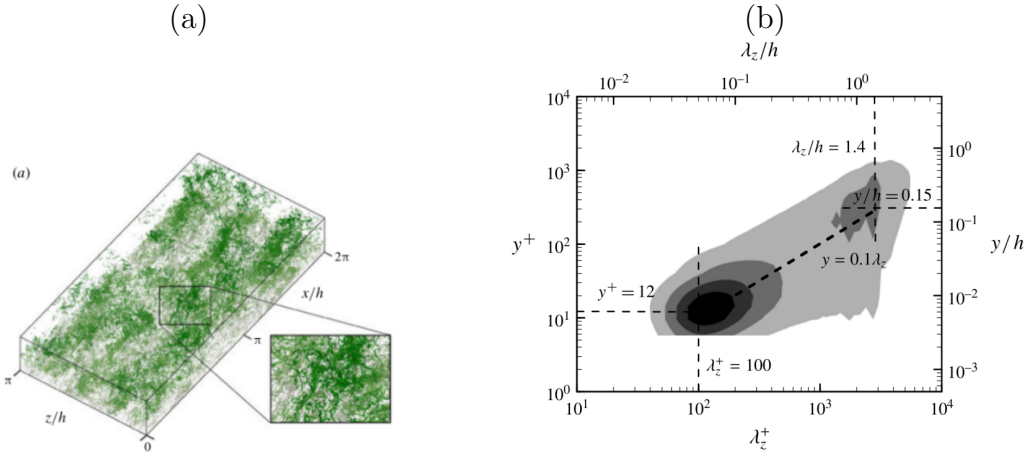

Figure 2.2: (a)Coherent structures in a turbulent snapshot from the simulations of Lozano-Duran and Jimenéz [15] in a channel of dimensions $2\pi h \times 2h \times \pi h$ for $Re_\tau = 4164$ with vortex clusters, and (b) (premultiplied) spanwise spectrum of u in a turbulent channel for $Re_\tau = 2003$ taken from [16]

Lozano-Duran and Jiménez [15] visualise coherent structures in turbulent channels where vortex clusters are identified based on the definition that the discriminant of the velocity gradient tensor is greater than zero [64]. Fig. 2.2(a) is the visualisation of large vortical structures in a channel of dimensions $2\pi h \times 2h \times \pi h$ at a high Reynolds number $Re_\tau = 4164$. From Eqns. 2.4 and 2.5 the channel dimensions in inner units are $L_x^+ \times L_z^+ \approx 26160 \times 13080$. In comparison, near-wall structures of the order of 100 inner units (as seen from the spectra in Fig. 2.2(b)), are too small to be observed in this visualisation. Fig. 2.2(b) shows the premultiplied spectrum of u in a turbulent channel at a high Reynolds number, $Re_\tau = 2003$, albeit different from the Re_τ at which computations are made for Fig. 2.2(a). A primary energy peak is visible in the maps, centred at $y^+ \approx 12$, associated with spanwise wavelengths of the order of $\mathcal{O}(100h^+)$. This corresponds to near-wall structures. A secondary peak is also visible at $y^+ \approx 180$ which corresponds to the large-scale organisation of the velocity field in the logarithmic part of the boundary layer.

2.3 Wall-attached eddy hypothesis

Townsend *et al.* [65] proposed the "wall-attached eddy hypothesis" to explain the structures populating turbulent flow in wall-bounded shear flows. Fig. 2.3 (from [16]) shows the schematic of the wall-attached eddy model which consists of eddies/vortices of different sizes, all attached to the wall. In this hypothesis, consistently with the spectrum shown in Fig. 2.2(b), the size of each structure is proportional to its distance from the wall.

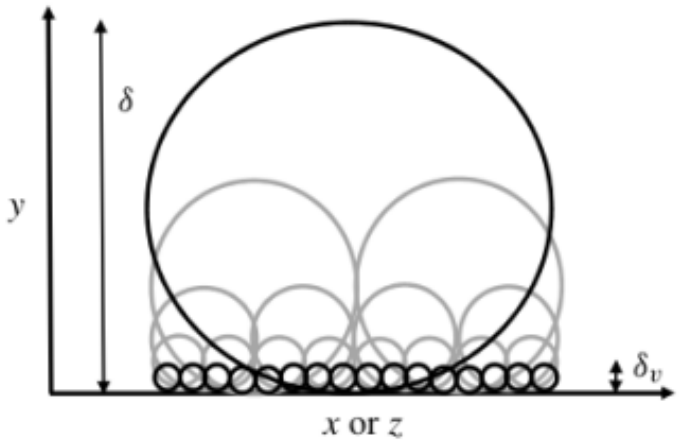

Figure 2.3: Schematic of the wall-attached eddy hypothesis proposed by Townsend *et al.*, taken from the work of Hwang [16]

This describes the existence of different scales: large eddies in the outer layer, the intermediate logarithmic region, and the near-wall inner region where the smallest scale structures are found. Initially, [66] [67] the energy containing motions (large scale motions) in the outer region were considered to be a consequence of the merging and growth of the near-wall vortices similar to a bottom-up process. Further studies in recent years [68] [69] have shown that there is no significant change in the dynamics and statistics of the outer region when the near-wall region was disturbed by wall roughness. Hwang and

Cossu [70] showed that the energy-containing motions at outer scales consisting of large and very large scale motions are self-sustained when the motions in the near-wall and logarithmic regions are artificially removed. Similarly Hwang and Cossu [71] also show that the energy-containing motions in the logarithmic region are also independent of the motion at other scales, and are capable of sustaining on their own.
It is known that the near-wall structures are sufficient to change the drag from laminar to turbulent, at least at finite values of Re_τ. Since the drag is defined basically by the gradients at the wall, it is sufficient to study the small scale wall-localised structures to estimate the drag, and the large scale structures can be neglected. But are the small scale structures capable of existing and sustaining themselves autonomously i.e. independently of the other scales, or is there a necessity for energy feedback between the different scales for the persistence of these structures? What are the length scales and velocity scales to be used to analyse these near-wall structures?

2.4 Turbulent computations in channel flow; Minimal Flow Unit (M.F.U.) computations by Jimenéz and Moin [1]

Pioneering work in isolating the near-wall structures was done by Jimenéz and Moin in 1991 [1] in a spatially periodic domain large enough to contain just the basic structures necessary to sustain turbulence. This domain has been referred to as the minimal flow unit (M.F.U.).
They performed DNS of unsteady channel flow in domains chosen such that the flow consists of a doubly periodic (in x and z) array of identical structures. They used a fully spectral N-S integrator, using Fourier expansions in the x and z directions, and Chebyshev polynomials in the y direction. The top and the bottom boundaries are physical walls with no-slip, while a periodic boundary condition is imposed in the streamwise and spanwise directions. A constant instantaneous volume flux is imposed to drive the flow. They find that a spectral expansion on $32 \times 129 \times 16$ is good enough to represent the dynamics in the channel after performing studies at different resolutions. The spanwise period of the channel was varied between 80 and 160 inner units, and the streamwise period between 300 and 600 inner units.
It is interesting to note that turbulence on both walls was observed for all Re. In addition to it, turbulence localised only on one of the walls was also observed for a few Re.

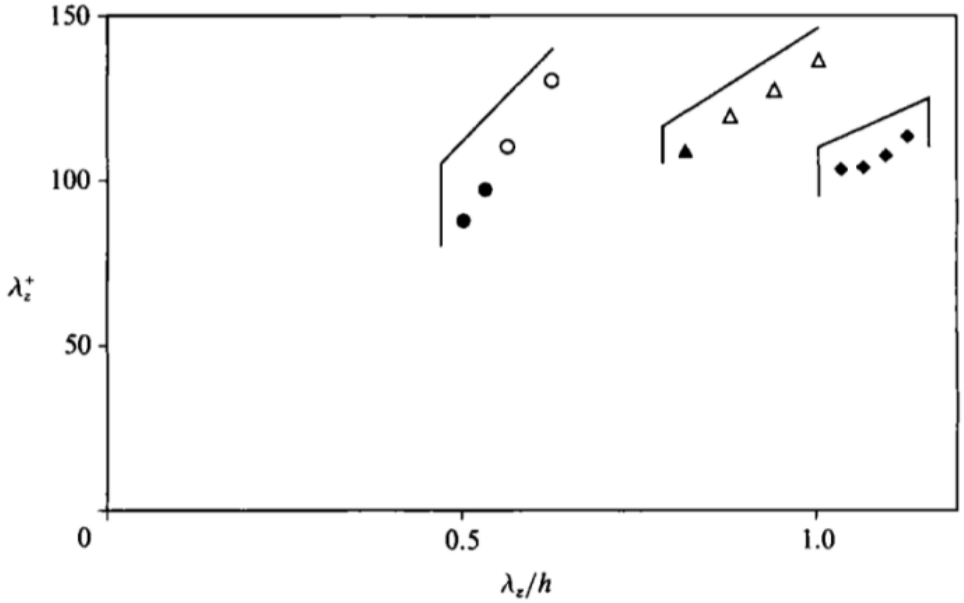

Figure 2.4: Plot from Jimenéz and Moin [1] showing the presence of turbulence at different Re and the corresponding spanwise wavelength of the channel in inner and outer units. $\circ$, $\triangle$ and $\diamond$ correspond to $Re = 2000$, $Re = 3000$ and $Re = 5000$ respectively. Open symbols represent two-walled turbulence and closed symbols represent one-walled turbulence.

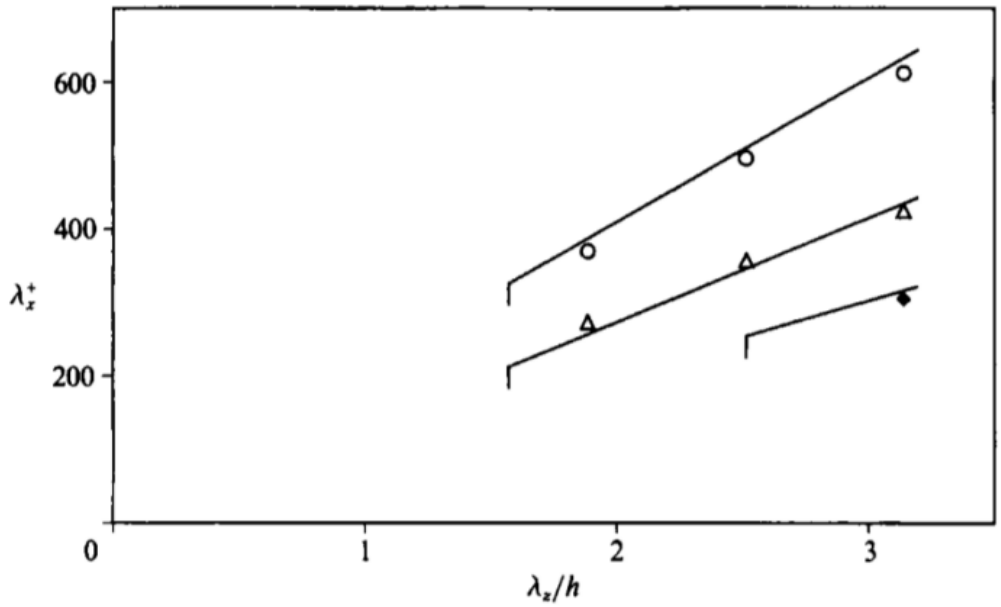

Figure 2.5: Plot from Jimenéz and Moin [1] showing the presence of turbulence at different Re and the corresponding streamwise wavelength of the channel in inner and outer units. $\circ$, $\triangle$ and $\diamond$ correspond to $Re = 2000$, $Re = 3000$ and $Re = 5000$ respectively. Open symbols represent two-walled turbulence and closed symbols represent one-walled turbulence.

Fig. 2.4 shows the spanwise wavelength in both inner units and outer units. The symbols $\circ$, $\triangle$ and $\diamond$ correspond to $Re = 2000$, $Re = 3000$ and $Re = 5000$ respectively. Open symbols

represent two-walled turbulence and closed symbols represent one-walled turbulence. It can be seen from Fig. 2.4 that the critical channel span varies for different Re when expressed in outer units but is roughly the same in inner units. They find that the critical value is around $\lambda_z^+ = 100$, in good agreement with the experimental mean streak spacing reported by Smith and Metzler [72].
They observe that their turbulent state shifts from one wall to another in a few cases. They describe that the 'quiet' wall i.e. the wall without activity undergoes transition, and for a short while, both walls become turbulent. However since this state was not stable, turbulence at one of the walls decays after a short time. They mention that this 'switching' of the active walls was a relatively rare event, and between such events, the flow remained essentially one-sided.
Jimenéz and Moin report that in the streamwise direction, although there is no clear critical wavelength as in the spanwise direction, there appears to be a minimal streamwise period of about $\lambda_x^+ \approx 250 - 350$ which becomes shorter as with increase in Re, as shown in Fig. 2.5. Note that a similar approach was developed by Hamilton, Kim and Waleffe for the context of plane Couette flow [48], with similar quantitative conclusions.
In effect, M.F.U. acts a cheap computational trick to isolate near-wall structures and observe autonomous dynamics near the wall. The framework of the M.F.U. will be used throughout the whole thesis for the state space analysis already introduced in 1.7.4.

Chapter 3

Numerical tools

3.1 Channelflow

The DNS (Direct Numerical Simulations) code *Channelflow* is an open-source software in C++ developed by John F. Gibson [73]. It is used for all numerical simulations of the incompressible Navier-Stokes flow 3.1, 3.2 in this thesis.

$$\frac{\partial \boldsymbol{u}}{\partial t} + (\boldsymbol{u} \cdot \nabla)\boldsymbol{u} = -\frac{1}{\rho}\nabla p + \nu \nabla^2 \boldsymbol{u} \tag{3.1}$$

$$\nabla \cdot \boldsymbol{u} = 0. \tag{3.2}$$

Channelflow is written specifically for Cartesian geometries with two periodic directions and one inhomogeneous direction. Since the flow on which this thesis focuses is plane Poiseuille flow, which is flow within two parallel walls, *Channelflow* is an ideal tool for the computations and analysis in this context. The fluid flow is in the rectangular domain $\Omega \triangleq L_x\mathbb{T} \times [-1, 1] \times L_z\mathbb{T}$ where $\mathbb{T}$ is the periodic unit interval. No-slip boundary conditions are imposed at the walls, i.e. $\boldsymbol{u} = 0$ at $y = -1$ and $y = +1$. Periodic boundary conditions are imposed in the streamwise and spanwise directions, i.e. $\boldsymbol{u}(x + L_x, y, z, t) = \boldsymbol{u}(x, y, z, t)$ and $\boldsymbol{u}(x, y, z + L_z, t) = \boldsymbol{u}(x, y, z, t)$. The spatial direction is spectrally discretised, with the streamwise and spanwise directions being expanded into Fourier modes, and the wall-normal direction being expanded into Chebyshev modes, and finite differencing is used in time.
Channelflow defines the discrete xz-Fourier transform and inverse as

$$\tilde{f}_{k_x,k_z} = \frac{1}{L_x L_z} \sum_{n_x=0}^{N_x-1} \sum_{n_z=0}^{N_z-1} f(x_{n_x}, z_{n_z}) e^{-2\pi i (k_x x_{n_x}/L_x + k_z z_{n_z}/L_z)} \triangle x \triangle z, \tag{3.3}$$

$$f(x_{n_x}, z_{n_z}) = \sum_{k_x=-\frac{N_x}{2}+1}^{\frac{N_x}{2}} \sum_{k_z=-\frac{N_z}{2}+1}^{\frac{N_z}{2}} \tilde{u}_{k_x,k_z} e^{2\pi i (\frac{k_x x_{n_x}}{L_x} + \frac{k_z z_{n_z}}{L_z})} \tag{3.4}$$

for $f(x, z)$ on the domain $x \in L_x\mathbb{T}$ and $z \in L_z\mathbb{T}$. The gridpoints and stepsizes are defined by $x_{n_x} = n_x \triangle_x$, $z_{n_z} = n_z \triangle_z$, $\triangle_x = L_x/N_x$ and $\triangle_z = L_z/N_z$ whereas the continuous Fourier transform and its inverse are given by

$$\overline{f}_{k_x,k_z} = \frac{1}{L_x L_z} \int_0^{L_x} \int_0^{L_z} f(x,z) e^{-2\pi i(k_x x/L_x + k_z z/L_z)} dx dz, \tag{3.5}$$

$$f(x,z) = \sum_{-\infty}^{\infty} \sum_{-\infty}^{\infty} \overline{f}_{k_x,k_z} e^{2\pi i(k_x x/L_x + k_z z/L_z)} \tag{3.6}$$

The discrete Fourier transform and inverse can be viewed as a finite-sum approximation to the continuous transform and inverse. For sufficiently smooth f, the discrete spectral coefficients can be used to form an uniformly convergent approximation of f as

$$f(x,z) = \sum_{k_x=-\frac{N_x}{2}+1}^{\frac{N_x}{2}} \sum_{k_z=-\frac{N_z}{2}+1}^{\frac{N_z}{2}} \tilde{u}_{k_x,k_z} e^{2\pi i(\frac{k_x x}{L_x} + \frac{k_z z}{L_z})} \tag{3.7}$$

The Chebyshev expansions of a function g on the domain $[-1,1]$ is given by

$$g(y) = \sum_{n=0}^{N-1} \hat{g_n} \overline{T}_n(y) \tag{3.8}$$

where $\overline{T}_n$ is the n-th Chebyshev polynomial rescaled for the domain $y \in [-1,1]$, i.e.

$$\overline{T}_n(y) = T_n y \tag{3.9}$$

The discrete set of Chebyshev gridpoints are given by

$$y_n = cos(\frac{n\pi}{N_y - 1}), n \in [0, N_y - 1] \tag{3.10}$$

Thus, the velocity field for each component can be represented as

$$u(x) = \sum_{k_x=-\frac{N_x}{2}+1}^{\frac{N_x}{2}} \sum_{n_y=0}^{N_y-1} \sum_{k_z=-\frac{N_z}{2}+1}^{\frac{N_z}{2}} \tilde{u}_{k_x,n_y,k_z} \overline{T}_{n_y}(y) e^{2\pi i(\frac{k_x x}{L_x} + \frac{k_z z}{L_z})} \tag{3.11}$$

where the coefficients result from a combined Fourier transform in xz and a Chebyshev transform in y.
The velocity and pressure fields can be represented as a combination of constant and a perturbation. The velocity field is the sum of the base flow $U(y)\boldsymbol{e}_x$ and the perturbation velocity $\boldsymbol{u_{pert}}(\boldsymbol{x},t)$.

$$\boldsymbol{u}(\boldsymbol{x},t) = U(y)\boldsymbol{e}_x + \boldsymbol{u_{pert}}(\boldsymbol{x},t). \tag{3.12}$$

The total pressure field is the sum of a linear-in-x term $\pi_x(t)x$ and a periodic fluctuating pressure $p_{pert}(\boldsymbol{x},t)$. The gradient of this decomposition relates the total pressure gradient to a constant base pressure gradient $\pi_x \boldsymbol{e_x}$ and a fluctuating pressure gradient $\nabla p_{pert}(\boldsymbol{x},t)$.

$$p(\boldsymbol{x},t) = \pi_x(t)x + p_{pert}(\boldsymbol{x},t) \tag{3.13}$$

$$\nabla p(\boldsymbol{x},t) = \pi_x(t)\boldsymbol{e_x} + \nabla p_{pert}(\boldsymbol{x},t). \tag{3.14}$$

Substituting Eqns. 3.12 and 3.14 into 3.1 gives us

$$\frac{\partial \boldsymbol{u_{pert}}}{\partial t} + \nabla p = \nu \nabla^2 \boldsymbol{u_{pert}} - u.\nabla u + [\nu \frac{\partial^2 U}{\partial y^2} - \pi_x]\boldsymbol{e_x} \tag{3.15}$$

We shall henceforth refer to $\boldsymbol{u_{pert}}$ as $\boldsymbol{u}$ and p_{pert} as p for the sake of convenience. Using the rotational form to represent the convection term in Eqn. 3.15, we obtain

$$\frac{\partial \boldsymbol{u}}{\partial t} + \nabla[p + \frac{1}{2}\boldsymbol{u}\cdot\boldsymbol{u}] = \nu\nabla^2\boldsymbol{u} - [(\nabla \times \boldsymbol{u}) \times \boldsymbol{u} + U\frac{\partial \boldsymbol{u}}{\partial x} + v\frac{\partial U}{\partial y}\boldsymbol{e_x}] + [\nu\frac{\partial^2 U}{\partial y^2} - \pi_x]\boldsymbol{e_x} \tag{3.16}$$

which can be represented as

$$\frac{\partial \boldsymbol{u}}{\partial t} + \nabla \boldsymbol{q} = \boldsymbol{L}\boldsymbol{u} - \boldsymbol{N}\boldsymbol{u} + C, \tag{3.17}$$

where the nonlinear term $\boldsymbol{N}(\boldsymbol{u})$ are

$$\boldsymbol{N}(\boldsymbol{u}) \triangleq (\nabla \times \boldsymbol{u}) \times \boldsymbol{u} + U\frac{\partial \boldsymbol{u}}{\partial x} + v\frac{\partial U}{\partial y}\boldsymbol{e_x}, \tag{3.18}$$

the linear term $\boldsymbol{L}(\boldsymbol{u})$ represents

$$\boldsymbol{L}(\boldsymbol{u}) \triangleq \nu\nabla^2\boldsymbol{u}, \tag{3.19}$$

the modified pressure q represents

$$q \triangleq p + \frac{1}{2}\boldsymbol{u}\cdot\boldsymbol{u}, \tag{3.20}$$

and the constant term C (which is constant in $\boldsymbol{u}$ but not in time) represents

$$C \triangleq [\nu\frac{\partial^2 U}{\partial y^2} - \pi_x]\boldsymbol{e_x}. \tag{3.21}$$

The continuous Fourier transform (Eqn. 3.5) is applied and truncation is introduced. The Fourier-transformed operators for the gradient, the Laplacian, and the linear operator $\boldsymbol{L}$ are

$$\overline{\nabla_{k_x k_z}} \triangleq 2\pi i\frac{k_x}{L_x}\boldsymbol{e_x} + \frac{\partial}{\partial y}\boldsymbol{e_y} + 2\pi i\frac{k_z}{L_z}\boldsymbol{e_z}, \tag{3.22}$$

$$\overline{\nabla^2_{k_x k_z}} \triangleq \frac{\partial^2}{\partial y^2} - 4\pi^2(\frac{k_x^2}{L_x^2} + \frac{k_z^2}{L_z^2}), \tag{3.23}$$

$$\overline{\boldsymbol{L}}_{k_x k_z} \triangleq \nu\overline{\nabla}^2_{k_x k_z} \tag{3.24}$$

With these definitions, $\tilde{\nabla}\boldsymbol{q} = \overline{\nabla}\overline{q}$ and $\tilde{\boldsymbol{L}}\boldsymbol{u} = \overline{\boldsymbol{L}}\overline{u}$. For the sake of convenience, the subscripts k_x, k_z will be suppressed henceforth, and the fourier transform of Eqn. 3.17 can be written as

$$\frac{\partial \overline{u}}{\partial t} + \overline{\nabla}\overline{q} = \overline{\boldsymbol{L}}\overline{u} - \tilde{\boldsymbol{N}}(u) + \overline{C} \tag{3.25}$$

We consider the Crank-Nicolson/Adams-Bashforth (CNAB) time integration scheme, the terms in Eqn. 3.24 are approximated at $t = (n - 1/2)\Delta t$ as

$$\frac{\partial}{\partial t}\overline{u}^{n+1/2} = \frac{\overline{u}^{n-1} - \overline{u}^{n}}{\Delta t} + O(\Delta t^2) \tag{3.26}$$

$$\overline{\boldsymbol{L}}\overline{u}^{n+1/2} = \frac{1}{2}\overline{\boldsymbol{L}}\overline{u}^{n+1} + \frac{1}{2}\overline{\boldsymbol{L}}\overline{u}^{n} + O(\Delta t^2) \tag{3.27}$$

$$\overline{\nabla}\overline{q}^{n+1/2} = \frac{1}{2}\overline{\nabla}\overline{q}^{n+1} + \frac{1}{2}\overline{\nabla}\overline{q}^{n} + O(\Delta t^2) \tag{3.28}$$

$$\overline{\boldsymbol{N}}^{n+1/2} = \frac{3}{2}\overline{\boldsymbol{N}}^{n} - \frac{1}{2}\overline{\boldsymbol{N}}^{n-1} + O(\Delta t^2) \tag{3.29}$$

$$\overline{C}^{n+1/2} = \frac{1}{2}\overline{C}^{n+1} - \frac{1}{2}\overline{C}^{n} + O(\Delta t^2) \tag{3.30}$$

The approximation for the linear terms is called Crank-Nicolson, and that for the nonlinear term is Adams-Bashforth. Using these approximations in Eqn. 3.25 and rearranging yields

$$[\frac{1}{\Delta t} - \frac{1}{2}\overline{\boldsymbol{L}}]\overline{u}^{n+1} + \frac{1}{2}\overline{\nabla}q^{n+1} = [\frac{1}{\Delta t} + \frac{1}{2}\overline{\boldsymbol{L}}]\overline{u}^{n} - \frac{1}{2}\overline{\nabla}q^{n} + \frac{3}{2}\overline{\boldsymbol{N}}^{n} - \frac{1}{2}\overline{\boldsymbol{N}}^{n-1} + \frac{1}{2}\overline{C}^{n+1} + \frac{1}{2}\overline{C}^{n} \tag{3.31}$$

At this point, the $O(t^2)$ terms are neglected, and this Eqn. 3.31 is taken as the update rule for the approximate solution $\overline{u}^{n+1}$. This process is continued until the end of the time loop in the code. The time step, Δt is variable between $\Delta t_{min} = 0.01$ and $\Delta t_{max} = 0.03125$ for computations on the lower-order grid (for $N_x \times N_y \times N_z = 32 \times 65 \times 32$) and varies between $\Delta t_{min} = 0.001$ and $\Delta t_{max} = 0.003125$ for computations on the lower-order grid (for $N_x \times N_y \times N_z = 32 \times 129 \times 32$).
A huge advantage of using *Channelflow* is that the *Channelflow* library contains a number of high-level algorithms for computing exact solutions like equilibria, travelling waves, periodic orbits and relative periodic orbits.

3.2 Newton-Krylov-Hookstep method

One of the methods that has been used to look for equilibria and travelling waves of the plane Poiseuille flow in this thesis is the iterative Newton-Krylov-Hookstep method developed by Viswanath [74]. If the time-t map of the Navier-Stokes computed by the DNS (direct numerical simulation) is given by $\Phi^t(u)$ and σ represents a translation in both the x and z directions of the flow (consisting of 2 components, the shift in x and z), we seek solutions of the equation

$$G(u, \sigma, t) = \sigma\Phi^t(u) - u = 0 \tag{3.32}$$

Let $x = (u, \sigma, t)$ be the vector being sought, and $x^* = (u^*, \sigma^*, t^*)$ be the solution, i.e. $G(x^*) = G(u^*, \sigma^*, t^*) = 0$. Assuming that $x^* = x + dx$ and $G(x^*) = G(x + dx_N)$ where the subscript N refers to the Newton step, and dropping the higher order terms, we get

$$DG(x)dx_N = -G(x). \tag{3.33}$$

$D(G)$ represents the Jacobian of G. This defines an iterative process terminated only once $G(x)$ is small enough.

In order to have a unique solution dx_N, this system is supplemented by three constraint equations,

$$(du_N, du/dt) = 0 \tag{3.34}$$
$$(du_N, du/d(\Delta x)) = 0 \tag{3.35}$$
$$(du_N, du/d(\Delta z)) = 0 \tag{3.36}$$

where $(,)$ signifies an inner product. These are orthogonality constraints preventing the Newton step from going in the directions of the time, x, and z equivariance. If we consider the dimensionality of u to be M, and the symmetry operator σ to have a dimension of 2 (including the shifts in the x and the z directions), then we get an $(M+3) \times (M+3)$ dimensional system

$$\boldsymbol{A}\ dx_N = b. \tag{3.37}$$

Since M is very large, the iterative GMRES Krylov-subspace algorithm is used to find an approximate solution dx_N to the $(M+3) \times (M+3)$ system $\boldsymbol{A}\ dx_N = b$. However if one is too far from the solution x^*, the linearization inherent in the Newton algorithm will not be accurate.

3.3 Arnoldi method

The Arnoldi algorithm implemented within *Channelflow* is used to calculate the stability characterisitcs of exact coherent structures. Consider a time-integration map

$$F^T : \boldsymbol{u} \to \boldsymbol{u}(t+T) \tag{3.38}$$

which integrates a flow field a time T forward in time. For a fixed point $\boldsymbol{u}^*$ of F^T, we have

$$F^T(\boldsymbol{u}^*) = \boldsymbol{u}^*. \tag{3.39}$$

For a small deviation $d\boldsymbol{u}$ from $\boldsymbol{u}$, an operator $L(\boldsymbol{u}^*)(d\boldsymbol{u})$ can be defined as

$$L(\boldsymbol{u}^*)(d\boldsymbol{u}) \equiv L\ d\boldsymbol{u} := F^T(\boldsymbol{u}^* + d\boldsymbol{u}) - \boldsymbol{u}^* \tag{3.40}$$

This operator describes how small disturbances to the fixed point $\boldsymbol{u}^*$ develop and thus its eigenvalues can be used as an indicator of the stability of an equilibrium solution. Here L is a matrix of very high dimensionality. Hence instead of calculating the eigenvalues of L directly, Krylov subspace methods are applied. For a given matrix L and a starting vector q, the m-th Krylov-subspace $\mathcal{K}_m(L, q)$ as

$$\mathcal{K}_m(L, q) := \{q, Lq, Lq^2, ..., Lq^m\}. \tag{3.41}$$

Using the Arnoldi iteration, an orthogonal projection of L on the Krylov-subspace is calculated. After m such steps, the orthogonal projection of L on the m-th Krylov-subspace is obtained, which is denoted by H_m. The eigenvalues of H_m approximate those of L and coincide if m is equal to the dimension of matrix L. To get an approximation of

the eigenvalues of L, the eigenvalues of H_m are calculated. The eigenvalues of H_m converge first to the eigenvalues of L with largest real part which are also the relevant eigenvalues for a stability analysis. Since only the matrix vector products are used, it is not necessary to calculate and save the matrix L.

3.4 Bisection

Bisection is one of the classical methods to achieve the restriction of a flow trajectory to the manifold separating the laminar basin and the turbulent basin in the phase space. The basic idea of the bisection algorithm has been introduced in section 1.7.3. As explained in section 1.7.3, at the end of the bisection process, we obtain an initial condition $\boldsymbol{u} = \boldsymbol{u_L} + \lambda(\boldsymbol{u_T} - \boldsymbol{u_L})$ that lies closest to the edge. But since the edge state is an unstable solution, the trajectory soon departs from the edge. To determine whether a trajectory has sufficiently deviated from the edge towards either the laminar state or the turbulent state, an observable related to the flow is continuously monitored. One of the usual observables is the kinetic energy of the flow

$$E(t) = 1/2 \int_0^{Lx} \int_0^{Lz} \int_{-1}^{1} \boldsymbol{u}^2 dxdzdy. \tag{3.42}$$

The value of $E(t)$ expectedly approaches 0 when the flow approaches the laminar state, but does not change drastically for the edge states compared to the turbulent states. Since the streamwise vortices of edge states are weak in strength, a better choice for the observable would be the energy associated with the wall-normal component of the velocity v, given by

$$E_v(t) = 1/2 \int_0^{Lx} \int_0^{Lz} \int_{-1}^{1} v^2 dxdzdy. \tag{3.43}$$

The value of E_v for the edge states is lower than the corresponding value for turbulent flow by a few decades, and hence E_v is clearly a better observable to monitor the flow evolution. After observing a few test cases, suitably chosen upper and lower thresholds for E_v are set, beyond/below which the flow is considered to be surely approaching the turbulent/laminar state. The values of the thresholds in our simulations were generally around $(E_v)_T \approx 5\times10^{-4}$ above which the flow was deemed to be approaching the turbulent state, and $(E_v)_L \approx 5\times10^{-7}$ below which the flow was considered to be converging towards the laminar solution.
Each time the upper or the lower threshold is crossed, the flow is restarted with a new initial condition belonging to the family $\boldsymbol{u} = \boldsymbol{u_L} + \lambda(\boldsymbol{u_T} - \boldsymbol{u_L})$.
When the value of the initial amplitude $\boldsymbol{u}$ has been refined to the 16^{th} decimal, machine precision is reached and the value of $\boldsymbol{u}$ cannot be refined further. When the edge state has been tracked for a certain amount of time in the state space, the process of bisection has to be restarted with a new set of appropriately chosen value of λ for $\boldsymbol{u_L}$ and $\boldsymbol{u_T}$.

3.5 Quotienting

As discussed in section 1.7.2, the presence of continuous symmetries makes it harder to find exact coherent solutions like steady states and periodic orbits. Several attempts

have been made to rid the system of the degeneracy induced by the continuous symmetries without any other loss of information. This process of "removing" the symmetries inherent to the system is known as "quotienting". Cvitanović *et al.* describe a "template-based" quotienting method in [10] and [75], where they choose a known solution of the flow, say an upper branch solution $\boldsymbol{u_{UB}}$ as a "template" and "reduce" (as explained in the subsequent paragraph) all the states to this one. Similar successful template-based methods have been implemented by Willis *et al.* in pipe flow [32] and [11] based on the knowledge of exact solutions, and Budanur *et al.* in [76] using the first fourier mode as template for quotienting. Attempts to quotient out the symmetries using a different method known as the "geometric-phase" method, without the dependence on a template have been done by Rowley *et al.* in [77], and by Kreilos et. al in [78].

We initially attempted to quotient out the symmetries in our system using a fixed template method, and then tried to extend the method to make it independent of this fixed template. We started by choosing one of the snapshots in our flow $u(t^*)$, as the "reference field" or the "template". The shift which minimises the distance between a given snapshot $u(t), t > t^*$ and the desired template $u(t^*)$ is identified using a Newton optimisation scheme described below. We thus achieve the "reduction" of continuous symmetries in the streamwise and the spanwise direction. The method described here uses a single template or a "fixed template" to which all the snapshots in the flow are compared for symmetry reduction. This gives rise to a disadvantage : even though the flow does not deviate a lot between any two time instants t^* and $t > t^*$ when the flow is close to the laminar attractor, the flow field at a certain time instant might be drastically different from the "reference field" obtained just a few instants earlier when the flow is turbulent and chaotic. This makes the "fixed template", a bad initial condition to the Newton optimisation scheme, especially for quotienting turbulent flows.

As an alternative, we implemented another method of quotienting wherein the "reference field" is not a fixed snapshot. We choose an already-quotiented flow field which occurs in the flow just a few time units earlier (in practice one time unit earlier in units of h/U_{cl}) as the "reference field", i.e. $t^* = t - dt$ with $dt = 1$. Hence in this method, we have a "moving template" as opposed to the "fixed template" in the earlier method.

We now describe the optimisation algorithm. We first take the two snapshots, the "reference field", u_{ref} (which could be a fixed or a moving template) and the flow field $v(t)$ at any given time instant, t. Firstly the streamwise length of the domain is discretised into 100 parts, and a landscape of the domain is created, where the L-2 distance between any two locations is plotted, and the minimum distance in the streamwise direction is identified, so as to get a rough estimate of the x-shift for the initialisation of the Newton algorithm.

The state-space distance in the full state space between two flow fields v and u_{ref} is defined as follows :

$$\begin{aligned} G(\triangle x) &= ||\sigma_{\triangle x} v - u_{ref}||^2 \\ &= \langle \sigma_{\triangle x} v - u_{ref}, \sigma_{\triangle x} v - u_{ref} \rangle, \end{aligned} \tag{3.44}$$

where $(\sigma_{\triangle x} v)(x) = v(x - \triangle x)$ by definition.

Here, $G(\triangle x)$ needs to be minimised, which necessitates that the first derivative of $G(\triangle x)$ should be zero, and the second derivative of $G(\triangle x)$ should be positive.

We compute the first and second derivative of $G(\triangle x)$ as follows :

$$\frac{d}{d(\triangle x)}G(\triangle x) = 2\langle\frac{d}{d(\triangle x)}(\sigma_{\triangle x}v), (\sigma_{\triangle x}v - u_{ref})\rangle = 0 \tag{3.45}$$

with the constraint that

$$\frac{d^2}{d(\triangle x)^2}G(\triangle x) = 2\langle\frac{d}{d(\triangle x)}(\sigma_{\triangle x}v), \frac{d}{d(\triangle x)}(\sigma_{\triangle x}v)\rangle + 2\langle\frac{d^2}{d(\triangle x)^2}(\sigma_{\triangle x}v), (\sigma_{\triangle x}v - u_{ref})\rangle > 0 \tag{3.46}$$

We would like to have a generalisation of this minimisation procedure to 2D shifts since shifts are encountered in both the x and z directions in practice. We define the functional $G(\triangle x, \triangle z)$ as the distance between two fields, a reference field u_{ref} and a flow field in time v, as follows :

$$G(\triangle x, \triangle z) = ||\sigma_{\triangle x, \triangle z}v - u_{ref}||^2, \tag{3.47}$$

where $(\sigma_{\triangle x, \triangle z}v)(x, y, z) = v(x - \triangle x, y, z - \triangle z)$
For the sake of convenience, henceforth $\triangle x$ shall be referred to as x, $\triangle z$ as z, and u_{ref} as u.
Similarly to the one-dimensional case earlier, in order to minimise the functional $G(x, z)$, we need to find the values of x and z for which its gradient, ∇G is zero, and the Hessian, $H[G] = J(\nabla G)$ is definite positive.
The gradient and the Hessian of G are computed as follows :

$$\begin{aligned}\nabla G &= (\frac{\partial G}{\partial x}, \frac{\partial G}{\partial z}) \\ &= (2\langle\frac{d}{dx}(\sigma_{x,z}v), (\sigma_{x,z}v - u)\rangle, 2\langle\frac{d}{dz}(\sigma_{x,z}v), (\sigma_{x,z}v - u)\rangle)\end{aligned} \tag{3.48}$$

and

$$\begin{aligned}H[G] &= J(\nabla G) \\ &= J(\frac{\partial G}{\partial x}, \frac{\partial G}{\partial z}) \\ &= \frac{\partial(\frac{\partial G}{\partial x}, \frac{\partial G}{\partial z})}{\partial(x, z)} \\ &= \begin{bmatrix} T_1 & T_2 \\ T_3 & T_4 \end{bmatrix}\end{aligned} \tag{3.49}$$

The terms T_1, T_2, T_3 and T_4 used in Eqn. 3.49 stand for :

$$\begin{aligned}T_1 &= \frac{\partial(\frac{\partial G}{\partial x})}{\partial x} \\ &= \frac{\partial}{\partial x}(2\langle\frac{d}{dx}(\sigma_{x,z}v), (\sigma_{x,z}v - u)\rangle) \\ &= 2(\langle\frac{d^2}{dx^2}(\sigma_{x,z}v), (\sigma_{x,z}v - u)\rangle + \langle\frac{d}{dx}(\sigma_{x,z}v), \frac{d}{dx}(\sigma_{x,z}v)\rangle)\end{aligned} \tag{3.50}$$

$$
\begin{aligned}
T_2 &= \frac{\partial(\frac{\partial G}{\partial x})}{\partial z} \\
&= \frac{\partial}{\partial z}(2\langle\frac{d}{dx}(\sigma_{x,z}v),(\sigma_{x,z}v-u)\rangle) \\
&= 2(\langle\frac{d^2}{dxdz}(\sigma_{x,z}v),(\sigma_{x,z}v-u)\rangle + \langle\frac{d}{dx}(\sigma_{x,z}v),\frac{d}{dz}(\sigma_{x,z}v)\rangle)
\end{aligned} \tag{3.51}
$$

$$
\begin{aligned}
T_3 &= \frac{\partial(\frac{\partial G}{\partial z})}{\partial x} \\
&= \frac{\partial}{\partial x}(2\langle\frac{d}{dz}(\sigma_{x,z}v),(\sigma_{x,z}v-u)\rangle) \\
&= 2(\langle\frac{d^2}{dxdz}(\sigma_{x,z}v),(\sigma_{x,z}v-u)\rangle + \langle\frac{d}{dz}(\sigma_{x,z}v),\frac{d}{dx}(\sigma_{x,z}v)\rangle)
\end{aligned} \tag{3.52}
$$

$$
\begin{aligned}
T_4 &= \frac{\partial(\frac{\partial G}{\partial z})}{\partial z} \\
&= \frac{\partial}{\partial z}(2\langle\frac{d}{dz}(\sigma_{x,z}v),(\sigma_{x,z}v-u)\rangle) \\
&= 2(\langle\frac{d^2}{dz^2}(\sigma_{x,z}v),(\sigma_{x,z}v-u)\rangle + \langle\frac{d}{dz}(\sigma_{x,z}v),\frac{d}{dz}(\sigma_{x,z}v)\rangle)
\end{aligned} \tag{3.53}
$$

For the sake of simplicity, let us refer to the following terms as shown :

$$(\sigma_{x,z}v-u) = T_u \tag{3.54}$$

$$\frac{d}{dx}(\sigma_{x,z}v) = T_x \tag{3.55}$$

$$\frac{d}{dz}(\sigma_{x,z}v) = T_z \tag{3.56}$$

$$\frac{d^2}{dx^2}(\sigma_{x,z}v) = T_{xx} \tag{3.57}$$

$$\frac{d^2}{dz^2}(\sigma_{x,z}v) = T_{zz} \tag{3.58}$$

and

$$\frac{d^2}{dxdz}(\sigma_{x,z}v) = \frac{d^2}{dzdx}(\sigma_{x,z}v) = T_{xz} \tag{3.59}$$

giving us the gradient and the Hessian of the functional $G(x,z)$ as shown in Eqns. 3.48 and 3.49 to be

$$\nabla G = 2(\langle T_x, T_u\rangle, \langle T_z, T_u\rangle) \tag{3.60}$$

and

$$H[G] = 2\begin{bmatrix} (\langle T_{xx}, T_u\rangle + \langle T_x, T_x\rangle) & (\langle T_{xz}, T_u\rangle + \langle T_x, T_z\rangle) \\ (\langle T_{xz}, T_u\rangle + \langle T_z, T_x\rangle) & (\langle T_{zz}, T_u\rangle + \langle T_z, T_z\rangle) \end{bmatrix} \tag{3.61}$$

The terms represented in Eqns. 3.55 to 3.59 are evaluated as follows :

$$\begin{aligned} T_x &= \frac{d}{dx}(\sigma_{x,z}v) \\ &= \sigma_{x,z}(\frac{\sigma_{\delta x,0}v - u}{\delta x}) \end{aligned} \tag{3.62}$$

$$\begin{aligned} T_z &= \frac{d}{dz}(\sigma_{x,z}v) \\ &= \sigma_{x,z}(\frac{\sigma_{0,\delta z}v - u}{\delta z}) \end{aligned} \tag{3.63}$$

$$\begin{aligned} T_{xx} &= \frac{d^2}{dx^2}(\sigma_{x,z}v) \\ &\simeq \frac{\sigma_{x+\delta x,z}v - 2\sigma_{x,z}v + \sigma_{x-\delta x,z}v}{2\delta x} \\ &= \sigma_{x,z}(\frac{\sigma_{\delta x,0}v - 2v + \sigma_{-\delta x,0}v}{2\delta x}) \end{aligned} \tag{3.64}$$

$$\begin{aligned} T_{zz} &= \frac{d^2}{dz^2}(\sigma_{x,z}v) \\ &\simeq \frac{\sigma_{x,z+\delta z}v - 2\sigma_{x,z}v + \sigma_{x,z-\delta z}v}{2\delta z} \\ &= \sigma_{x,z}(\frac{\sigma_{0,\delta z}v - 2v + \sigma_{0,-\delta z}v}{2\delta z}) \end{aligned} \tag{3.65}$$

$$\begin{aligned} T_{xz} = T_{zx} &= \frac{d^2}{dxdz}(\sigma_{x,z}v) \\ &\simeq \frac{d}{dx}(\frac{\sigma_{x,z+\delta z}v - \sigma_{x,z}v}{\delta z}) \\ &= \frac{1}{\delta z}(\frac{\sigma_{x+\delta x,z+\delta z}v - \sigma_{x,z+\delta z}v}{\delta x}) - \frac{1}{\delta z}(\frac{\sigma_{x+\delta x,z}v - \sigma_{x,z}v}{\delta x}) \\ &= \sigma_{x,z}(\frac{\sigma_{\delta x\delta z}v - \sigma_{\delta x,0}v - \sigma_{0,\delta z}v + v}{\delta x\delta z}) \end{aligned} \tag{3.66}$$

3.6 Visualisation

Different methods of visualisation of the flow fields are used according to the context. 3D data is visualised in 2D, using a routine provided in *Channelflow*, by extracting the values of the different components of velocities in specific xy, yz and xz planes. For instance, the velocities in the xy plane are extracted at $z = 0$ and $z = L_z$, in the yz plane at $x = 0$ and $x = L_x$, and in the xz plane at $y = L_y/2$.

3D visualisation was performed using the open-source application ParaView [79]. The streamwise velocity contours were plotted and the vortical structures were represented using the Q-criterion. The Q-criterion defines a vortex as a "connected fluid region with a positive second invariant of $\nabla \boldsymbol{u}$". [80]

$$Q = \frac{1}{2}||\bar{\Omega}||^2 - ||\bar{S}||^2 \tag{3.67}$$

where, Ω_{ij} is the vorticity tensor, S_{ij} is the rate-of-strain tensor, and $||\cdot||$ represents the usual $L-2$ norm defined by the inner product of a quantity with itself.

$$\Omega_{ij} = \frac{1}{2}(\frac{\partial u_i}{\partial x_j} - \frac{\partial u_j}{\partial x_i}) \tag{3.68}$$

$$S_{ij} = \frac{1}{2}(\frac{\partial u_i}{\partial x_j} + \frac{\partial u_j}{\partial x_i}) \tag{3.69}$$

Q represents the local balance between the rate of shear-strain and the vorticity magnitude, and the Q-criterion defines vortices as volumes where the vorticity magnitude is greater than the magnitude of rate-of-strain, i.e., $Q > 0$.
Fig. 3.1 shows the contours of vorticity obtained using the Q-criterion in a turbulent channel of domain size $L_x \times L_y \times L_z = 2.5 \times 2 \times 1.25$ where $Re_\tau = 80$. In practice, the best iso-surface of Q for visualisation is chosen through trial and error.

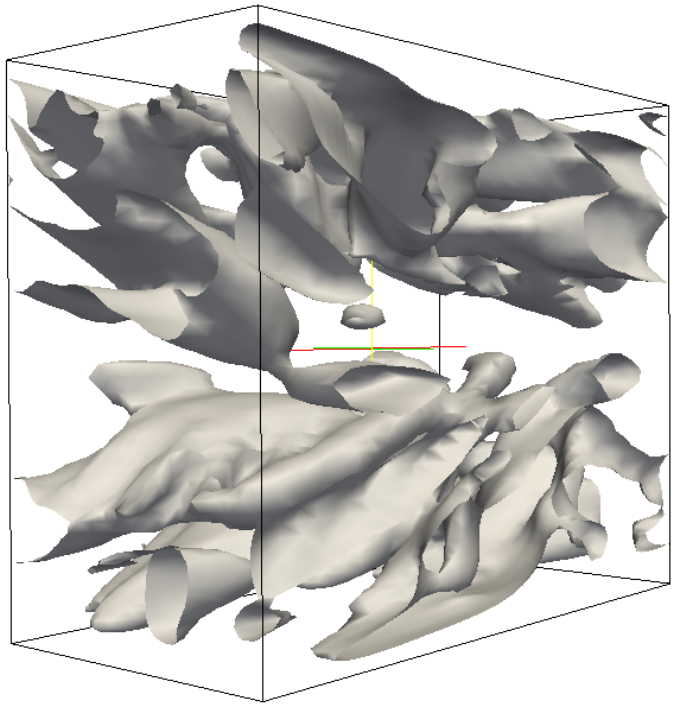

Figure 3.1: Iso-surfaces of $Q = +0.09$ representing vortical structures in a turbulent simulation at $Re_\tau = 80$. Flow is from left to right.

Chapter 4

Turbulence in periodic channels

In this chapter, the results obtained from the turbulent simulations in channels of different dimensions will be discussed. We start with computations in large domains, and move on to the minimal flow channels. The large channels which are discussed in the beginning have a streamwise and spanwise domain wavelength which is four times that of the minimal flow unit (M.F.U.) considered subsequently. We also present mean profiles statistics in all cases.

4.1 Computations in large domains, $L_x^+ \times L_z^+ = 800 \times 400$

In this section, turbulent simulations were carried out in a channel of dimensions $L_x^+ \times L_z^+ = 800 \times 400$, for a range of Re_τ starting from $Re_\tau = 60$ to $Re_\tau = 100$. These channels are not large enough for us to observe the spots or stripes as seen in Chapter 1 but are sufficiently large to capture the dynamics of large scale flow amongst the near-wall streaks. All computations in this section were carried out in channels whose numerical resolution was $N_x \times N_y \times N_z = 128 \times 65 \times 128$.
Table 4.1 lists the different values of Re_τ for which these computations have been carried out, along with their respective domain sizes in outer units and inner units.

4.1.1 Visualisations

A 3D visualisation of a turbulent snapshot at $Re_\tau = 100$ in a channel of dimensions $L_x^+ \times L_z^+ = 800 \times 400$ is shown in Fig. 4.1.

Re_τ	L_x	L_z	L_x^+	L_z^+
60	13.32	6.66	800	400
70	11.44	5.72	800	400
80	10	5	800	400
100	8	4	800	400

Table 4.1: Channel dimensions of the large channels in outer and inner units, for different Re_τ.

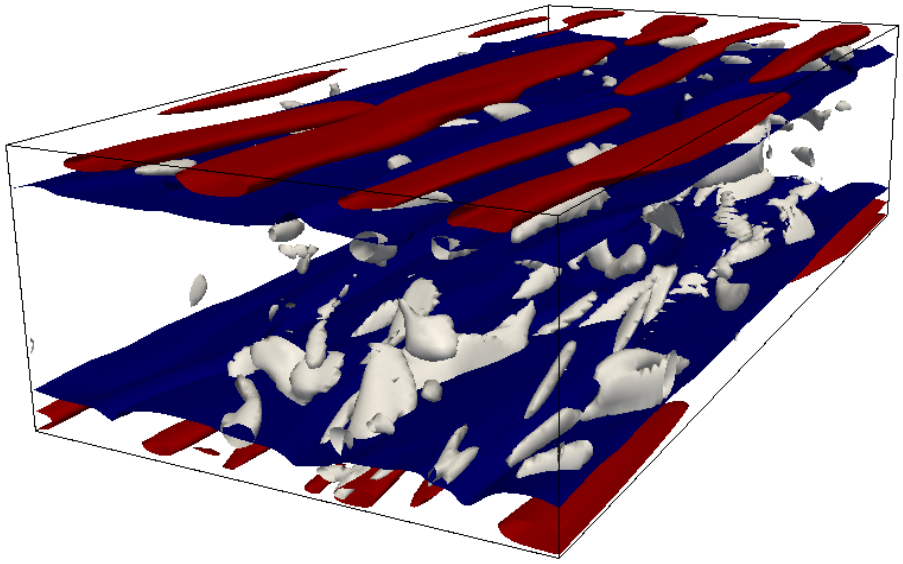

Figure 4.1: Iso-surfaces of $u = +0.05$ in red, $u = -0.5$ in blue, $Q = +0.1$ in grey in a turbulent simulation at $Re_\tau = 100$ in a channel of dimensions $L_x^+ \times L_z^+ = 800 \times 400$, flow is from left to right

We see that turbulent activity is spread over both the walls, with the presence of streamwise vortices and near-wall streaks.
To have a neater visualisation of the positive and the negative streaks throughout the domain, we plot the contours of streamwise velocity in the yz plane at $Re_\tau = 70$, where the spanwise and wall-normal velocities are represented through the vectors in Fig. 4.2.

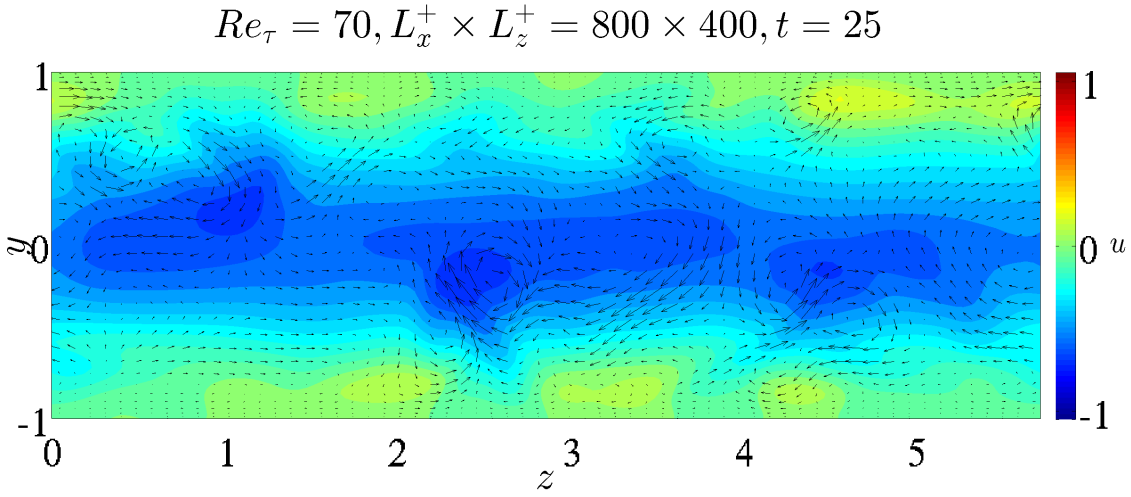

Figure 4.2: The contours of u in the yz plane in a turbulent simulation at $Re_\tau = 70$ in a channel of dimensions $L_x^+ \times L_z^+ = 800 \times 400$

A corresponding 3D visualisation of the same flow field is shown in Fig. 4.3 where the

structures in red correspond to iso-surfaces of $u = +0.1$. They represent the positive streaks. The structures in blue correspond to iso-surfaces of $u = -0.5$. They represent the negative streaks. The structures in grey correspond to iso-surfaces of $Q = +1$.

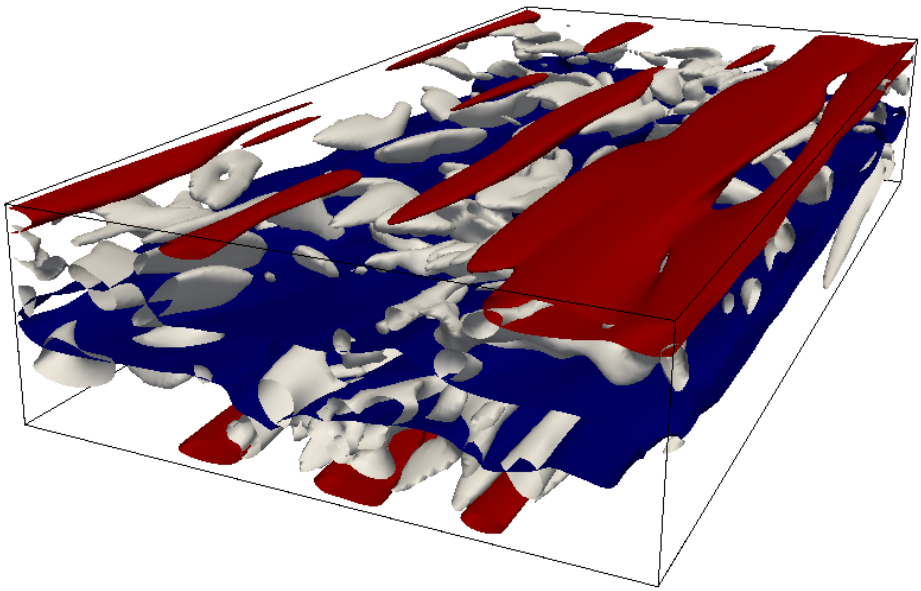

Figure 4.3: Iso-surfaces of $u = +0.1$ in red, $u = -0.5$ in blue, $Q = +3$ in grey in a turbulent simulation at $Re_\tau = 70$ in a channel of dimensions $L_x^+ \times L_z^+ = 800 \times 400$

We see in Fig. 4.1 four positive streaks found near the walls. Fig. 4.3 shows the presence of five streaks near the top wall, and three streaks near the bottom wall, which gives again a rough average of four streaks near the wall. Considering the domain size to be $L_z^+ = 400$, this gives an indication that the average streak spacing in the spanwise direction is around 100 inner units which corresponds well with the earlier observations of Jimenéz and Moin [1].

4.1.2 Statistics

We compute the contribution of each wall to the turbulence, and quantify it using the asymmetry variables as described below.

$$s_u = \frac{\int_{-1}^{0} u_{rms}(y,t)dy - \int_{0}^{1} u_{rms}(y,t)dy}{\int_{-1}^{0} u_{rms}(y,t)dy + \int_{0}^{1} u_{rms}(y,t)dy} \tag{4.1}$$

$$s_v = \frac{\int_{-1}^{0} v_{rms}(y,t)dy - \int_{0}^{1} v_{rms}(y,t)dy}{\int_{-1}^{0} v_{rms}(y,t)dy + \int_{0}^{1} v_{rms}(y,t)dy} \tag{4.2}$$

$$s_w = \frac{\int_{-1}^{0} w_{rms}(y,t)dy - \int_{0}^{1} w_{rms}(y,t)dy}{\int_{-1}^{0} w_{rms}(y,t)dy + \int_{0}^{1} w_{rms}(y,t)dy} \tag{4.3}$$

where the r.m.s. velocity is computed as

$$u_{rms}(y,t) = \sqrt{\frac{\sum_{i,j}(u(x_i,z_j,y,t) - \hat{u}(k_x=0,k_z=0,y,t))^2}{N_x N_z}} \tag{4.4}$$

$$v_{rms}(y,t) = \sqrt{\frac{\sum_{i,j}(v(x_i,z_j,y,t) - \hat{v}(k_x=0,k_z=0,y,t))^2}{N_x N_z}} \tag{4.5}$$

$$w_{rms}(y,t) = \sqrt{\frac{\sum_{i,j}(w(x_i,z_j,y,t) - \hat{w}(k_x=0,k_z=0,y,t))^2}{N_x N_z}} \tag{4.6}$$

The r.m.s. velocity is computed by taking the mean of the fluctuations of velocity along the streamwise and spanwise directions. We introduce the asymmetry variables to assess the contribution of each wall separately, and to monitor whether turbulence is equally distributed over both the walls or restricted to one of the walls. The channel is cut in two equal parts along the $y = 0$ plane, and the difference in contribution between the two halves is computed. From their definition in Eqns. 4.1, 4.2 and 4.3, the asymmetry variables, s_u, s_v and s_w turn out to be positive if the lower wall has a greater contribution than the upper wall i.e. if the turbulent structures are localised more near the lower wall; and vice versa. All integrals were computed using the trapezoidal rule.
The resulting plots of s_u *vs* t for some of the Re_τ are shown in Fig. 4.4.

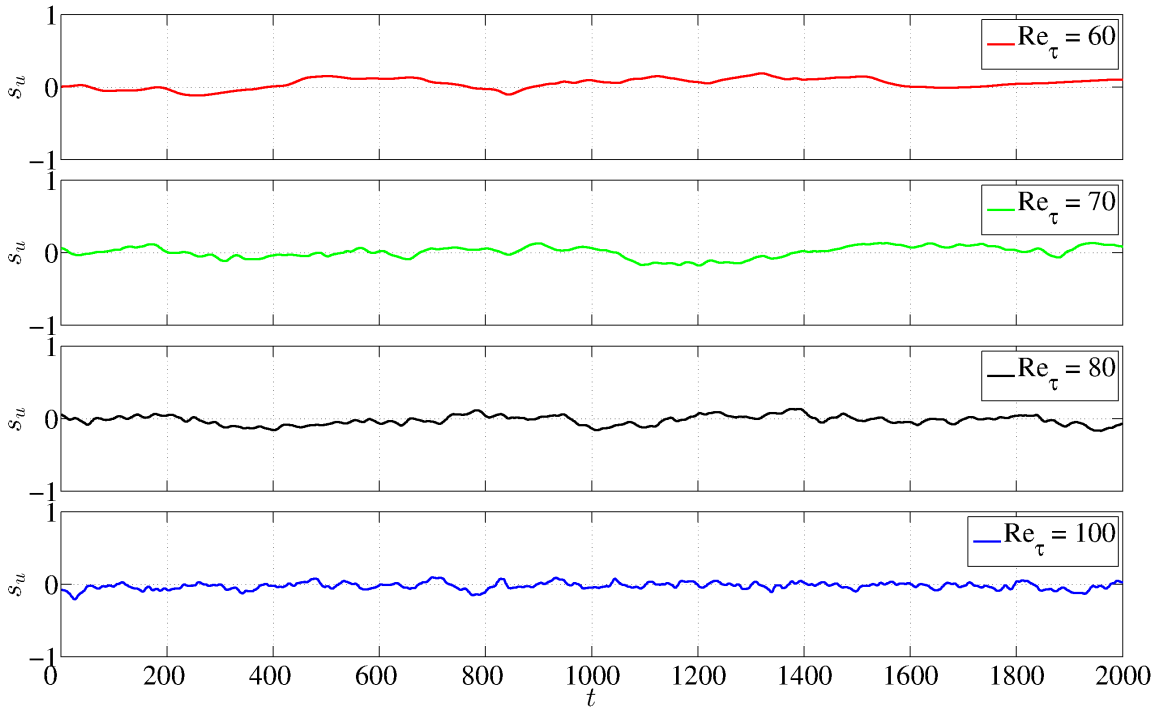

Figure 4.4: Asymmetry variable s_u for the turbulent simulations at different Re_τ w.r.t time (in units of U_{cl}/h).

The value of $|s_u|$ in Fig. 4.4 hardly exceeds 0.2. Though the instantaneous value fluctuates, the mean value is very close to zero, thereby indicating that there is an equally strong

contribution to the formation of turbulent structures from both walls. It is expected that the mean value gets closer and closer to zero with increasing simulation time.
The time-averaged r.m.s. velocity profiles, $< u_{rms}(y) >$ are computed for turbulent simulations at all the Re_τ, as shown below :

$$< u_{rms}(y) >= \frac{1}{T}\int_0^T u_{rms}(y,t)dt \tag{4.7}$$

$$< v_{rms}(y) >= \frac{1}{T}\int_0^T v_{rms}(y,t)dt \tag{4.8}$$

$$< w_{rms}(y) >= \frac{1}{T}\int_0^T w_{rms}(y,t)dt \tag{4.9}$$

The plot of $< u_{rms}(y) >$ vs y in outer units as well as inner units is shown below in Figs. 4.5 and 4.6.

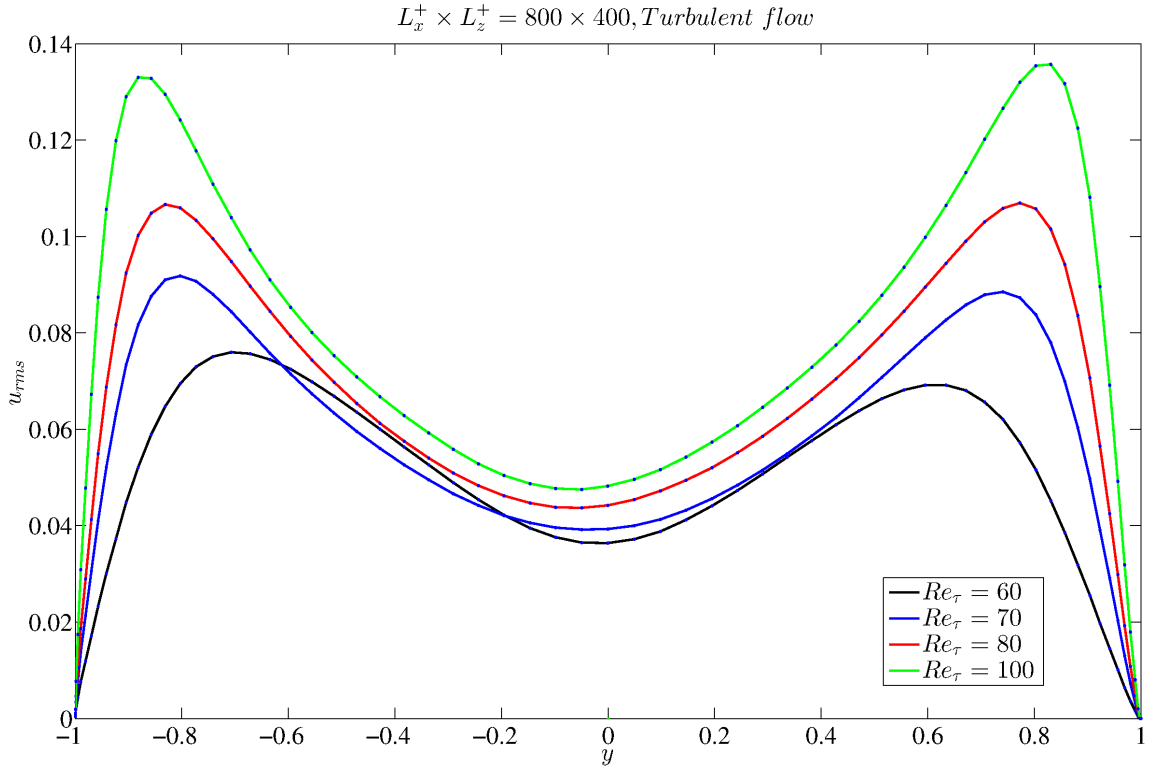

Figure 4.5: R.m.s. velocity profiles $< u_{rms}(y) >$ of the turbulent simulations at different Re_τ in a channel of dimensions $L_x^+ \times L_z^+ = 800 \times 400$, plotted in outer units

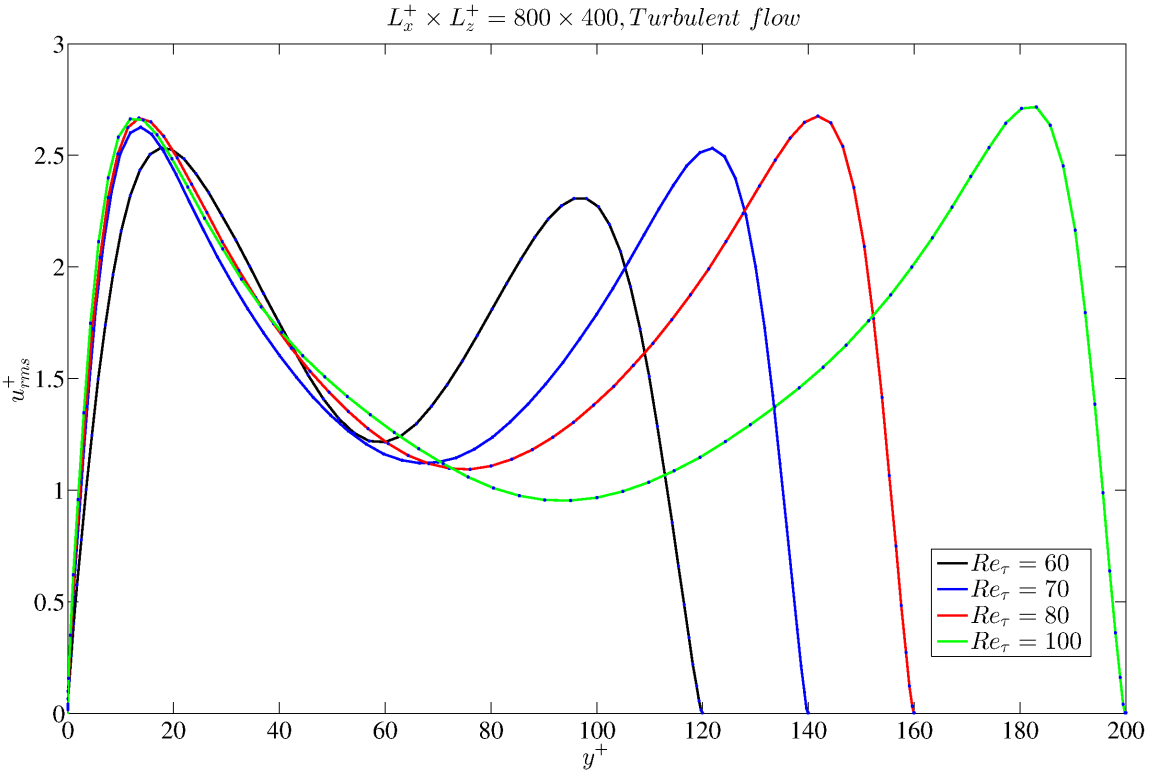

Figure 4.6: R.m.s. velocity profiles $< u_{rms}(y) >$ of the turbulent simulations at different Re_τ in a channel of dimensions $L_x^+ \times L_z^+ = 800 \times 400$, plotted in inner units

In Figs. 4.5 and 4.6, when plotted in outer units, the profiles of $< u_{rms} >$ shows a gradually increasing trend, that is, $max(< u_{rms} >)$ increases with Re_τ, as also the y-location of the maximum, $y_{max} = y|_{max<u_{rms}>}$. Yet when plotted in inner units, the maximum value, $max(< u_{rms} >)$ collapses to a single value at a fixed y-location, displaying self-similarity as expected from most turbulent simulations of shear flows, e.g. [81]. Hence there is clear self-similarity only when the profiles of near-wall turbulence are plotted in inner units.

4.2 Computations in minimal flow unit channels, $L_x^+ \times L_z^+ = 200 \times 100$

Turbulent simulations were carried out in a channel of domain size in inner units being, $L_x^+ \times L_z^+ = 200 \times 100$, at different Re_τ. Note that L_x^+ is slightly smaller than the values considered in [1]. The channel size in outer units varied depending on the Re_τ.
The dimensions of the channel in inner and outer units, along with the resolution used, for different Re_τ are shown in Table 4.2.

4.2.1 Statistics and visualisations

The variation of the asymmetry variables w.r.t. t is shown in Fig. 4.7 for a few values of Re_τ.
For low values of Re_τ, for example, at $Re_\tau = 80$, the turbulent structures are not necessarily confined to a single wall, and are unevenly distributed for finite durations of time

Re_τ	L_x	L_z	L_x^+	L_z^+	$N_x \times N_y \times N_z$
60	3.33	1.67	200	100	$32 \times 65 \times 32$
70	2.86	1.43	200	100	$32 \times 65 \times 32$
80	2.5	1.25	200	100	$32 \times 65 \times 32$
100	2	1	200	100	$32 \times 65 \times 32$
120	1.67	0.83	200	100	$32 \times 129 \times 32$
150	1.33	0.67	200	100	$32 \times 129 \times 32$
180	1.11	0.56	200	100	$32 \times 129 \times 32$

Table 4.2: Channel dimensions in outer and inner units along with corresponding resolution in the M.F.U. channel, for different Re_τ

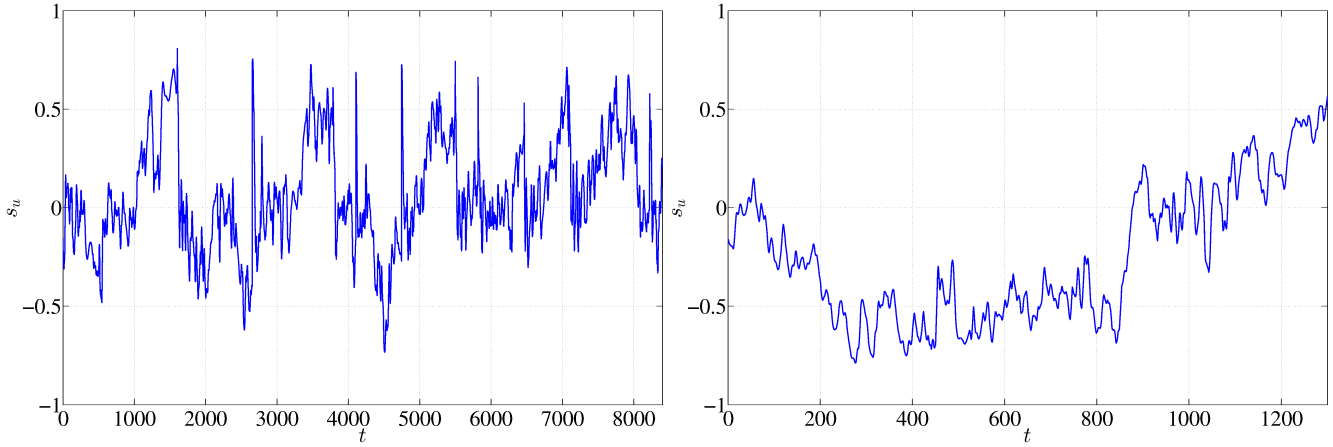

(a) $Re_\tau = 80$

(b) $Re_\tau = 120$

(c) $Re_\tau = 150$

(d) $Re_\tau = 180$

Figure 4.7: Time series of the asymmetry variable $s_u(t)$ for different Re_τ, $L_x^+ \times L_z^+ = 200 \times 100$.

and along both walls for shorter durations. Shown below in Fig. 4.8 is a switching event of the localised structures from the bottom wall to the top wall.

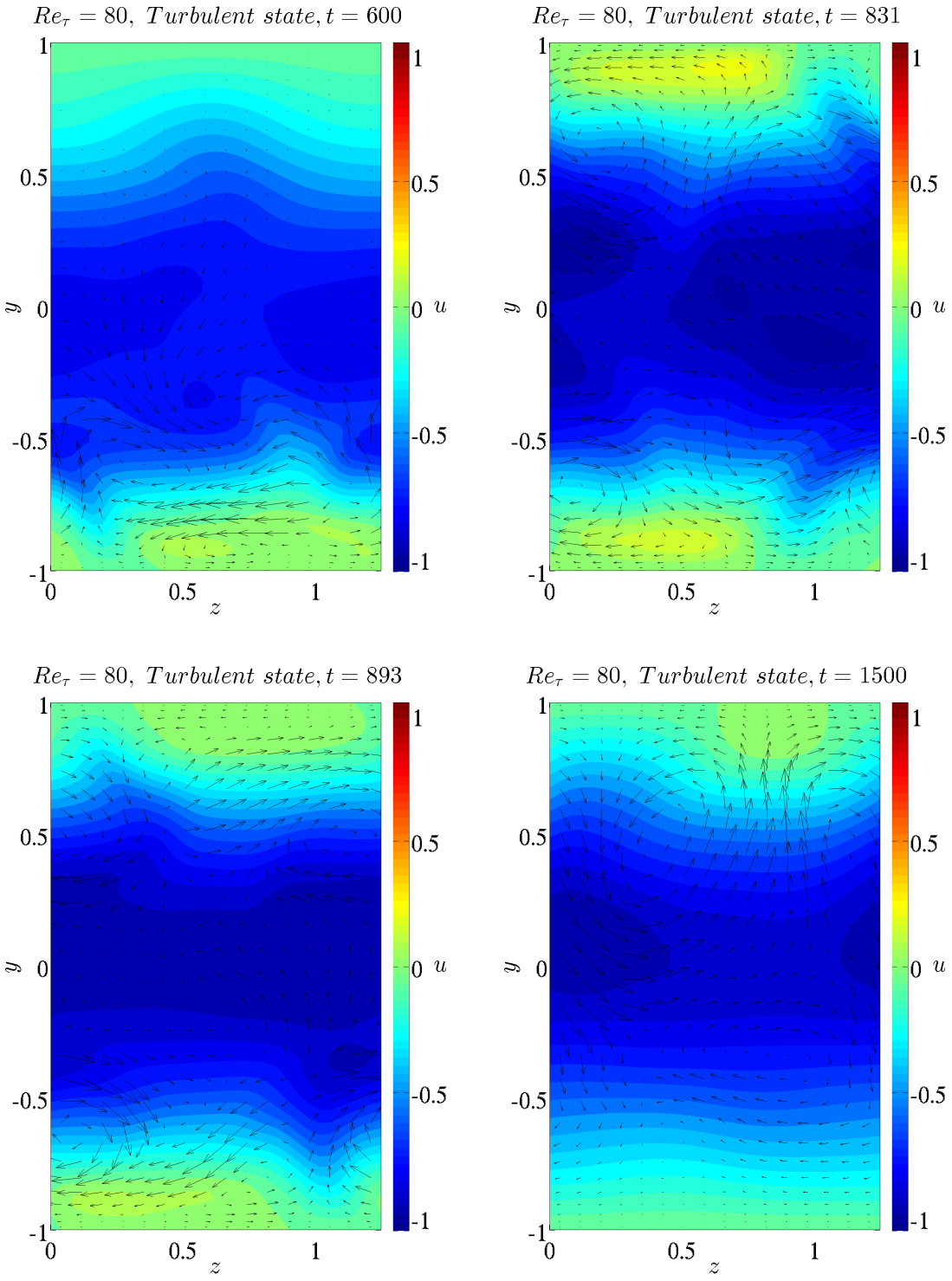

Figure 4.8: Visualisation of the reversals of the wall-localised structures in the turbulent flow at $Re_\tau = 80$

Fig. 4.8 shows the contours of streamwise velocity component u in the yz plane. When

the flow transitions from being localised at the bottom wall to the top wall, it also visits the $\boldsymbol{s} = \{s_u, s_v, s_w\} = 0$ subspace, where the flow is not localised necessarily at either wall, and the structures seem to be symmetric about the $y = 0$ plane.
A 3D representation of the streaks and vortical structures in the turbulent channel at $Re_\tau = 80$, close to $t = 1400$ is shown in Fig. 4.9.

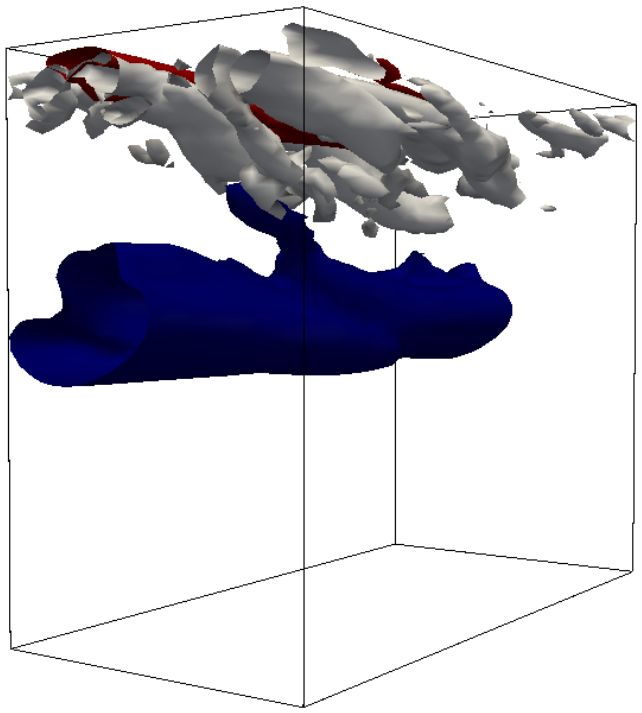

Figure 4.9: Streaks and vortical structures in a turbulent channel at $Re_\tau = 80$. The iso-surfaces have the following values : $u = +0.1$ representing the high speed streak in red, $u = -0.05$ representing the low speed streak in blue, $Q = 1.2$ representing the vortical structures.

However as Re_τ is increased to $Re_\tau = 150$ and $Re_\tau = 180$, the value of the asymmetry variable is quite far away from zero and close to ± 1 for long durations of time, indicating that the turbulent structures are single-walled but do not necessarily prefer the top or the bottom wall.
Similarly, the reversals of the near-wall structures in the channel at $Re_\tau = 180$ are shown in Fig. 4.10.

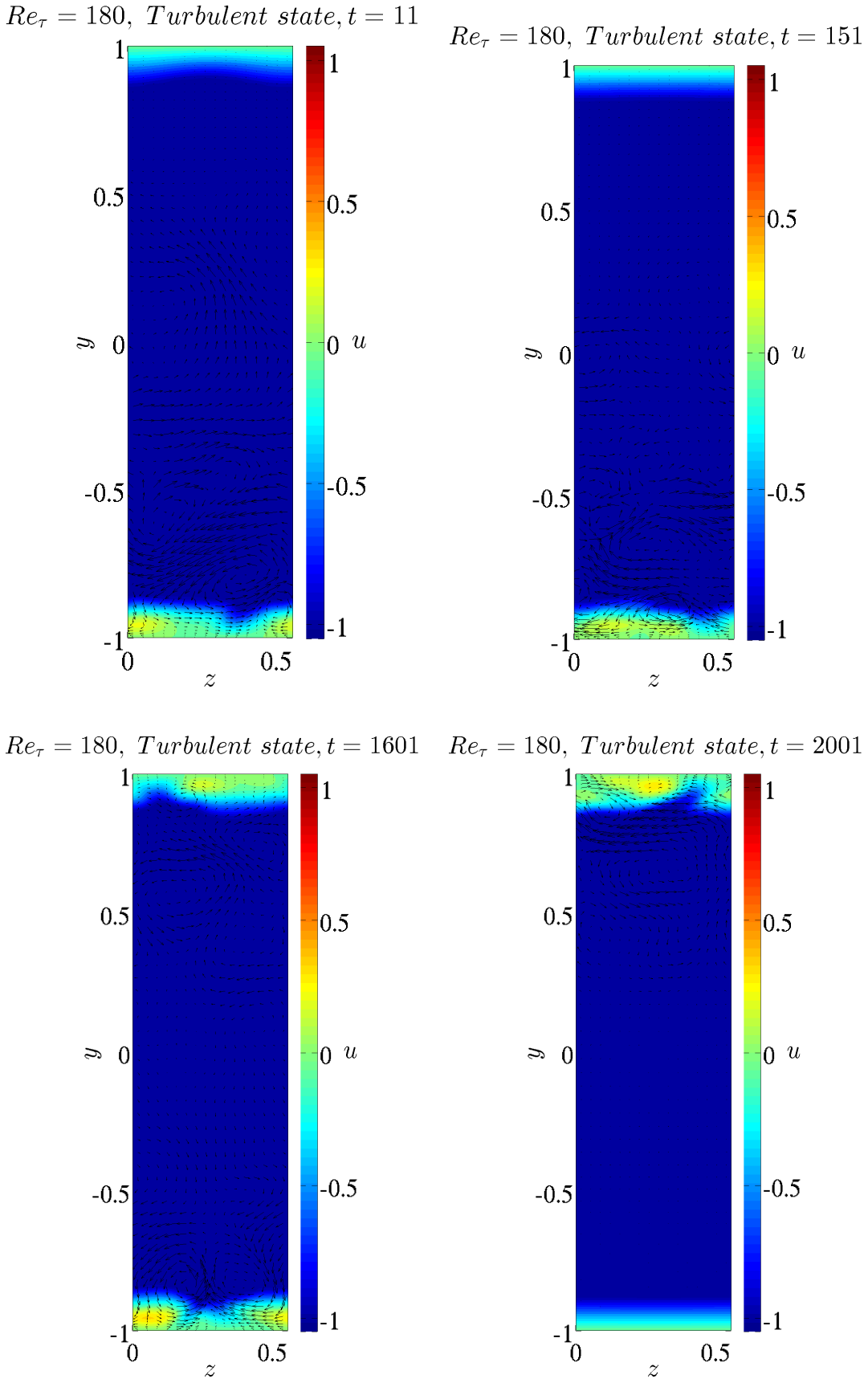

Figure 4.10: Visualisation of one reversal event in the turbulent flow at $Re_\tau = 180$

Similarly to the turbulent compositions of the large channel shown earlier, we compute the r.m.s. velocity profiles, $< u_{rms}(y) >$ for these turbulent simulations.
The r.m.s. velocity profiles of these computations in the M.F.U. channel for different Re_τ and plotted in Figs. 4.11 and 4.12.

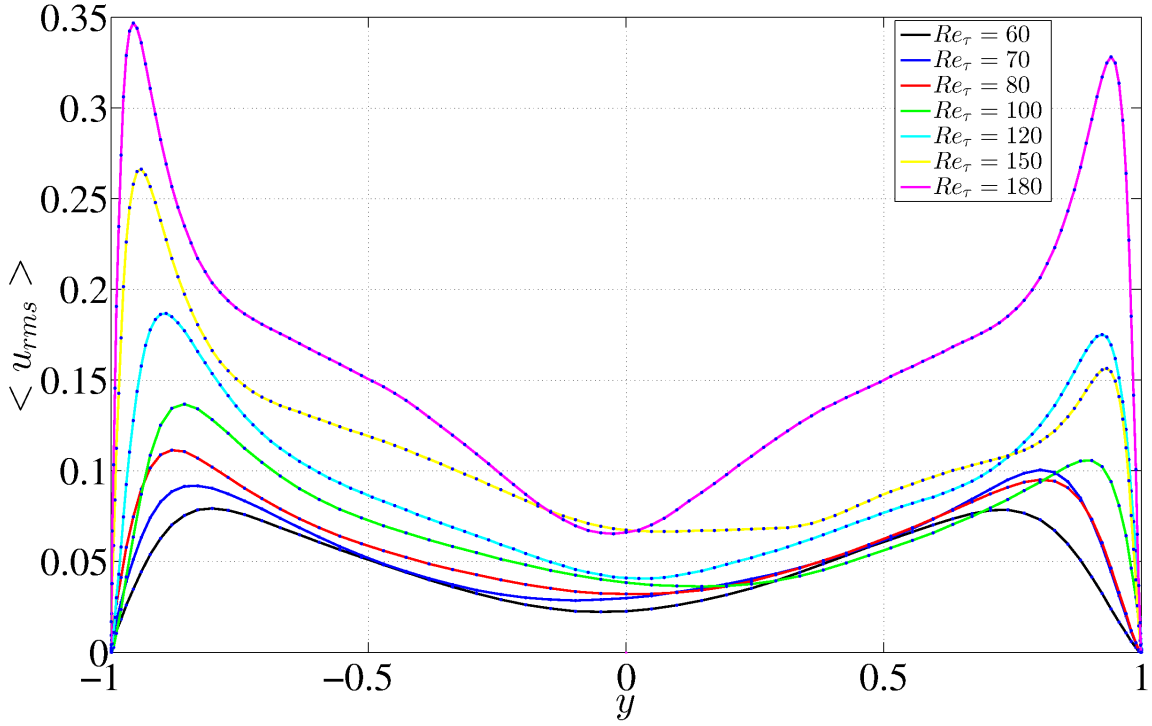

Figure 4.11: R.m.s. velocity profiles $< u_{rms}(y) >$ of the turbulent simulations at different Re_τ in a channel of dimensions $L_x^+ \times L_z^+ = 200 \times 100$, plotted in outer units

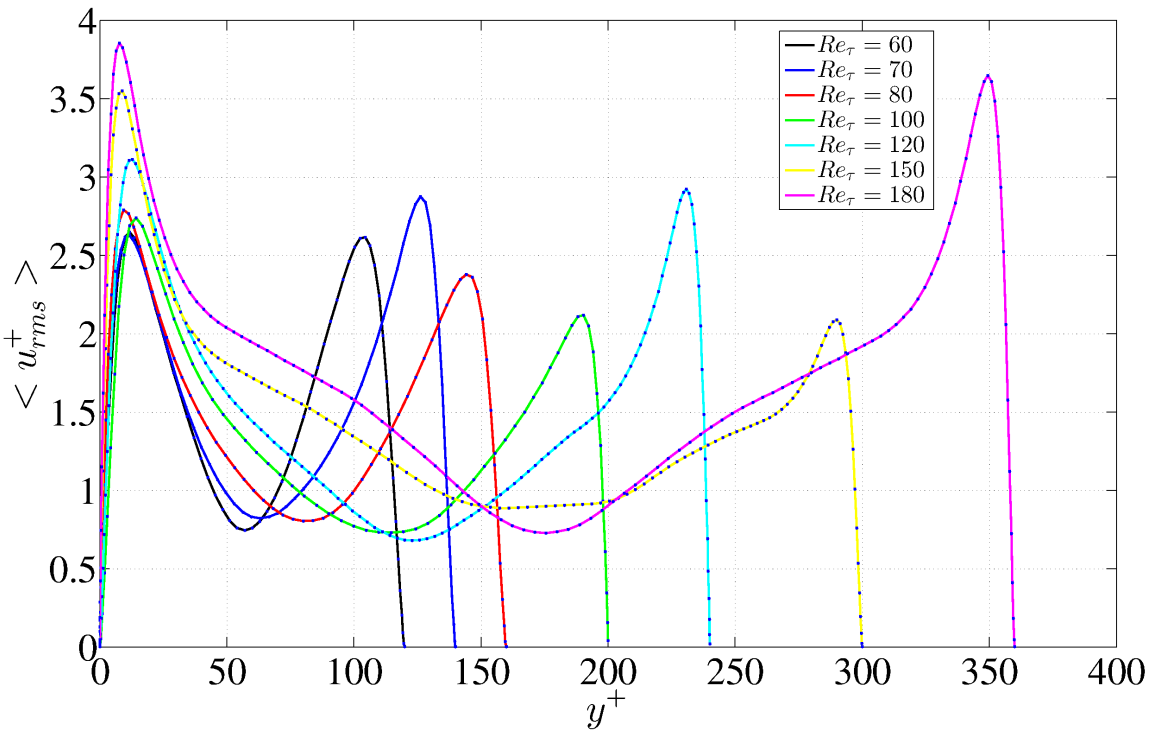

Figure 4.12: R.m.s. velocity profiles $< u^+_{rms}(y^+) >$ of the turbulent simulations at different Re_τ in a channel of dimensions $L^+_x \times L^+_z = 200 \times 100$, plotted in inner units

We see in Figs. 4.11 and 4.12 that the position of y_{max} remains fairly constant with changing values of Re_τ whereas the maximum values of the profiles u_{max} do not collapse to a single value. Unlike in section 4.1.2 where the turbulent solutions show perfect inner unit scaling, the r.m.s. profiles of the turbulent simulations do not show a perfect scaling in inner units 4.12. It is to be noted that the turbulent solutions in large channels have structures localised near both the walls while the turbulent solutions in the M.F.U. channel are localised near only one of the walls for long time-durations. The symmetric geometry of the M.F.U. implies that statistics for this case must be symmetric with respect to the $y = 0$ plane. However this is not the case as seen in Fig. 4.12. For instance, the curve in yellow which represents the $< u_{rms^+}(y^+) >$ profile for $Re_\tau = 150$ has a higher peak close to $y^+ = 0$ than at $y^+ = 300$. This suggests that, despite the long computational time used, the present statistics are not fully converged (in terms of number of reversals). We discuss this further in Chapter 6 where conditional averaging of statistics is introduced.

4.2.2 Lifetimes

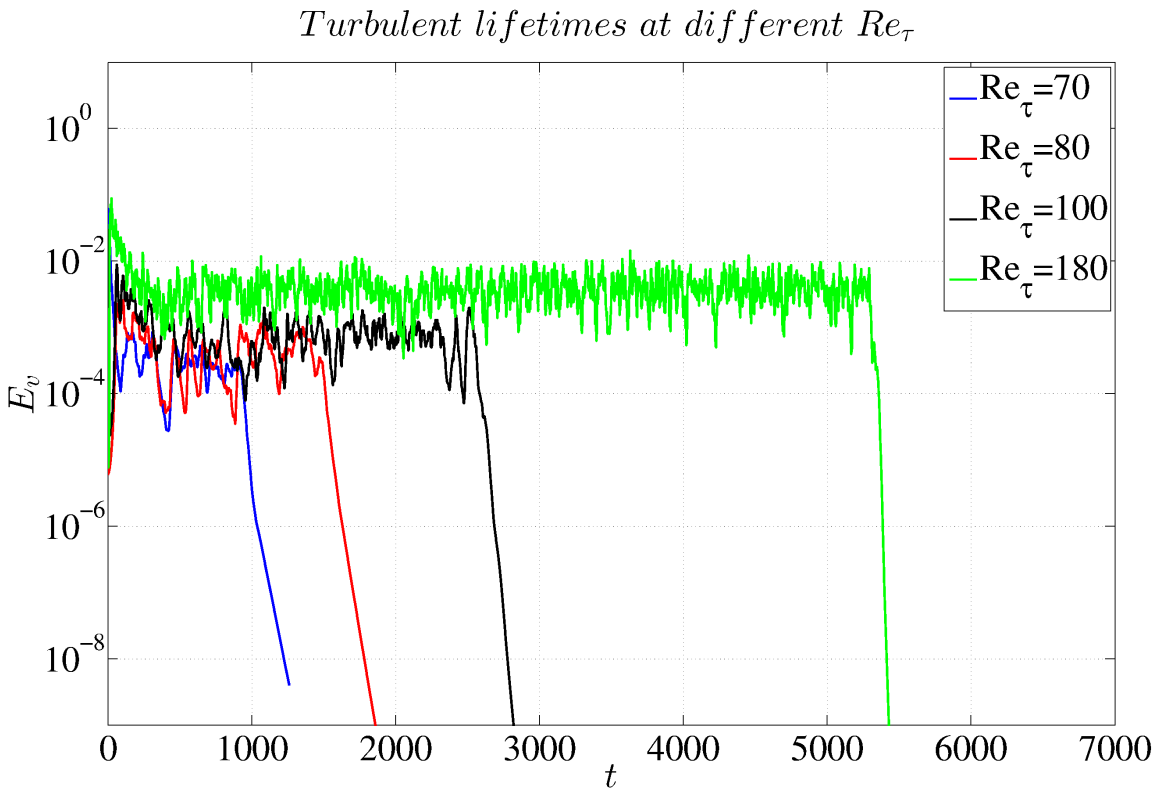

Figure 4.13: The plot showing the lifetimes of turbulence in channels with varying Re_τ

Fig. 4.13 shows the time duration for which turbulence sustains in the channel when initiated by a random flow field, for different Re_τ. It is to be noted that, for different Re_τ, the streamwise and the spanwise dimensions of the channels also change accordingly, since the inner dimensions of the channel are kept constant. As Re_τ increases, the time duration over which turbulence persists in the channel also increases. This is on expected lines, as we have sustained turbulence at Re_τ which is considerably high compared to the usual values of Re_τ at which relaminarisation occurs. But it is observed that turbulence doesn't sustain more than about $5500h/U_{cl}$ for all Re_τ, as opposed to the sustained turbulence found for equivalent Re in larger channels or in other shear flows, for instance turbulent pipe flow [82]. This is interpreted as a confinement effect by periodic boundary conditions due to the small value of L_x^+. This remark is valid only for the present simulations. If one considers different initial conditions, the relevant analysis should by statistical [82].

Chapter 5

Phase space analysis of the Minimal Flow Unit

5.1 Open Questions

In this chapter, we discuss the search for invariant solutions in the M.F.U. other than the laminar state. Such invariant solutions could be fixed points or periodic orbits which are embedded in the turbulent region of the state space. We also intend to see whether we can find the manifolds connecting the different solutions so that they could give us an insight into some of the interesting dynamics taking place on the path of transition to turbulence. A clear inspiration is the work done by Gibson *et al.* [14] in finding different solutions of plane Couette flow, both on the lower branch and the upper branch and finding interesting dynamics by mapping the heteroclinic connections between the steady solutions.

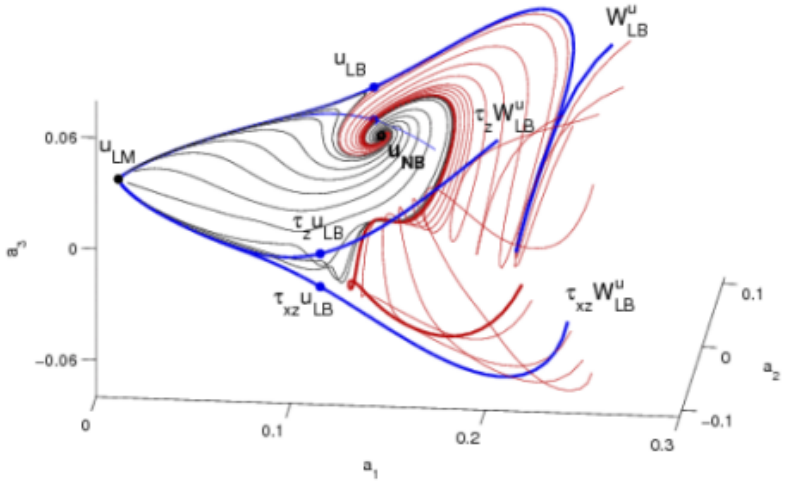

Figure 5.1: A state space projection of the different solutions of pCf and their unstable manifolds, taken from Gibson *et al.* [14]

5.2 Edge states

Edge states have been introduced earlier in section 1.7.3. Edge states have been computed in plane Couette flow [50], [51], pipe flow [56], [53], boundary layer flows [57], [83], and in plane Poiseuille flow [45]. Computations of exact coherent states in shear flows often starts with edge computations as seen, for instance, in [9], [84] and [13]. We use the procedure outlined in section 3.4 to compute edge states from $Re_\tau = 60$ to $Re_\tau = 180$ and discuss their properties in this chapter. We also outline another procedure to look for exact solutions like periodic orbits and travelling waves using recurrence maps, and discuss the properties of the travelling wave thus obtained.

5.2.1 Analysis of energy signals

We first start with the search for edge states using bisection. In this section, we show time series of the cross-flow energy component $E_v(t)$ obtained using bisection at different Re_τ. The domain size for all the computations in this section is $L_x^+ \times L_z^+ = 200 \times 100$. The domain size in outer units varies depending on Re_τ and is mentioned in the respective figure captions.

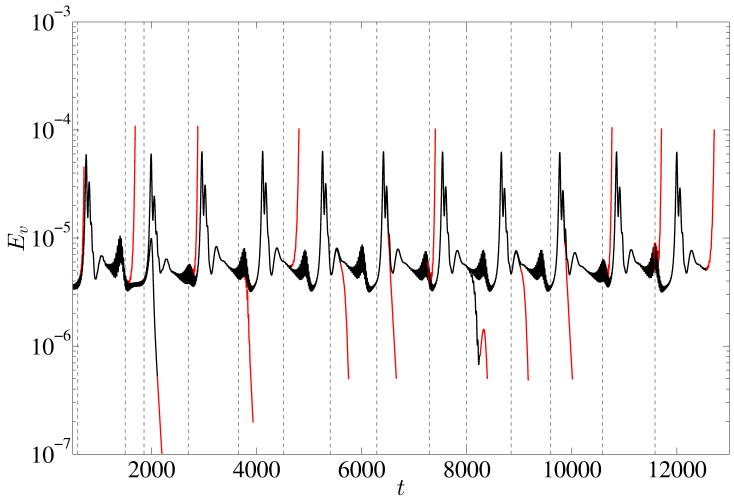

Figure 5.2: Energy of the cross-flow component E_v vs t, $Re_\tau = 60$, $L_x \times L_z = 3.33 \times 1.67$.

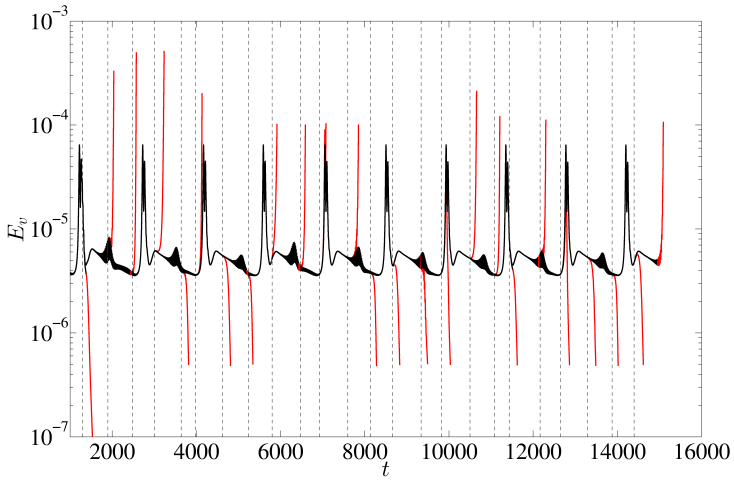

Figure 5.3: Energy of the cross-flow component E_v vs t, $Re_\tau = 70$, $L_x \times L_z = 2.86 \times 1.43$.

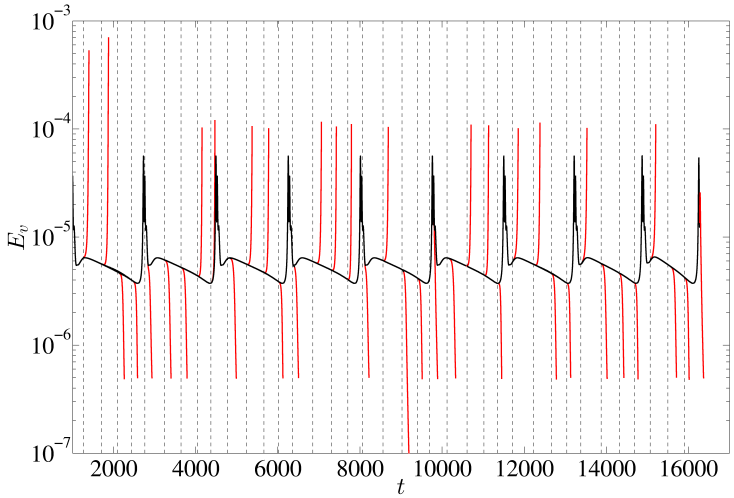

Figure 5.4: Energy of the cross-flow component E_v vs t, $Re_\tau = 80$, $L_x \times L_z = 2.5 \times 1.25$.

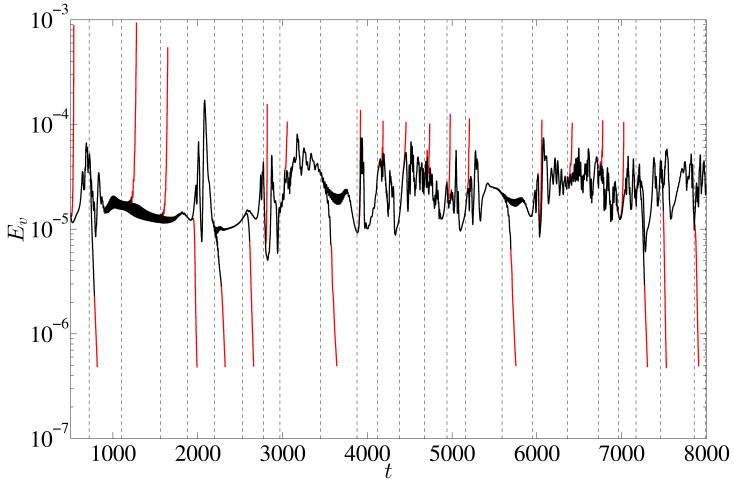

Figure 5.5: Energy of the cross-flow component E_v vs t, $Re_\tau = 100$, $L_x \times L_z = 2.0 \times 1.0$.

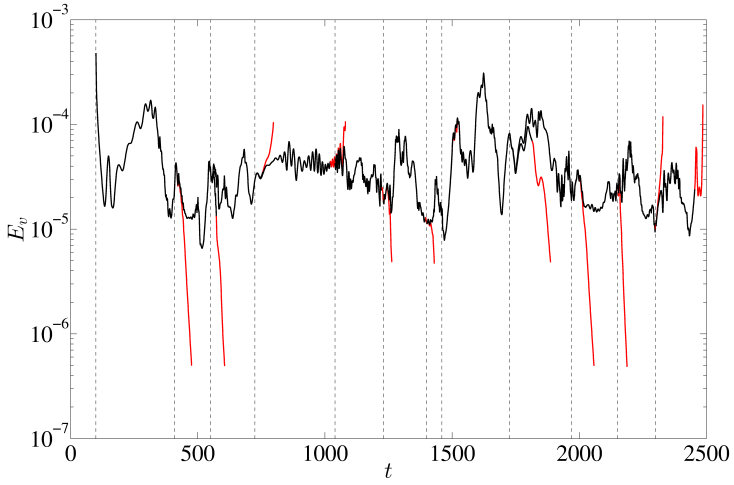

Figure 5.6: Energy of the cross-flow component E_v vs t, $Re_\tau = 120$, $L_x \times L_z = 1.67 \times 0.83$.

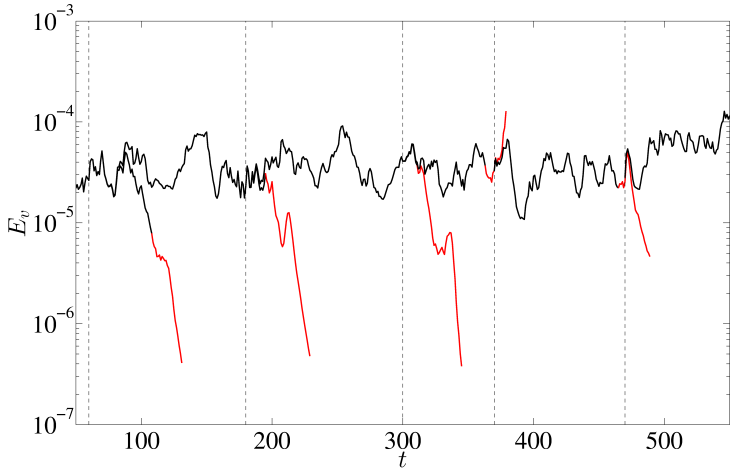

Figure 5.7: Energy of the cross-flow component E_v vs t, $Re_\tau = 180$, $L_x \times L_z = 1.11 \times 0.56$.

Figs. 5.2 to 5.7 show the energy of the cross-flow component E_v as time series for different Re_τ. Time is measured in times of U_{cl}/h. The trajectory in black represents the edge state. The trajectories in red represent the flows which deviate from the edge to either become turbulent (red trajectories deviating towards the top of the figures) or become laminar (red trajectories deviating towards the bottom of the figures). After few initial trial runs, thresholds for E_v were set at 10^{-4} and 5×10^{-7} to determine whether the flow becomes turbulent or laminar, respectively. The turbulent threshold is much higher than 10^{-4} for $Re_\tau \geq 100$. The black dotted lines in the figures correspond to the times at which a new bisection was initialised after the former computation has reached machine precision.

From Figs. 5.2, 5.3 and 5.4, the energy shows periodicity for $Re_\tau \leq 80$. The energy trajectory for $Re_\tau = 60$ seems to have a period consisting of three peaks which corresponds to around 4100 time units. A similar 3-periodic edge state has been observed in boundary-layer flow in [85]. Specifically, for $Re_\tau = 80$, the energy signal $E_v(t)$ has a period of around 1700 time units, with the presence of a burst associated with a sudden peaking of the

energy, together with a calm phase over one period. The first such bursting state has been observed by Toh and Itano in channel flow [55]. Subsequently such bursting edge states have been observed in boundary-layer flow [85] [83] and in plane Poiseuille flow driven by a fixed mass flux [84]. However to our knowledge, these are the first edge state computations performed in the original M.F.U. domains with dimensions set in inner units.
It is observed that for $Re_\tau \geq 100$, the energy varies in a chaotic way. Chaotic edge states have been observed earlier in plane Couette flow [51] and in pipe flow [86].

5.2.2 Connections between the time series and the corresponding physical space structures

5.2.2.1 Edge state at $Re_\tau = 80$

The yz plane representation of the edge state for $Re_\tau = 80$ at four different time instants is shown in the Fig. 5.8, with the streamwise velocity of the perturbations represented using iso-contours and the spanwise and wall-normal velocities of the perturbations represented using vectors. The regions in yellow represent zones of positive streamwise velocity and the regions in blue represent zones of negative streamwise velocity as indicated in the colorbars adjacent to the snapshots.

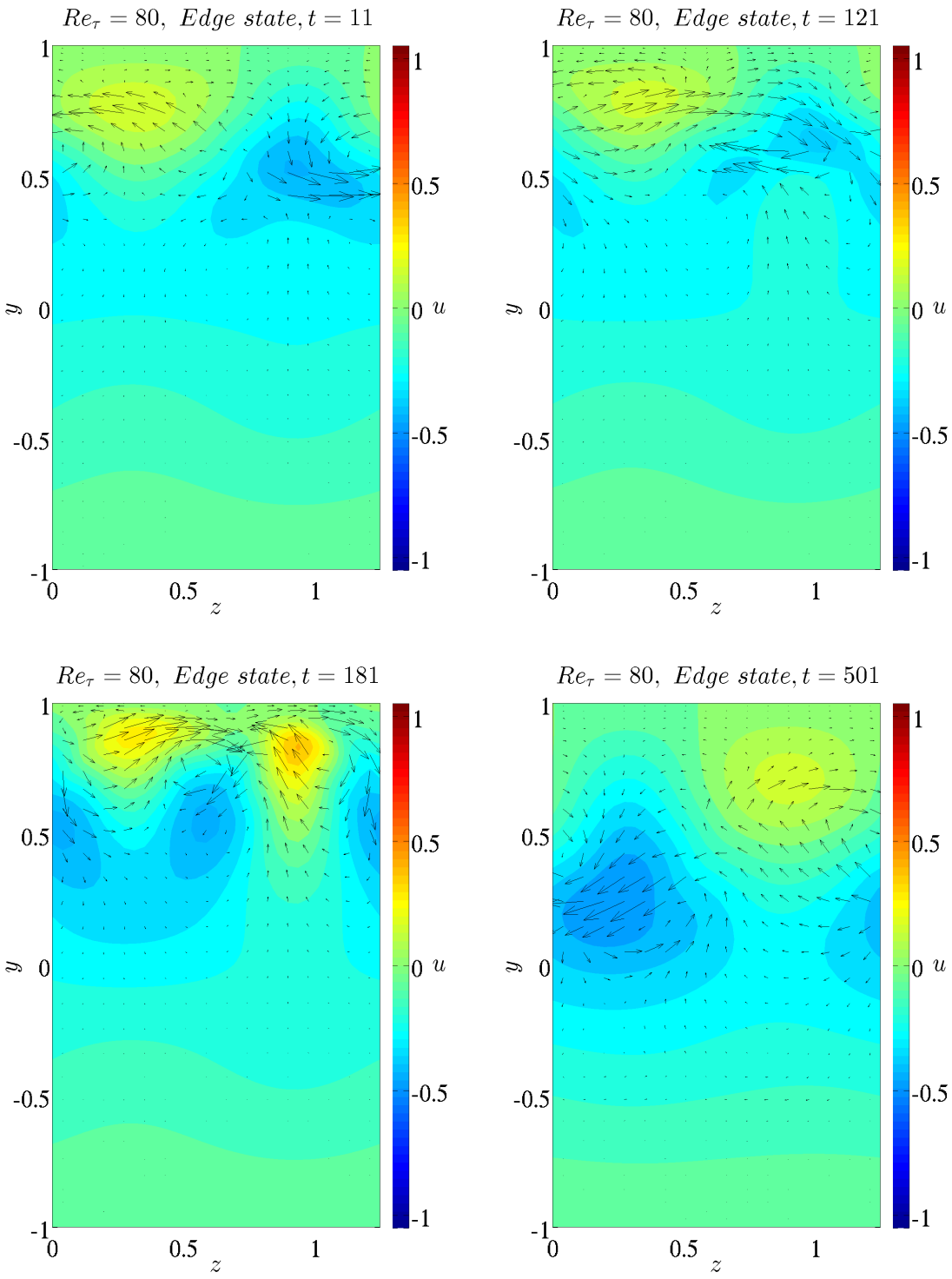

Figure 5.8: The edge state, $Re_\tau = 80$, $L_x^+ \times L_z^+ = 200 \times 100$

We observe the presence of counter-rotating vortices, along with a pair of streaks localised near the top wall. The high-speed streak is in yellow and the low-speed streak in blue, as indicated by the colorbar. The high-speed and low-speed streaks do not maintain the same spanwise position throughout the period of the edge state. The streaks undergo a shift in their spanwise location once every period. This is seen clearly in the sequence of

snapshots shown over one cycle of the edge state, with the high-speed streak closer to the spanwise location $z = 0$ at time $t = 11$, but at time $t = 501$ being closer to $z = L_z/2$. The snapshot at time $t = 181$ features breakdown of the streaks at their respective locations, eventually leading to the formation of the new streaks.
It is noted that the physical process of shifting of the streaks occurs immediately after the bursting phase in the energy trajectory of this edge state observed in Fig. 5.4.
The edge state shown here follows the self sustaining process as explained by Fabian Waleffe [8], and as also observed previously in studies by Toh and Itano in channel flow [49] [55], Zammert *et al.* [44] in plane Poiseuille flow. The edge state shown here also undergoes a shift in the spanwise direction every cycle as observed earlier also by Khapko *et al.* and Kreilos *et al.* in ASBL [83] [59].

5.2.2.2 Edge state at $Re_\tau = 120$

The yz representation of the edge state for $Re_\tau = 120$ is shown in Fig. 5.9, with the contours and the vectors having the same significance as earlier.

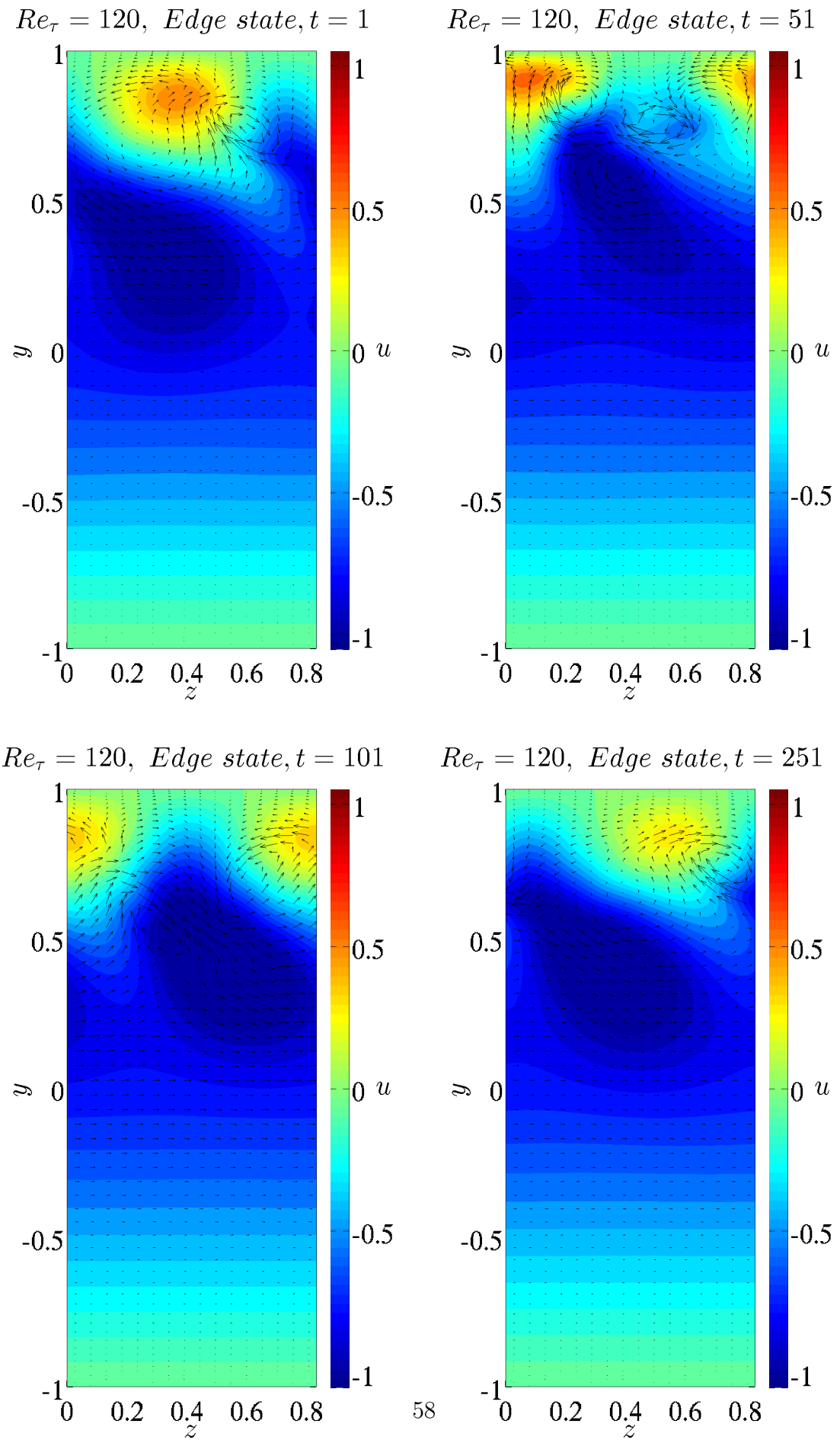

Figure 5.9: The edge state, $Re_\tau = 120$, $L_x^+ \times L_z^+ = 200 \times 100$

The edge state at $Re_\tau = 120$ seems to be chaotic (refer Fig. 5.6). However despite different dynamics, the physical structure of this edge state is qualitatively similar to the structure observed in the edge state at $Re_\tau = 80$. Fig. 5.9 shows the snapshots of contours of u in the yz plane.

5.2.2.3 Shifts, Reversal at $Re_\tau = 100$

We observe that most of the edge states are one-sided, and the streaks remain confined to one wall all the time. However for one particular case, $Re_\tau = 100$, we observed a phenomenon of 'switching' : the streaks which are localised near the top wall disintegrate, eventually regenerate and localise near the bottom wall, as in the turbulent regime. Fig. 5.10 shows the flow visualisations at four different time instants during the process of switching. Here the yz plane is shown, contours represent u, and the cross flow velocity is represented through vectors.

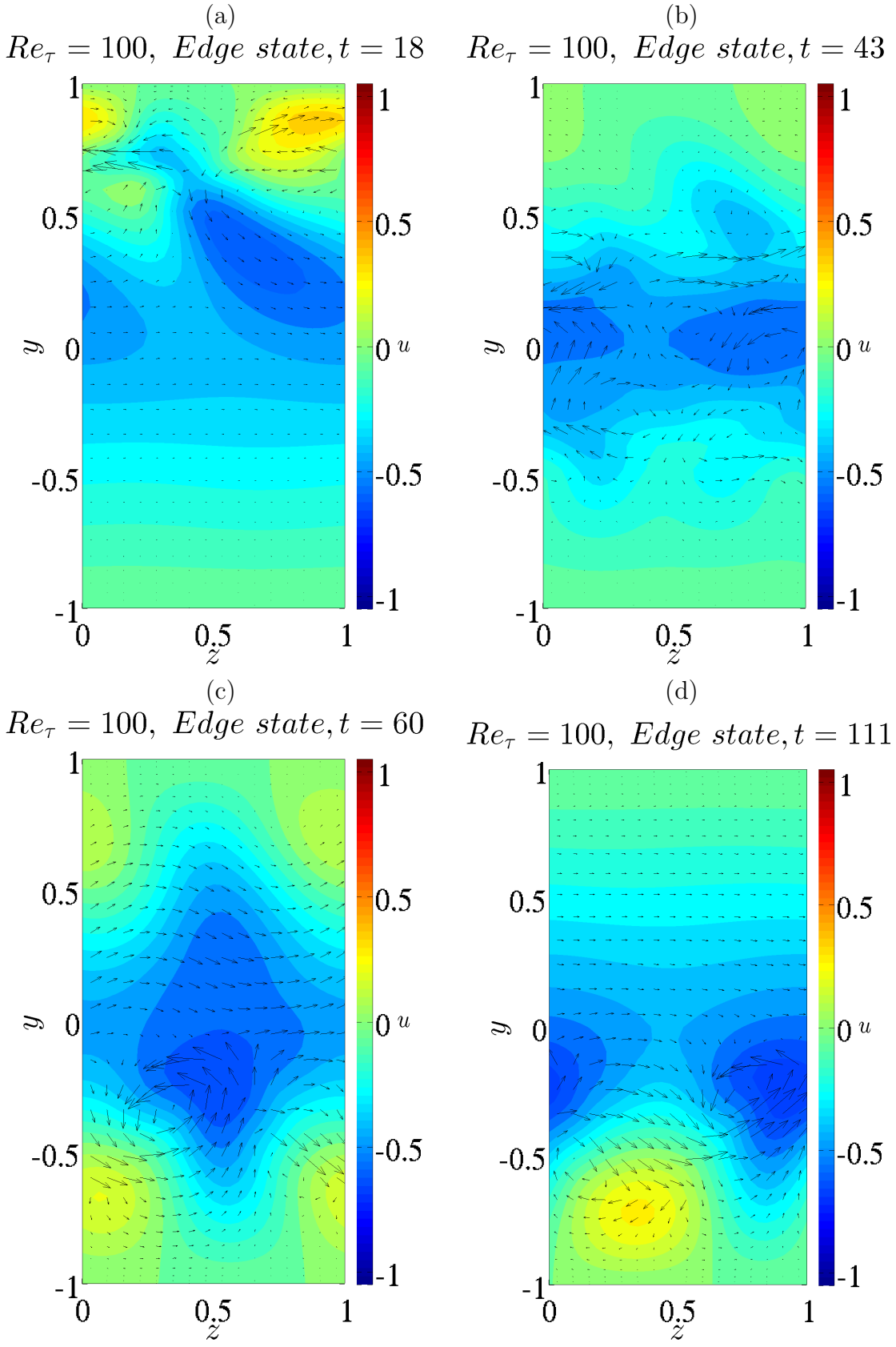

Figure 5.10: Switching of the edge state, $Re_\tau = 100$, $L_x^+ \times L_z^+ = 200 \times 100$

The edge state contains a set of high-speed and low-speed streaks which are initially

confined to the top wall as seen in Fig. 5.10(a). At some point of time, the streaks near the top wall begin to disintegrate as shown in Fig. 5.10(b). At the same time, streaks begin to appear near the bottom wall, and for a short time duration, there are streaks at both walls, for instance, close to $t = 60$ in Fig. 5.10(c). The structure at this time instant looks to be nearly symmetric about the $y = 0$ plane, and the state space dynamics features a visit through the $\boldsymbol{s} = \{s_u, s_v, s_w\} = 0$ subspace. This is similar to what is observed in the reversals in turbulent simulations in M.F.U. (refer Fig. 4.8 in section 4.2) where the flow visits the $\boldsymbol{s} = \{s_u, s_v, s_w\} = 0$ subspace when switching from top-wall localised turbulence to bottom-wall localised turbulence. Eventually, in the edge state at $Re_\tau = 100$ the streaks at the top wall fully decay, while the streaks at the bottom wall fully develop as seen in Fig. 5.10(d). The flow field in Fig. 5.10(d) has completely switched compared to the initial flow field in Fig. 5.10(a).

5.3 State space representations

Apart from the laminar solution, two different equilibrium regimes in plane Poiseuille flow have been computed in earlier sections : the turbulent solutions and the edge states. These flow regimes have at least one similarity - the visualisation in physical space shows the presence of near-wall streaks and streamwise vortices. Naturally the question arises how close the two regimes are in state space and how the two regimes are connected. We aim at constructing state space representations and phase portraits containing the already-identified flow regimes such that they could provide insight into the dynamics that can guide further analysis.

5.3.1 State space projections

A clear inspiration for this is the work by Gibson *et al.* [14]. They developed state space representations containing their solutions in plane Couette flow using basis sets constructed from exact solutions of the Navier-Stokes equations. Since the flow in consideration for this thesis, plane Poiseuille flow, is also a wall-bounded shear flow in a similar geometry, and our simulations have been done in periodic domains similar to [14], we project our edge state in a phase space constructed similar to the one described in [14]. Firstly, a basis is constructed using one full flow field from the flow, $\boldsymbol{u_{bas}}$ and its translations τ along the x and z directions. The vectors $\boldsymbol{a_1}$, $\boldsymbol{a_2}$, $\boldsymbol{a_3}$ and $\boldsymbol{a_4}$ defined in Eqns. 5.1 to 5.4 are the basis vectors onto which all the fields are projected. τ_x and τ_z are translations by $L_x/2$ and $L_z/2$ in the x and z directions, respectively. $\tau_{xz} = \tau_x\tau_z$ is the translation by $L_x/2$ in the x-direction and $L_z/2$ in the z-direction.

$$\boldsymbol{a_1} = (1 + \tau_x + \tau_z + \tau_{xz})\boldsymbol{u_{bas}} \tag{5.1}$$

$$\boldsymbol{a_2} = (1 + \tau_x - \tau_z - \tau_{xz})\boldsymbol{u_{bas}} \tag{5.2}$$

$$\boldsymbol{a_3} = (1 - \tau_x + \tau_z - \tau_{xz})\boldsymbol{u_{bas}} \tag{5.3}$$

$$\boldsymbol{a_4} = (1 - \tau_x - \tau_z + \tau_{xz})\boldsymbol{u_{bas}} \tag{5.4}$$

$$\tau_x[u, v, w](x, y, z) = [u, v, w](x + L_x/2, y, z) \tag{5.5}$$

$$\tau_z[u, v, w](x, y, z) = [u, v, w](x, y, z + L_z/2) \tag{5.6}$$

$$\tau_{xz}[u, v, w](x, y, z) = [u, v, w](x + L_x/2, y, z + L_z/2) \tag{5.7}$$

Fig. 5.11 shows the projection of the original edge trajectory onto this basis and the trajectory obtained after quotienting out the symmetries, for a time duration slightly greater than the apparent period of the edge state.

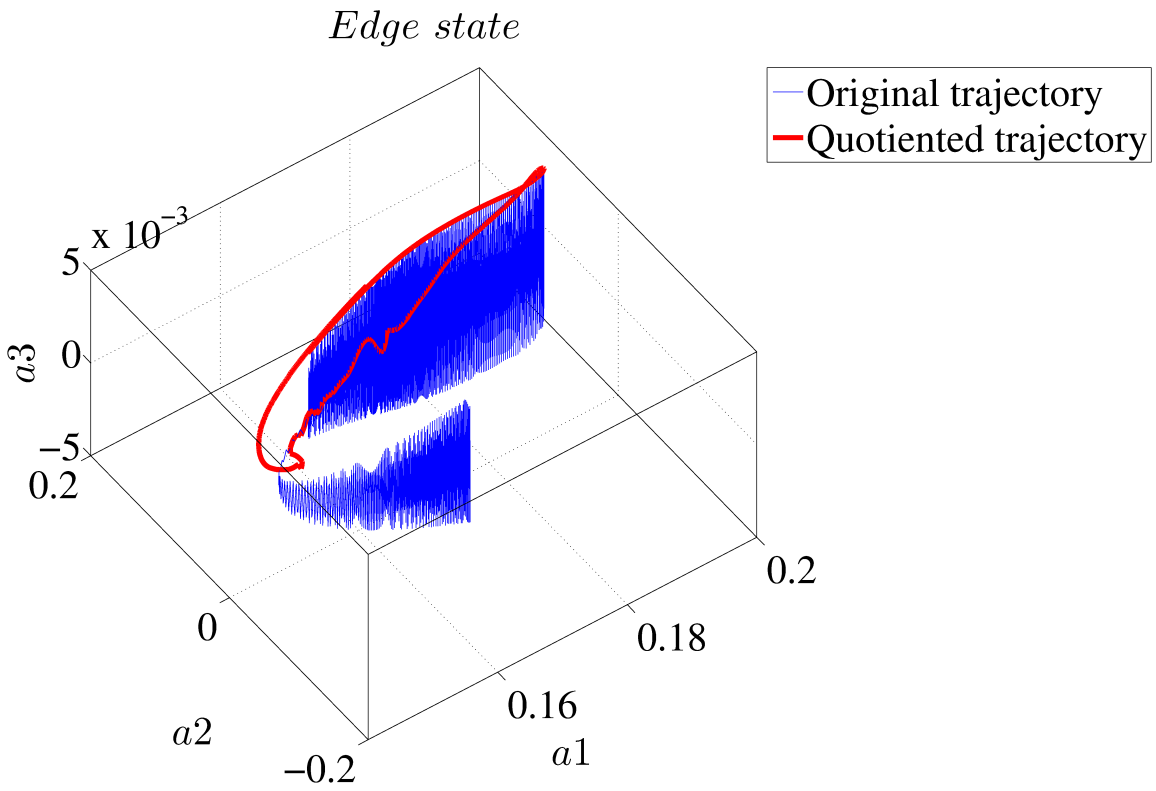

Figure 5.11: State space projection of the original and the quotiented trajectory of the edge state obtained at $Re_\tau = 80$ on a basis constructed using one of the flow fields from the flow $\boldsymbol{u_{bas}}$ and its translations along the x and z directions; blue corresponds to the original trajectory and red to the quotiented trajectory

The trajectory in blue represents the original trajectory of the edge state in this state space. After a time duration equal to the period of the edge state, it is seen that this trajectory does not close onto itself. This confirms again that the edge state is indeed a relative periodic orbit even though the energy signal of this orbit 5.4 seems periodic. The trajectory in red represents the trajectory of the edge state whose symmetries have been quotiented out. As expected this trajectory does not experience any shift like the original trajectory in blue. Even the quotiented trajectory does not perfectly close onto

itself since the edge state has been obtained only through bisection, and has not been converged to an exact solution. The R.P.O. has a large period of around 1700 units which makes it unfeasible to be used in a Newton solver to converge to the exact solution [9].

5.3.2 Phase portraits

It was seen in sections 4.2 and 5.2.2 that both the turbulent states and the edge states in the M.F.U. domain have wall-localised structures and also feature switches from one wall to the other. A better choice for a projection basis would allow one to quantify the nearness of the structures to either wall. A good choice would be the asymmetry variables s_u, s_v and s_w defined in 4.1.2. The phase portrait of the edge state at $Re_\tau = 80$ constructed using the asymmetry variables, s_u, s_v and s_w is shown in Fig. 5.12.

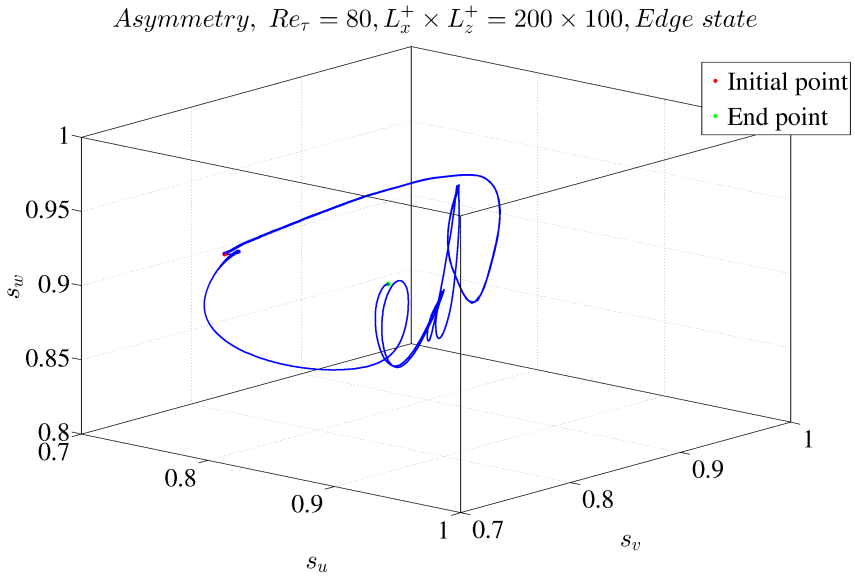

Figure 5.12: Phase portrait of the edge trajectory obtained at $Re_\tau = 80$ using asymmetry variables s_u, s_v, s_w

Note that s_u, s_v and s_w are insensitive to shifts, i.e. $\forall \boldsymbol{u}, \forall \sigma, s_u(\boldsymbol{u}) = s_u(\sigma \boldsymbol{u})$. Thus quotienting is not needed for such phase portraits.
The asymmetry values of the edge state is confined to values between 0.7 and 1 along all three directions, indicating that the edge state has streaks confined to the top wall. However we know that, by symmetry, there exists a symmetric edge state solution about the mid-y plane, that is, there exists a solution whose values of asymmetry variable would be the opposite to the above mentioned values, confined within -0.7 and -1 for all s_u, s_v and s_w.
We plot the phase portrait of these edge states, and the turbulent trajectories using these asymmetry variables in Figs. 5.13, 5.14 and 5.15.

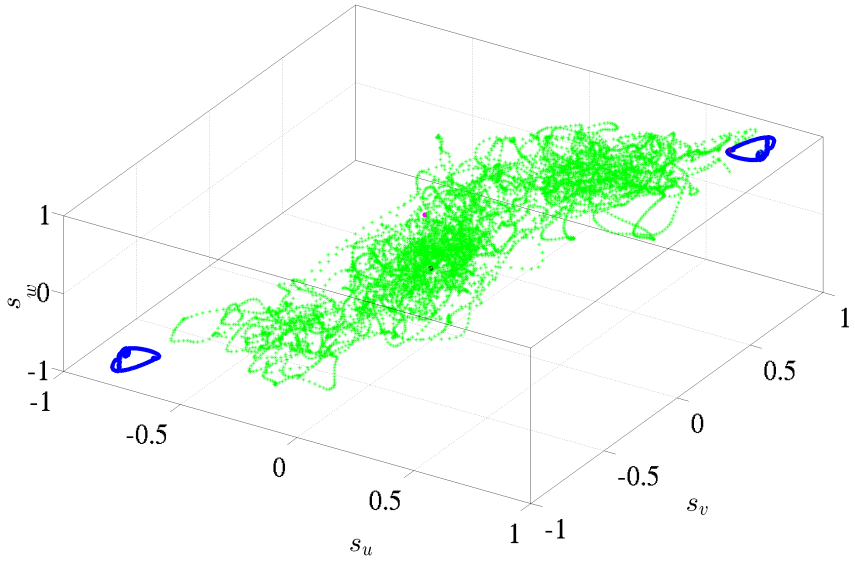

Figure 5.13: Representation of two symmetric copies of the edge and the turbulent trajectory on a basis constructed using the asymmetry variables, $Re_\tau = 80$, edge state in blue and the turbulent trajectory in green

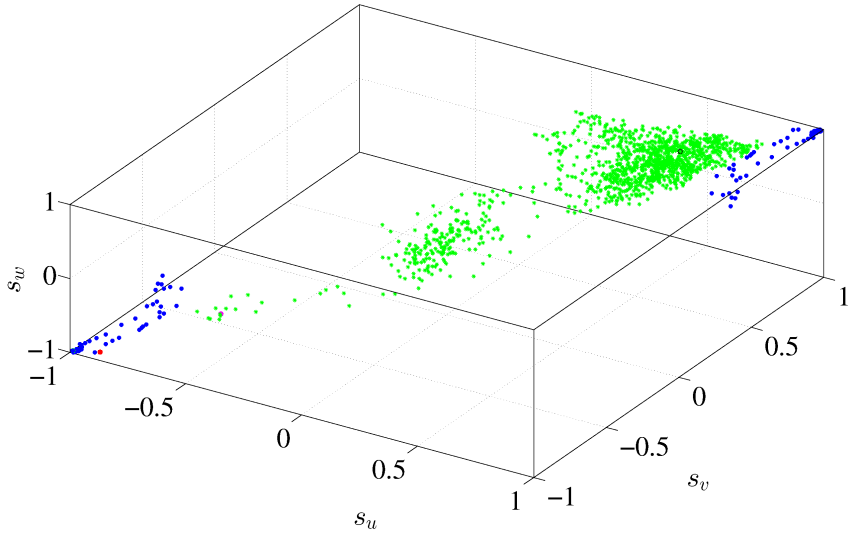

Figure 5.14: Same as Fig. 5.13, $Re_\tau = 150$

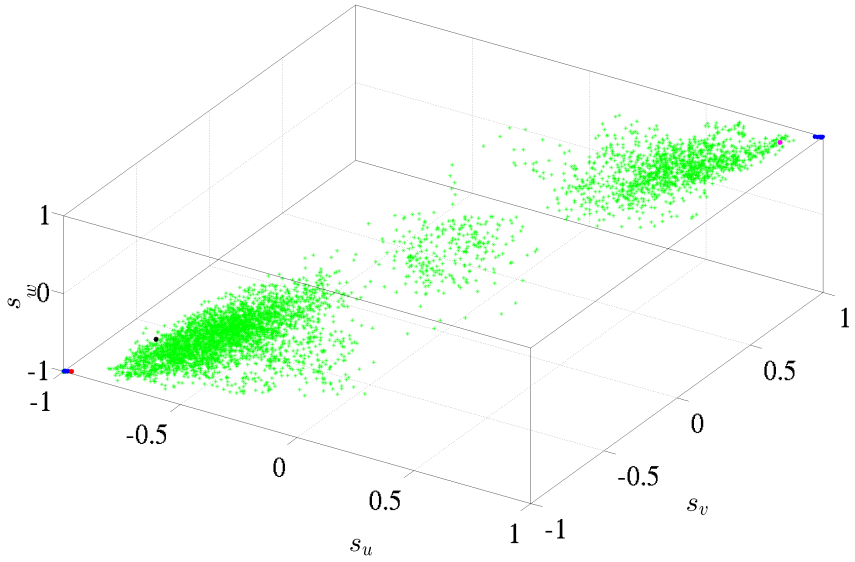

Figure 5.15: Same as Fig. 5.13, $Re_\tau = 180$

The symmetric counterpart of the edge state in the asymmetry subspace in Fig. 5.13 is representative of the fact that the streaks in our edge state could have localised as well on the lower wall, this choice being completely arbitrary. The turbulent trajectory makes several close visits to the edge state. It is also clear from Fig. 5.13 that the symmetric subspace $\boldsymbol{s} = s_u = s_v = s_w = 0$ is visited quite often for all Re_τ which is an indication that there could be repelling exact solutions in this space. The search for such solutions, is explained in the subsequent sections.

5.4 Recurrences

We look for exact coherent states in the M.F.U. system. In Chapter 1, we introduced mathematical objects like steady states, periodic orbits and their generalisations. We would now like to identify the presence of such objects in phase space. These objects have the common property that they correspond to non-trivial zeros of

$$r(t,T) = ||v(t+T) - v(t)||_a \ , T > 0 \tag{5.8}$$

i.e. they correspond to exact recurrence motion. 'a' represents the weight assigned to the cross flow components while computing the norm [32]. Hence a suitable approach to find these objects would be to construct recurrence maps as defined in Eqn. 5.8. The norm is defined as

$$||u||_a^2 = \frac{1}{2}\int_0^{L_x}\int_{-1}^{1}\int_0^{L_z}(u^2 + a^2(v^2+w^2))dxdydz. \tag{5.9}$$

The flow fields $v(t+T)$ and $v(t)$ in Eqn. 5.8 have been obtained after suitable quotienting as explained in section 3.5. This is important as the process of quotienting removes the continuous symmetries (which corresponds to invariance in the x and z directions) in the system. Thus the possibility that the recurrence map finds zeros of Eqn. 5.8 between two flow fields $v(t+T)$ and $v(t)$ which just differ by a translation either in the x or z direction,

is negated. Some of the recurrence maps obtained for turbulent simulations at $Re_\tau = 80$ have been shown in Figs. 5.16, 5.17 and 5.18.

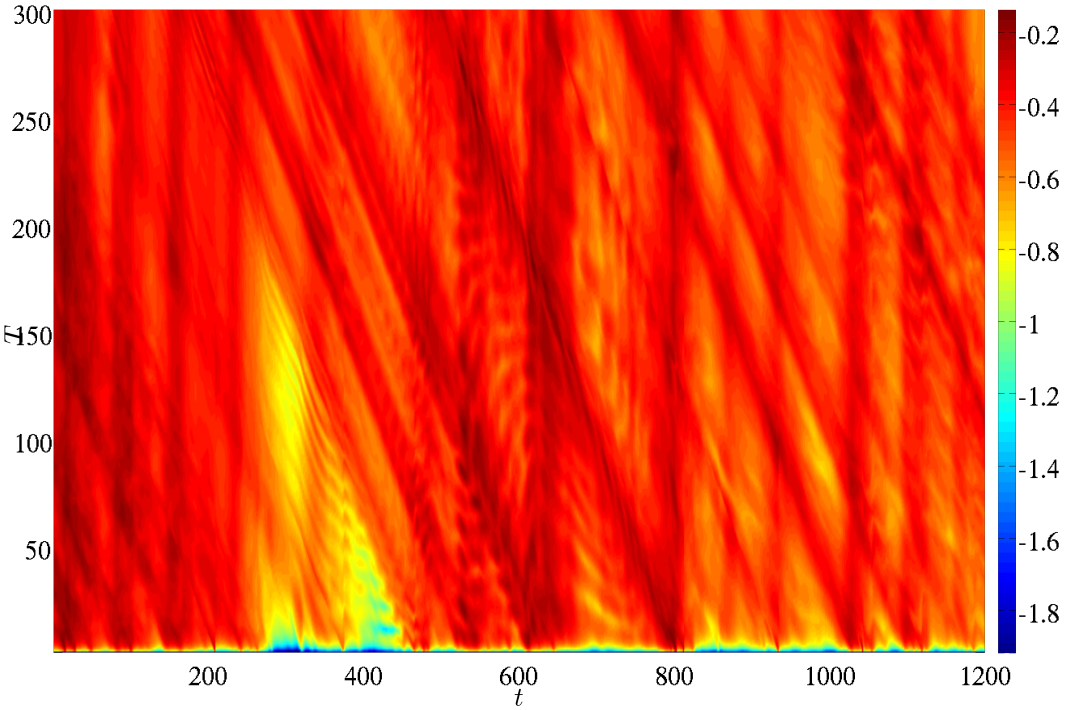

Figure 5.16: Recurrence map, case 1

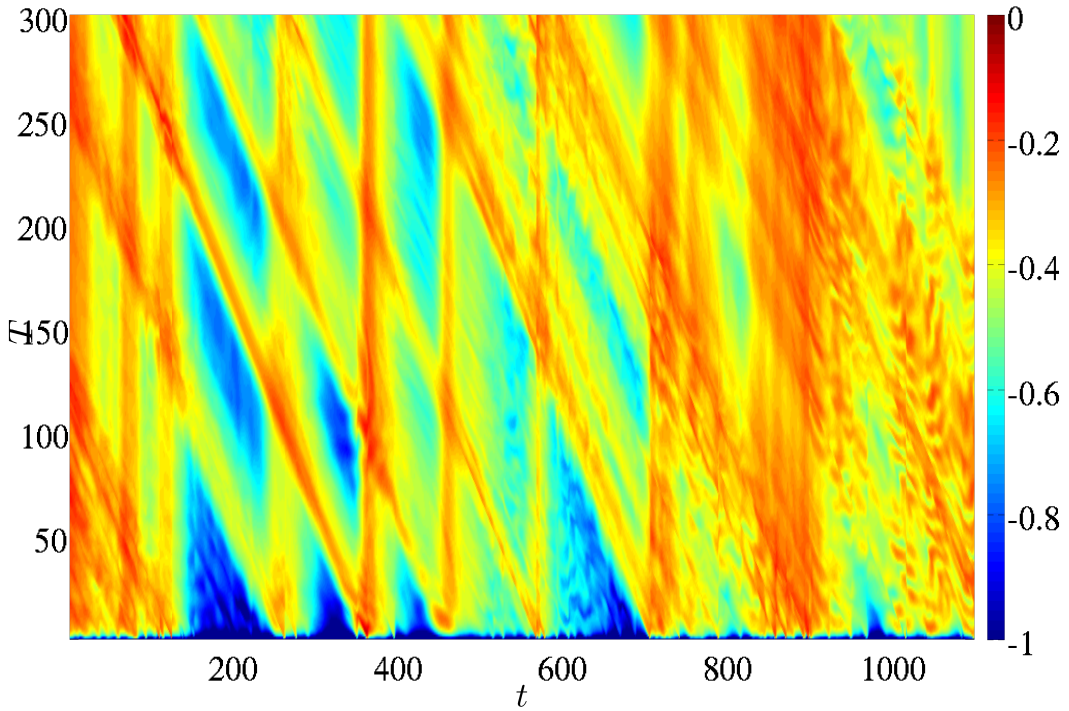

Figure 5.17: Recurrence map, case 2

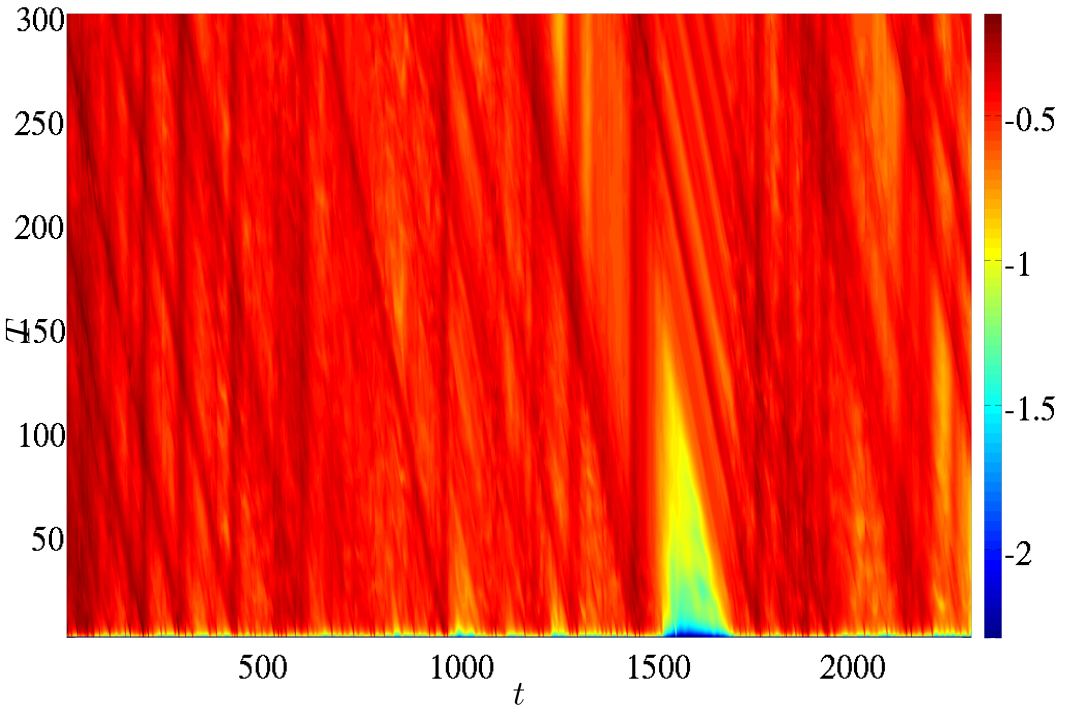

Figure 5.18: Recurrence map, case 3

Low values of $r(t, T)$ for small T indicate the presence of unstable steady states of the quotiented system, whereas horizontal lines with low $r(t, T)$ for $T > 0$ suggest unstable periodic orbits. The recurrence maps seemingly do not feature horizontal lines as seen in Fig 10 in [32]. This suggests that either no relative periodic orbit is to be found, or that the method is not well adapted. We also observe discontinuities in the recurrence maps very close to $T = 0$.
On the other hand, the quantity, $r(t, 1) = ||v(t + 1) - v(t)||_a$ was also plotted, where $r(t, 1)$ represents the $L - 2$ distance between a quotiented field at time t, $v(t + 1)$ and the quotiented field at the next time instant, $v(t + 1)$. This quantity helps us identify if there are any fixed points in our system. Indeed, we know that when the flow approaches a fixed point, the distance between consecutive flow fields reduces sharply, until the flow again deviates from the fixed point. The $r(t, 1) = ||v(t + 1) - v(t)||_a$ plots for the same turbulent simulations as in Figs. 5.16, 5.17 and 5.18 are shown below.

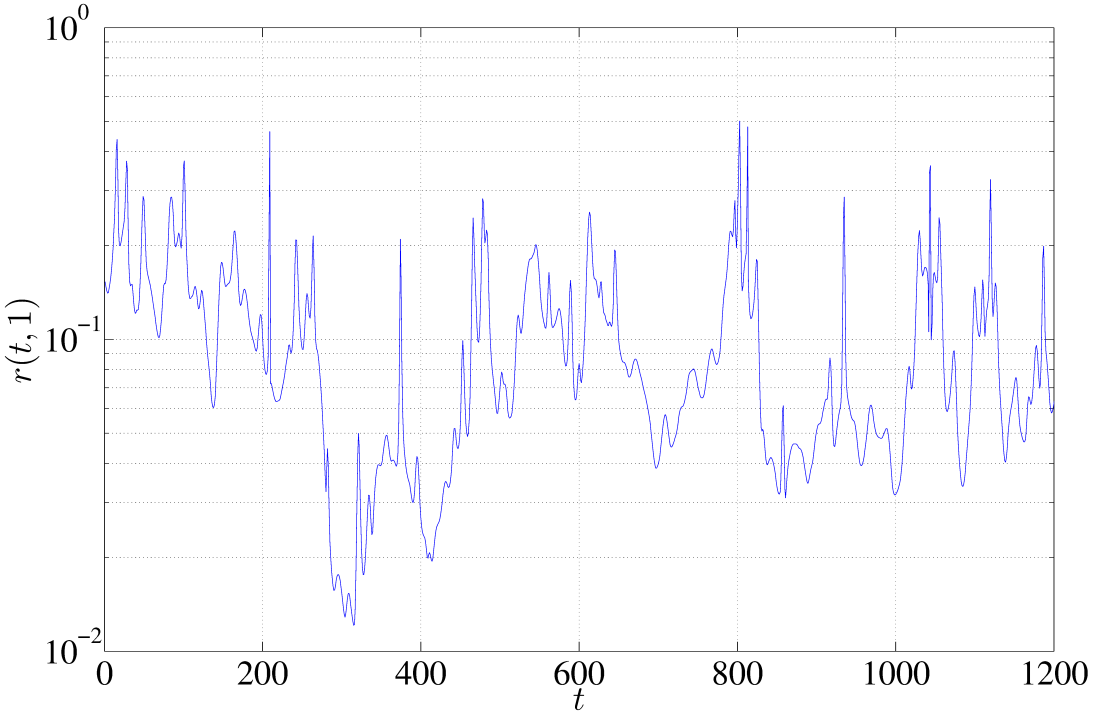

Figure 5.19: Plot of r(t,1), case 1

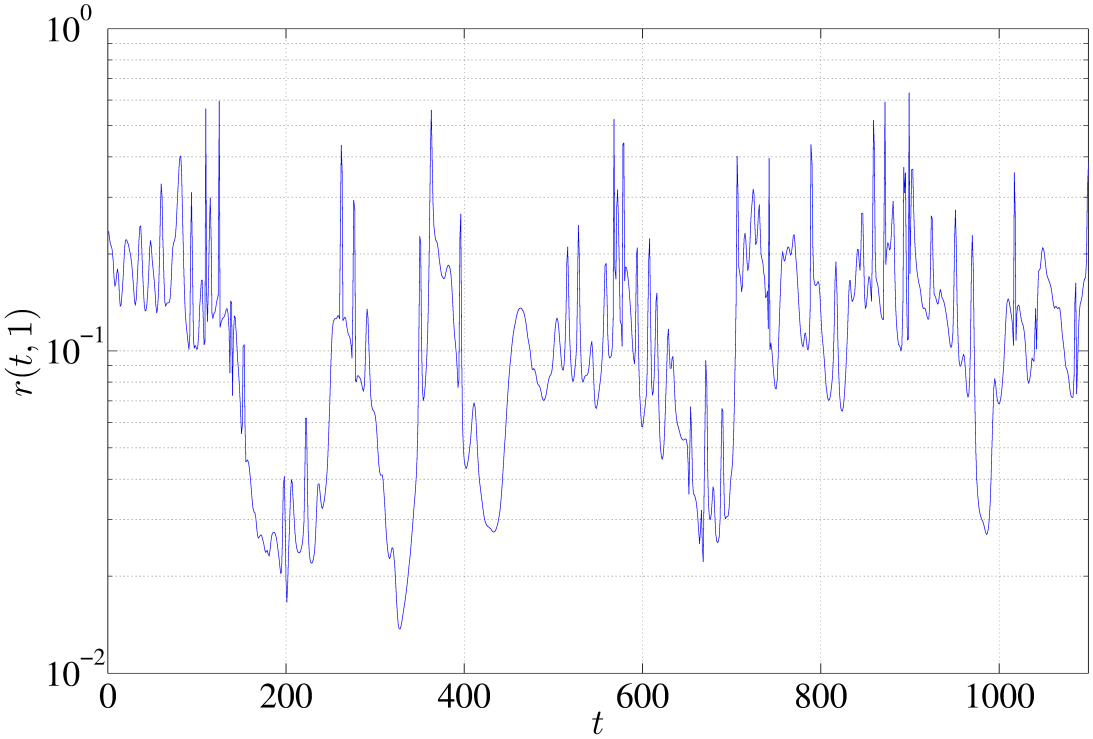

Figure 5.20: Plot of r(t,1), case 2

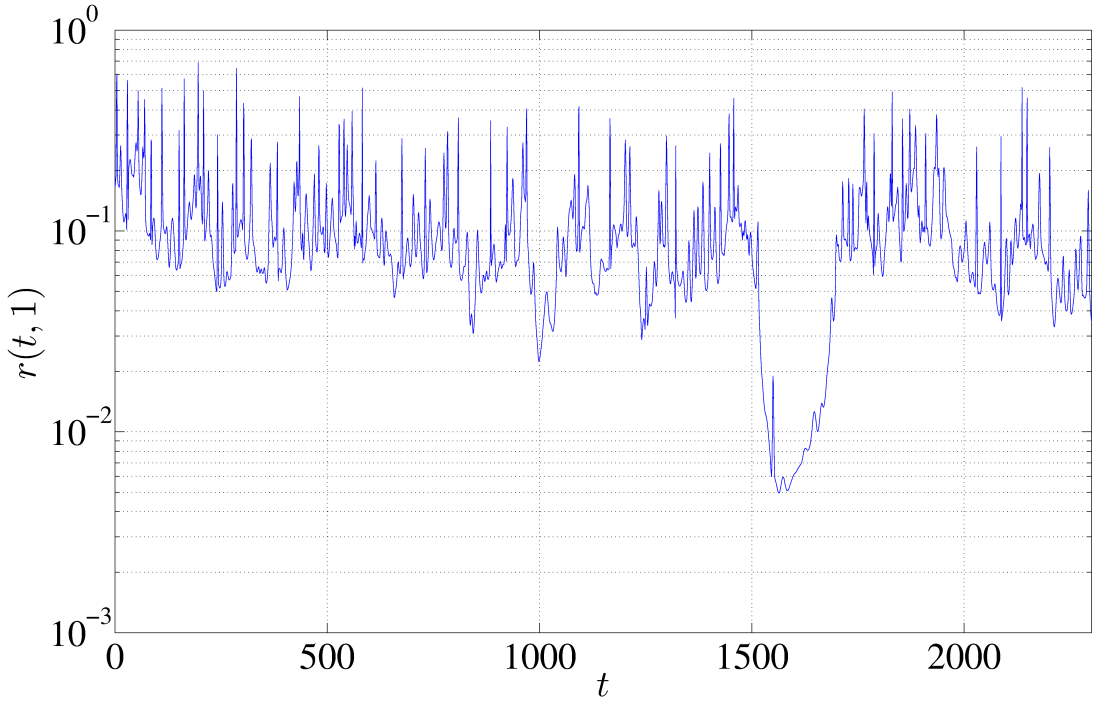

Figure 5.21: Plot of r(t,1), case 3

5.5 Identification of a travelling wave

We observe in Fig. 5.21 a sharp decrease of $r(t,1)$ at time $t \sim 1564$. As explained earlier, the sharp decrease in the L-2 distance between two consecutive flow fields suggests that the flow is approaching an unstable fixed point. Hence we look for an equilibrium-solution, using a Newton solver with the flow field at time $t = 1564$ being the initial guess. Since the values of $r(t,1)$ plotted in Fig. 5.21 correspond to the quotiented system, the fixed point in this system corresponds to a travelling wave in the original system. Different searches were performed with different guesses for the time period of the orbit, varying from $T_{guess} = 1$, to $T_{guess} = 4$ and $T_{guess} = 20$. The initial shift of the solution was also input, based on the value of the σ_x and σ_z obtained through the quotienting.
The search converged to the exact solution when the value of the time-period of the orbit was $T_{guess} = 20$. The convergence of the Newton search for this case is shown in Fig. 5.22.

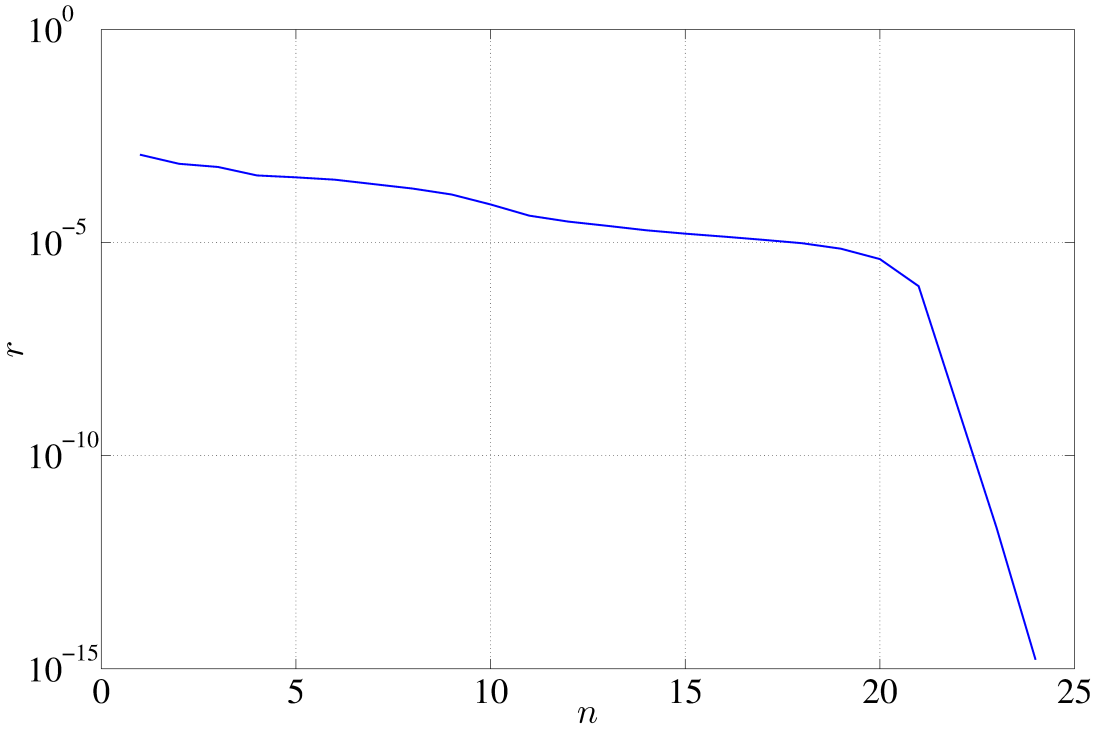

Figure 5.22: Plot of residual r vs number of iterations n performed by the Newton solver during convergence to the TW

This suggests that the quotienting method using a continously-changing template might not be completely accurate to look for a periodic orbit, nevertheless it was successful at identifying a travelling wave as explained above.

5.5.1 Properties of the TW : Does it lie on the edge?

The travelling wave has a three-dimensional structure, a phase-velocity $c = 0.295u_{cl}$ and no propagation in z. As far as we know, this solution has not been identified in the literature before. A stability analysis of the travelling wave was performed to find the most unstable modes using the Arnoldi algorithm (see section 3.3) implemented within *Channelflow* and with an observation time $T = 20$. The eigenspectrum is plotted in Fig. 5.23.

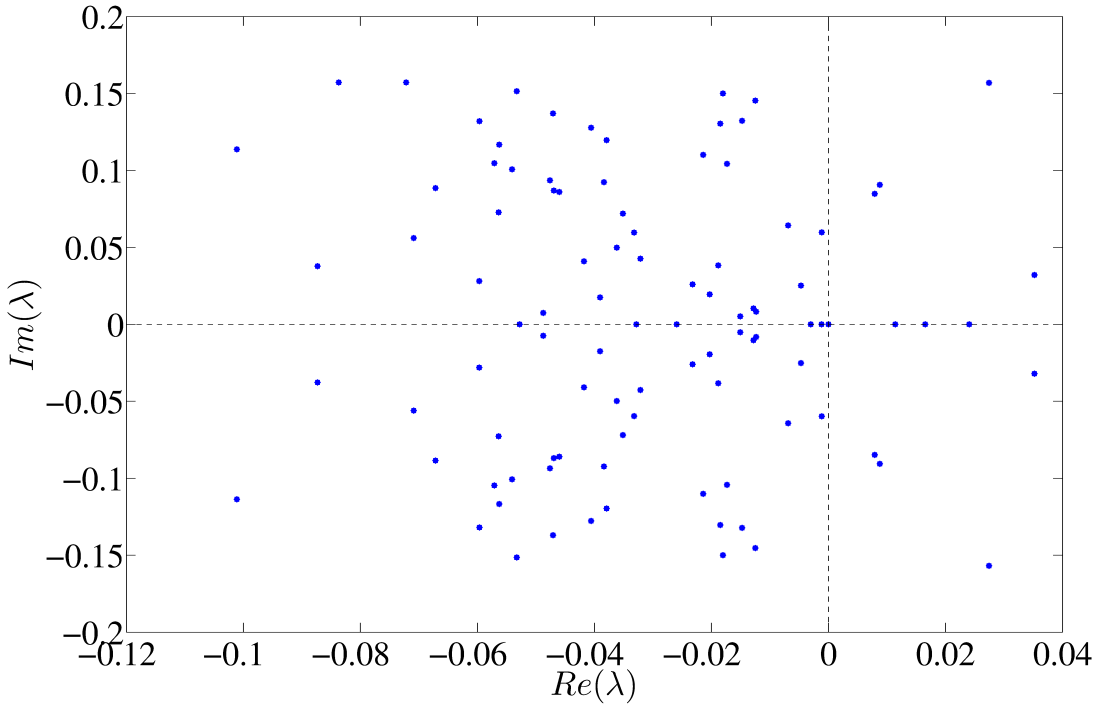

Figure 5.23: Eigenspectrum of the travelling wave

In Fig. 5.23, $Im(\lambda)$, the imaginary part of the eigenvalue λ represents the frequency. $Re(\lambda)$, the real part of λ represents the rate of instability, thus $Re(\lambda) > 0$ represents unstable eigenmodes. As anticipated, the TW possesses a small number of unstable eigenvalues : 11 unstable eigenvalues, including 3 real and 4 pairs of complex conjugate eigenvalues. We know that if an edge state is perturbed along its unstable eigenvector in opposite directions, the flow goes turbulent in one case, and laminar in another case. To check whether the travelling wave solution lies on the edge, the travelling wave solution was perturbed along each one of the corresponding unstable eigenvectors, in the two opposite directions. The energy time series are shown below in Fig. 5.24.

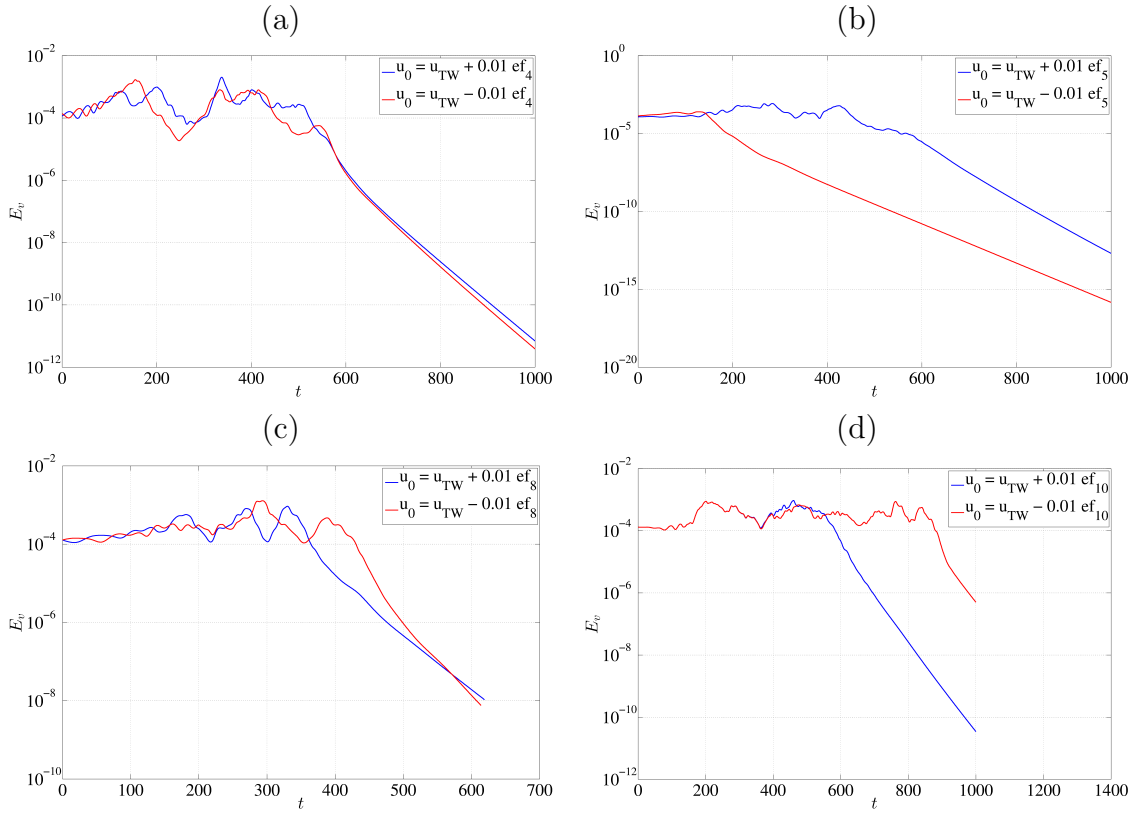

Figure 5.24: E_v *vs* t, TW perturbed along eigenvectors ef_4 in (a), ef_5 in (b), ef_8 in (c) and ef_{10} in (d)

It is observed that, for every such perturbation, the flow first becomes turbulent for a few hundred time units (typically between 200 and 600 time units) and eventually relaminarises. This rules out the possibility that the travelling wave solution might lie on the edge. This shows that the solution is not embedded in a more complicated edge state either, at least when no discrete symmetry is imposed as is the case here. In fact, since all perturbations lead to turbulent flow, there is a possibility that the travelling wave solution is an upper branch solution. A proper continuation of this TW in parameter space could shed light on this question possibly.

5.5.2 Spatial structure, symmetries

A 3D representation of the travelling wave is shown in Fig. 5.25.

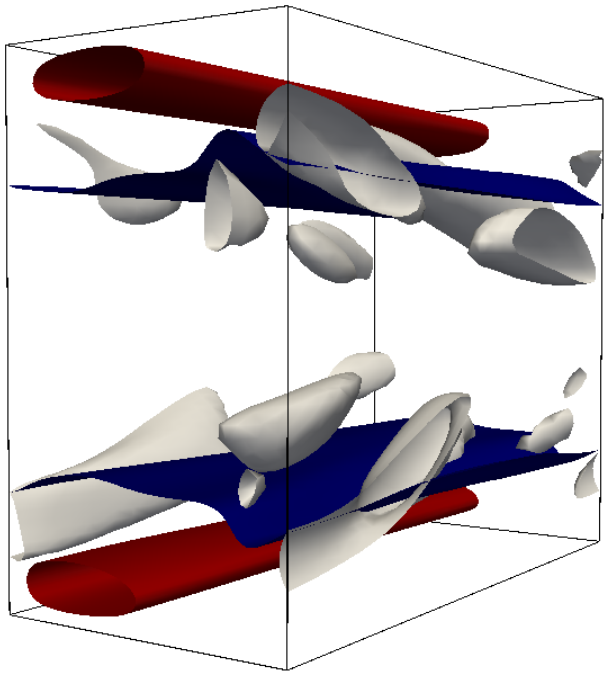

Figure 5.25: 3D representation of the travelling wave

The structure of the TW looks nearly symmetric about the $y = 0$ plane. We listed all possible discrete symmetries of the TW using the *fieldprops* utility from *Channelflow* and found that the TW obeyed none of them exactly. However the mirror symmetry M defined by

$$M\boldsymbol{u}(x, y, z) = \boldsymbol{u}(x, -y, z) \tag{5.10}$$

was the only symmetry which the TW seemed to nearly obey. We obtain $|M\boldsymbol{u} - \boldsymbol{u}|/|\boldsymbol{u}| \approx 2 \times 10^{-3}$ for the TW.
We computed several trajectories starting from the travelling wave with an initial condition of the form

$$u_0 = u_{TW} + 0.01 \times ef_n \tag{5.11}$$

and

$$u_0 = u_{TW} - 0.01 \times ef_n \tag{5.12}$$

where the travelling wave is perturbed along the n-th eigenfunction ef_n, in two opposite directions. These trajectories were plotted in the symmetric phase space, with the variables s_u, s_v, and s_w being defined as in section 4.1.1.
Shown in Figs. 5.26, 5.27 and 5.28 are the plots of the variables s_u, s_v and s_w against time for the trajectories perturbed along the eigenvectors ef_1, ef_2 and ef_6, i.e., the most unstable complex eigenpair and the second real eigenvector in eigenspectrum shown in the Fig. 5.23.

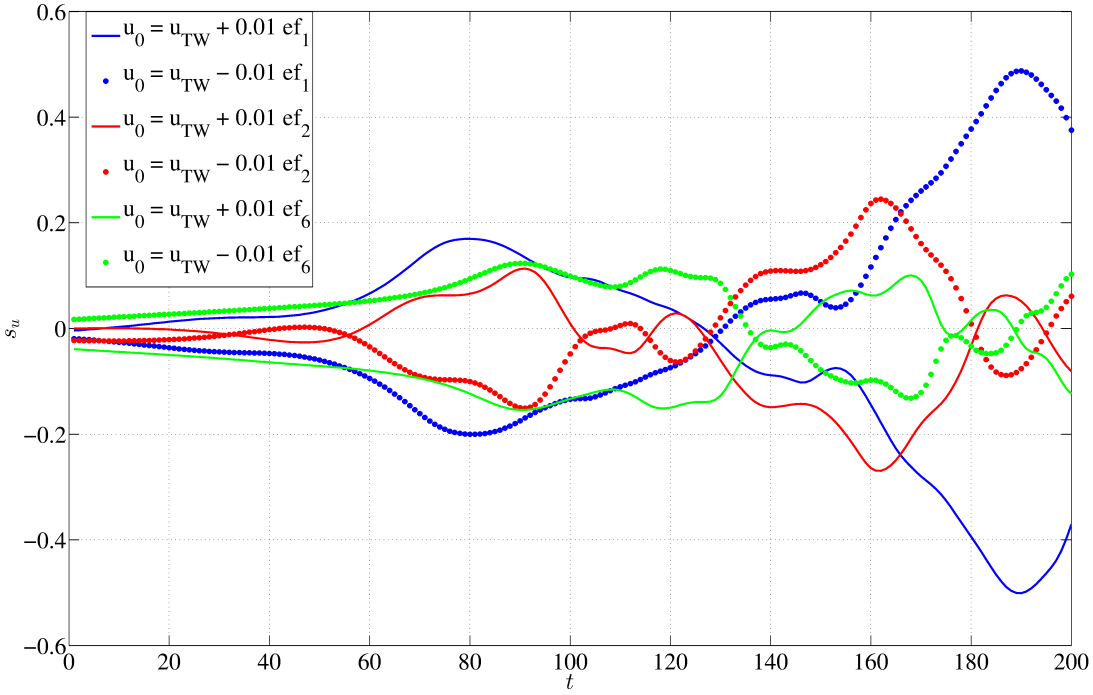

Figure 5.26: s_u vs t, Initial condition of the simulations is given by $u_{TW} + ef_n$

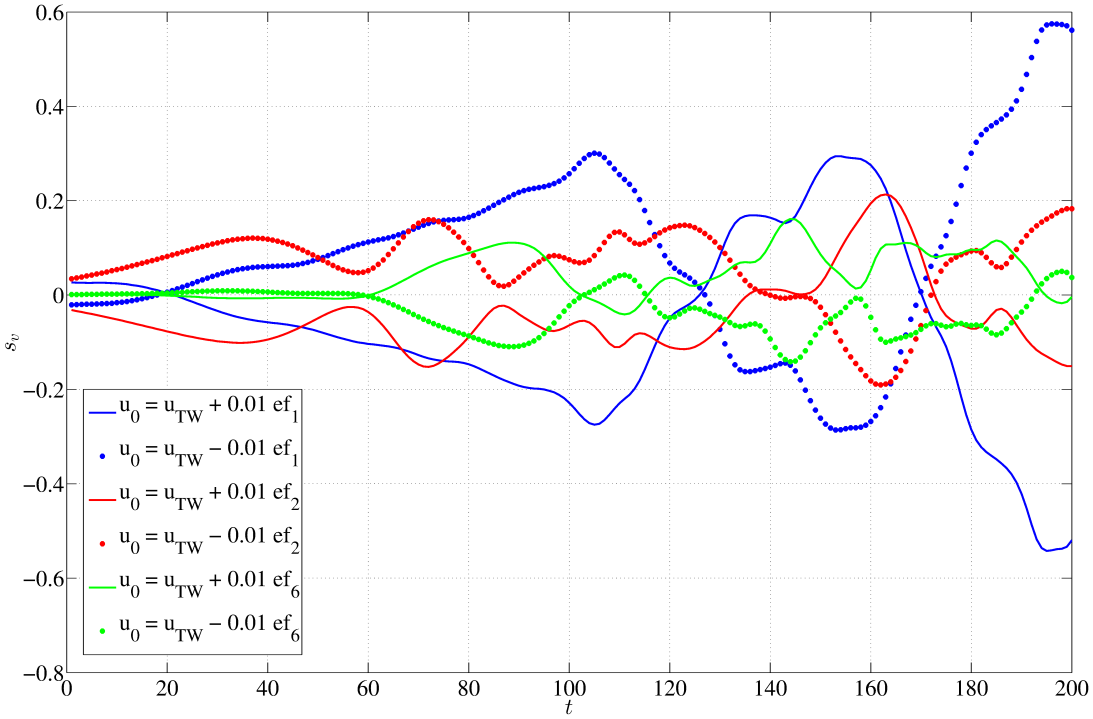

Figure 5.27: s_v vs t, Initial condition of the simulations is given by $u_{TW} + ef_n$

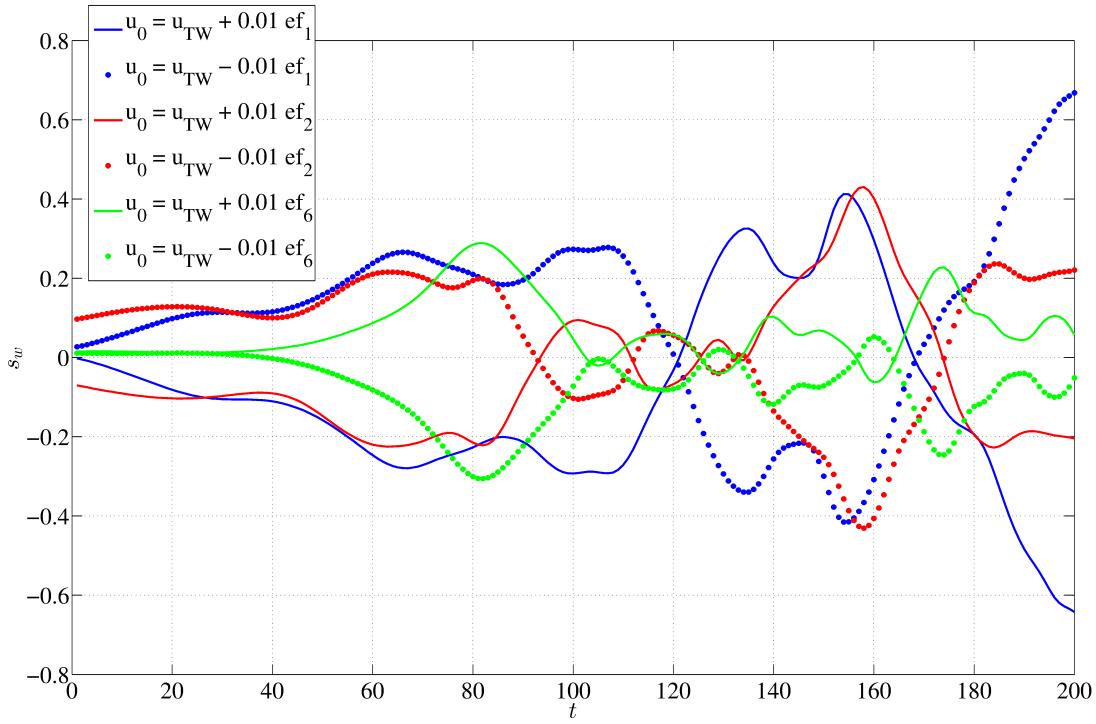

Figure 5.28: s_w vs t, Initial condition of the simulations is given by $u_{TW} + ef_n$

A 3D representation of the resulting trajectories in the symmetric subspace of s_u, s_v and s_w is shown in Fig. 5.29.

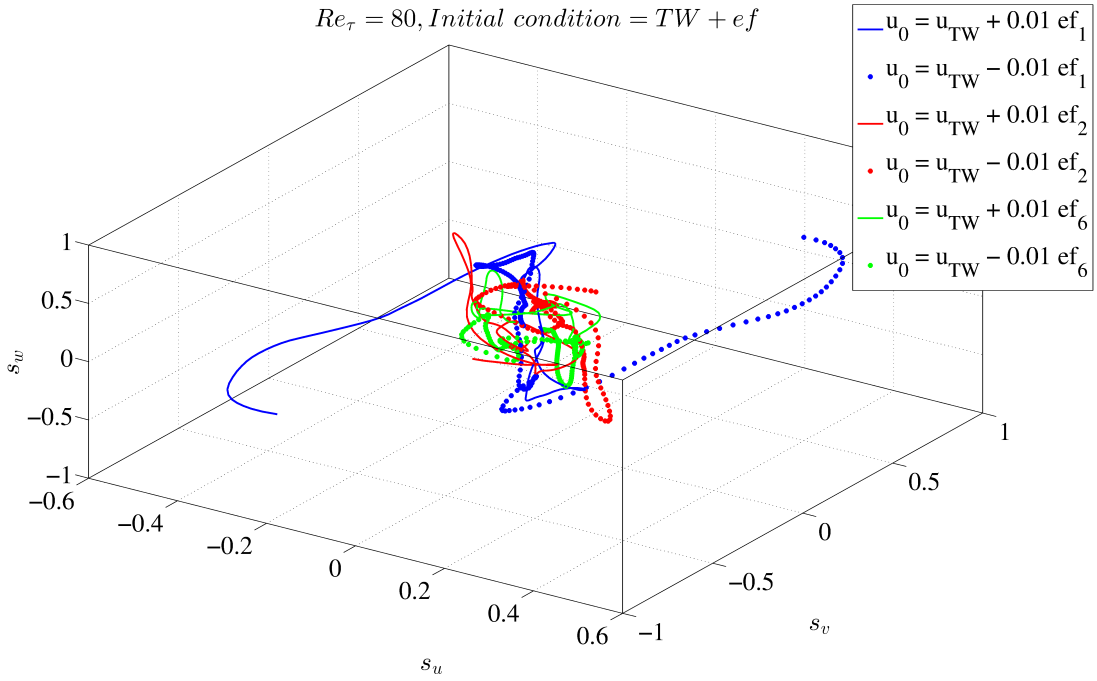

Figure 5.29: 3D representation of simulations with different initial conditions given by $u_{TW} + ef_n$, in the symmetric subspace of s_u, s_v and s_w

In Figs. 5.26 to 5.29 the trajectory evolving from the initial condition

$$u_0 = u_{TW} + 0.01 \times ef_n \tag{5.13}$$

is exactly symmetric to the trajectory evolving from the initial condition

$$u_0 = u_{TW} - 0.01 \times ef_n. \tag{5.14}$$

This result is seen for all chosen eigenvectors, ef_1, ef_2 and ef_6 in the behaviour of all the asymmetry variables s_u, s_v and s_w in Figs. 5.26, 5.27 and 5.28. It was checked one by one that the eigenfunctions associated with ef_1, ef_2 and ef_6 break the $\boldsymbol{s} = 0$ symmetry. Perturbing the travelling wave solution in one of its unstable directions thus leads either to turbulence at the top wall ($s_u > 0$) or at the bottom wall ($s_u < 0$). The flow rate is relatively low during the approach to the $\boldsymbol{s} = 0$ subspace, suggesting a high activity, whereas the edge is characterised by low perturbation energy and higher flow rate. This also excludes the hypothesis that the approach to the corresponds to so-called hibernation events [87]. Several other symmetric travelling wave solutions have been recently identified numerically in [42, 43, 88, 89]. Proper continuation in parameter space would be required to claim that these are the same solutions as the one identified here.

Chapter 6

Relevance of inner scaling vs outer scaling for various flow regimes in wall-bounded flows

6.1 Existing work

It has long been known that the vicinity of the wall consists in organised coherent structures such as streamwise vortices and streaks, and that to a large extent they determine the mean drag exerted by the flow to the wall. For sufficiently large Re, it is also known that the turbulent flow as a whole accommodates a hierarchy of structures of different scales. The multitude of scales obscures the specific energetic contribution of each scale, and though the non-local energy cascade couples all scales together, it is desirable to be able to investigate the dynamics of the wall structures nearest to the wall without the modulation effect by the motions of the logarithmic layer [90].
Jimenéz and Pinelli demonstrated that the dynamics in the M.F.U. is autonomous, i.e. the self-sustaining mechanism at play does not involve outer scales in any way [91]. This simplified M.F.U. system was very popular in the 1990s as the main research was aimed at understanding the minimal protagonists of the self-sustaining process, and the M.F.U. framework provided a relatively cheap computational approach. More recently, the interest has shifted towards large-scale structures (of size comparable to outer scales $\mathcal{O}(h)$). Steady states of minimal plane Couette flow, which are actually edge states, were successfully continued towards increasing Re in a numerical domain with dimensions fixed in units of h [92]. Most Re-continuations by Eckhardt *et al.* in Poiseuille flow were also performed inside a periodic domain of size $\mathcal{O}(h) \times 2h \times \mathcal{O}(h)$ [93]. More recently, a continuation of a symmetric upper branch steady state of plane Couette flow in Re_τ was suggested in [17] by imposing L_x^+ and L_z^+ fixed in inner units rather than outer units. Rawat *et al.* [17] observe, for the upper branch solution of plane Couette flow originally found by Nagata [38], that inner units are not eligible for a self-similarity hypothesis. They find that u_{rms}, when plotted in inner units for different Re does not show a fixed $y_{max} = y|_{u_{max}}$ (where $u_{max} = max(u_{rms})$) see Fig. 6.1. Although continuation was successful, the mean velocity profiles obtained did not satisfy self-similarity in inner units, indicating that the 'natural' scaling of such solutions is in outer units $\mathcal{O}(h)$ rather than in inner units.

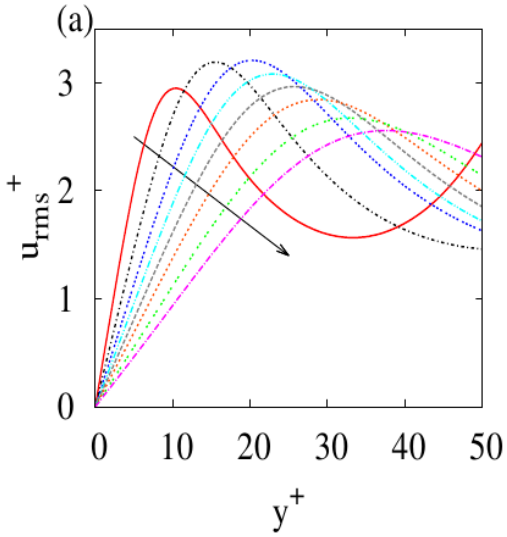

Figure 6.1: The r.m.s. profiles of u vs h, of the upper branch solution of plane Couette flow taken from Rawat *et al.* [17], plotted in inner units.

The arrow in Fig. 6.1 represents the direction of increasing Re. We see that the position of y^+_{max} doesn't stay constant but increases with increasing Re. It can also be seen that u^+_{max} does not show monotonical behaviour, it increases upto a certain value of Re_τ, and then decreases again.
In the present investigation we have identified an exact nearly-symmetric travelling wave as well as several non-symmetric equilibrium regimes with unsteady dynamics, namely the turbulent and edge regimes. Whereas we expect the nearly-symmetric travelling wave to obey a scaling similar to the findings of Rawat *et al.* [17] for plane Couette flow, the wall-localisation of non-symmetric solutions highly suggests that an $\mathcal{O}(h^+)$ scaling could still be relevant for other solutions. We aim here at verifing whether these different flow regimes scale well in inner units.

6.2 Present results

We computed the velocity profiles of different equilibrium regimes for all Re_τ against both outer and inner units, as explained in Chapter 4.
In section 4.1.2, we have computed the r.m.s. velocity profiles of the turbulent simulations in large channels (of dimensions $L^+_x \times L^+_z = 800 \times 400$) 4.1, and we noted that turbulent structures are distributed over both walls. However in the turbulent simulations in M.F.U. channels in section 4.2, we noted the existence of turbulent structures localised near only one of the walls for varying time durations. In order to obtain statistics corresponding to the structures at only one of the walls, we introduce now conditional averaging. Conditional averaging can be thought of as quotienting out the discrete up-down symmetry inherent to the system. The different types of conditional averaging used are as follows :

$$< u_{rms}(y) >_{top} = \frac{\int_0^T \underset{s_u<-0.2}{u_{rms}(y,t)dt}}{\int_0^T \underset{s_u<-0.2}{dt}} \tag{6.1}$$

$$< u_{rms}(y) >_{bot} = \frac{\int_0^T \underset{s_u>0.2}{u_{rms}(y,t)dt}}{\int_0^T \underset{s_u>0.2}{dt}} \tag{6.2}$$

The corresponding r.m.s. velocity profiles in the minimal flow unit channel are computed with condition 6.1, for different Re_τ and plotted in Figs. 6.2 and 6.3.

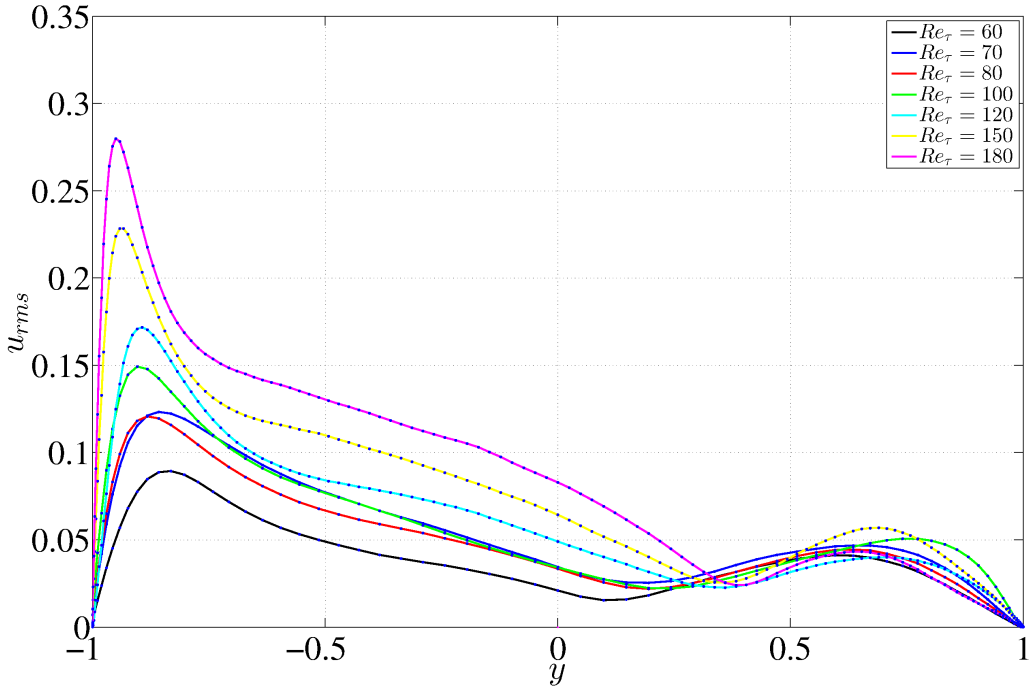

Figure 6.2: Conditional r.m.s. velocity profiles $< u_{rms}(y) >$ for the turbulent simulations, at different Re_τ, plotted in outer units.

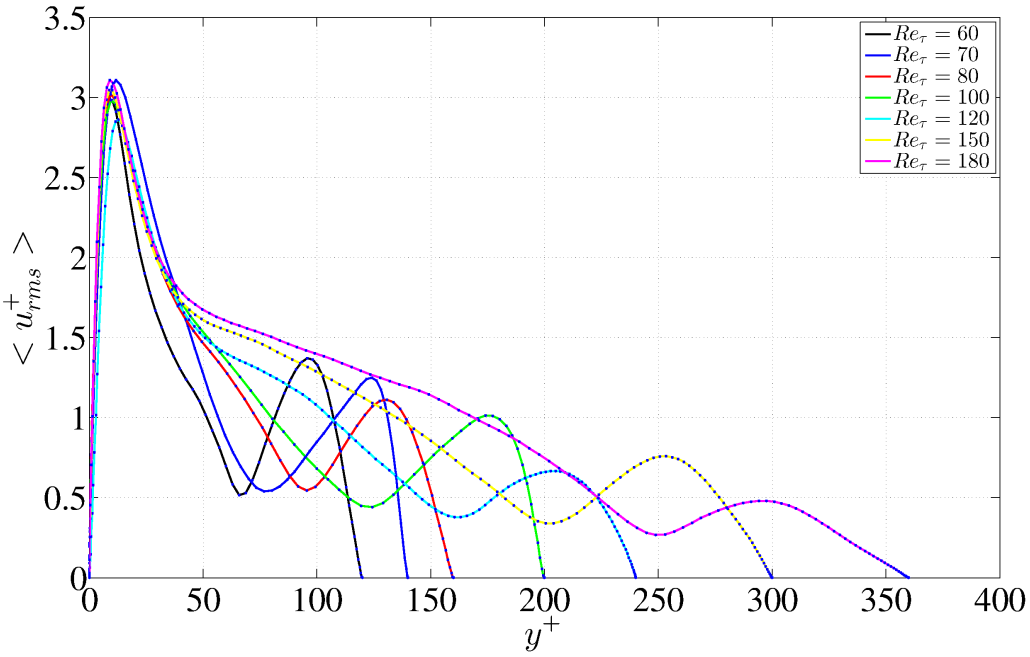

Figure 6.3: Conditional r.m.s. velocity profiles $< u^+_{rms}(y^+) >$ for the turbulent simulations, at different Re_τ, plotted in inner units.

Fig. 6.2 shows $< u_{rms} >$ profiles for the turbulent regime. When $< u_{rms} >$ is plotted in outer units, the position of y_{max} is not fixed, but it approaches the wall as Re_τ increases. However when the same $< u^+_{rms} >$ profiles are plotted in inner units, the profiles completely collapse onto a single curve, close to one wall. This again indicates that the inner units are a better unit to express turbulent features in the minimal flow unit channels also.

In section 4.1.2 of Chapter 4, when unconditioned data was used to compute the r.m.s. velocity profiles of the turbulent simulations, there was no clear scaling either in outer units or in inner units. Yet when conditionally averaged, the r.m.s. profiles of u of the turbulent simulations exhibit perfect self-similarity in inner units as in Jimenéz and Moin. But is this kind of self-similarity of the streamwise velocity profiles also seen in other flow regimes such as the edge state? Is this self-similarity seen only in flows which have near-wall structures or in all kinds of exact solutions of wall-bounded shear flows as well? In fact, the edge state is an equilibrium regime where we have constant Re_τ at statistical equilibrium, $Re_\tau = const$, thus the inner units might well be a good unit of measurement in which the profiles show self-similarity. In order to check this, we plot the streamwise velocity profiles for the edge states obtained at different Re_τ in Fig. 6.4.

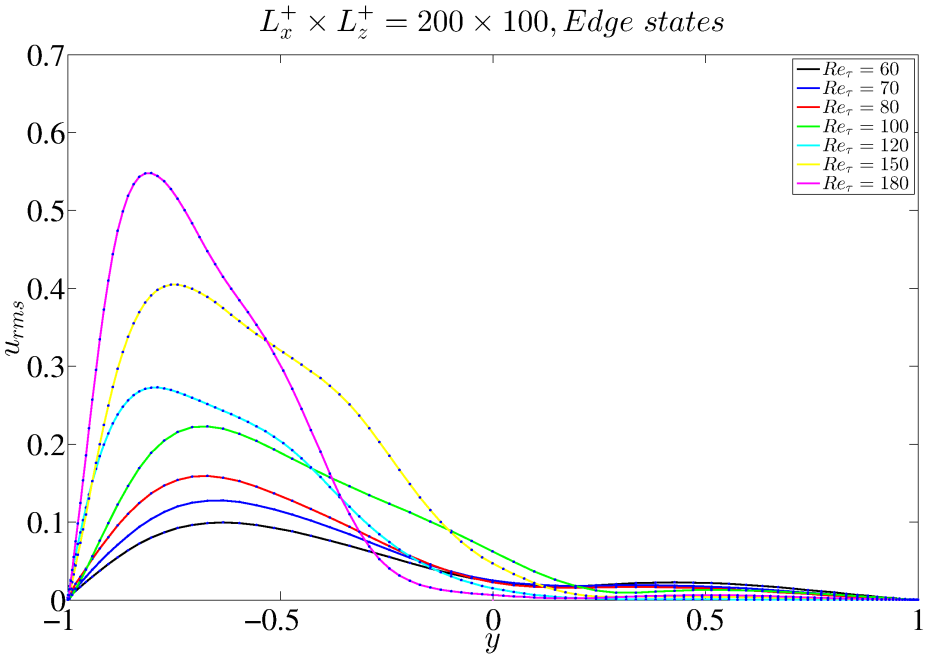

(a) Outer units

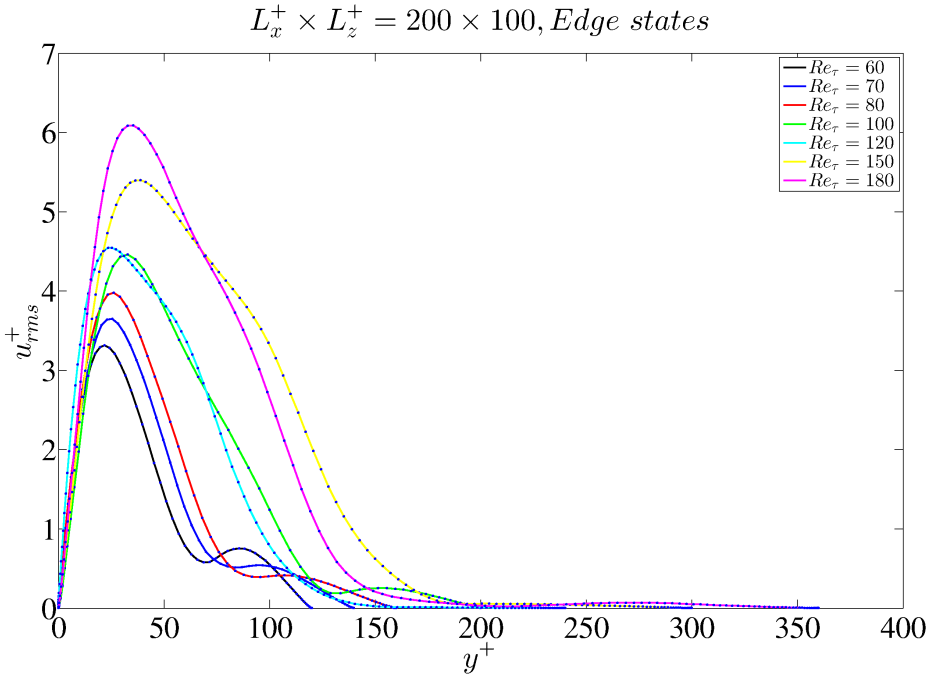

(b) Inner units

Figure 6.4: Conditional r.m.s. profiles $< u_{rms}(y) >$, for the edge states in both outer and inner units.

Figs. 6.4 show that there is no clear self-similarity in the plot of $< u_{rms} >$ when plotted in outer units. Instead, when $< u^+_{rms} >$ in inner units is plotted, there is a clearer pattern of the position of $u^+_{max} = max < u^+_{rms} >$. However, compared to the turbulent case, the self-similarity in inner units is not as satisfactory. For comparison, Rawat *et al.* [17] observe, for the upper branch solution of plane Couette flow, that inner units are not able to explain the self-similarity hypothesis. They find that u_{rms} does not have a fixed y_{max}

when plotted in inner units as shown in Fig. 6.1. This clearly differs from what has been observed in our case for plane Poiseuille flow. What could then be the reason for the difference in scaling seen in the solutions of Rawat *et al.* and the different flow regimes in plane Poiseuille flow discussed in this thesis? The computations by Rawat *et al.* were in the range of $Re_\tau = 33.3$ to $Re_\tau = 99.1$ whereas the computations in this thesis were in the range of $Re_\tau = 60$ to $Re_\tau = 180$, which is still in the "transitional regime". The upper branch solution found by Rawat *et al.* is steady whereas in our system the different non-trivial flow regimes are unsteady. But the unsteadiness of the solution should not influence the scaling of solutions w.r.t. Re_τ. The solutions found by Rawat *et al.* were in plane Couette flow and have an imposed symmetry about the mid-y plane (the up-down symmetry) at all times. All the simulations of plane Poiseuille flow in this thesis have been carried out without imposing the "up-down" symmetry. A major difference between the states found by Rawat *et al.* and our states, is thus apparently the physical structure of the velocity field. For comparison, the structure of the upper branch solution obtained by Rawat *et al.* is shown in Fig. 6.5.

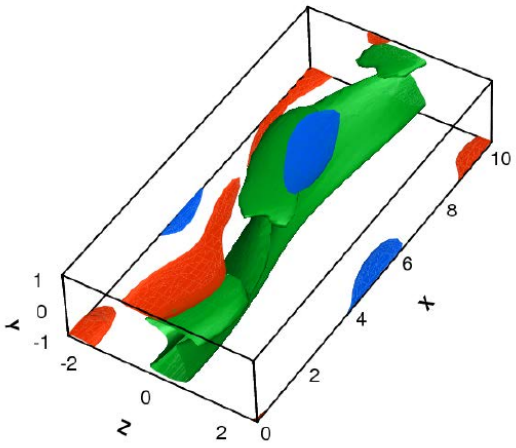

Figure 6.5: The 3D representation of the streamwise velocity component, of the upper branch solution, taken from Rawat *et al.* [17].

Note that this solution has the same structure as the upper branch equilibrium solution of Gibson shown in Fig. 1.14(b) in section 1.7. It contains streaks at both walls as a consequence of the imposed symmetry. The structures in our simulations, both for the edge state and turbulent flow yet turn out to be confined to one of the walls instead. This difference in the localisation of the two different flow regimes could be one of the reasons why there is a different scaling for the solutions by Rawat *et al.* and the solutions found in this thesis. In order to have a better quantitative picture of why the scaling of u_{max} and y_{max} differ between our computations and those of Rawat *et al.*, we plot u_{max} and y_{max} for the turbulent simulations as functions of Re_τ, see Figs. 6.6 and 6.7.

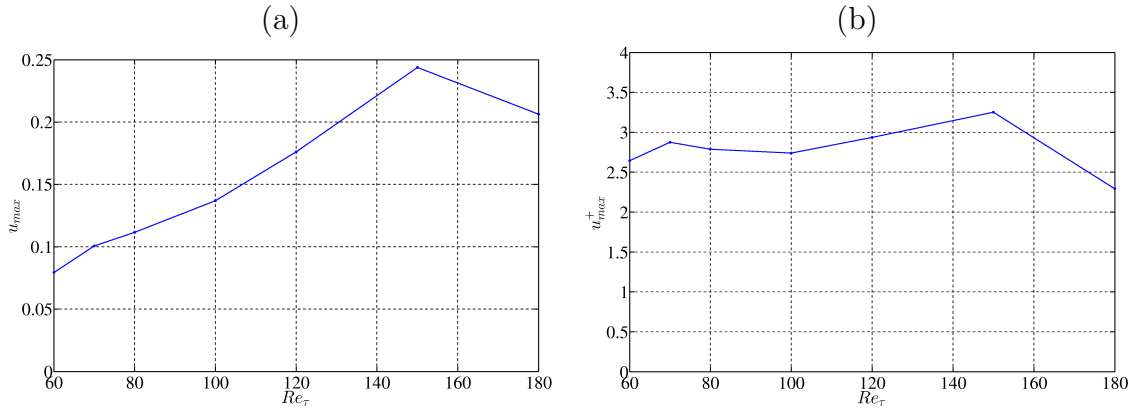

Figure 6.6: $u_{max} = max(< u^+_{rms} >)$ as a function of Re_τ for the turbulent states, in (a) outer units and (b) inner units.

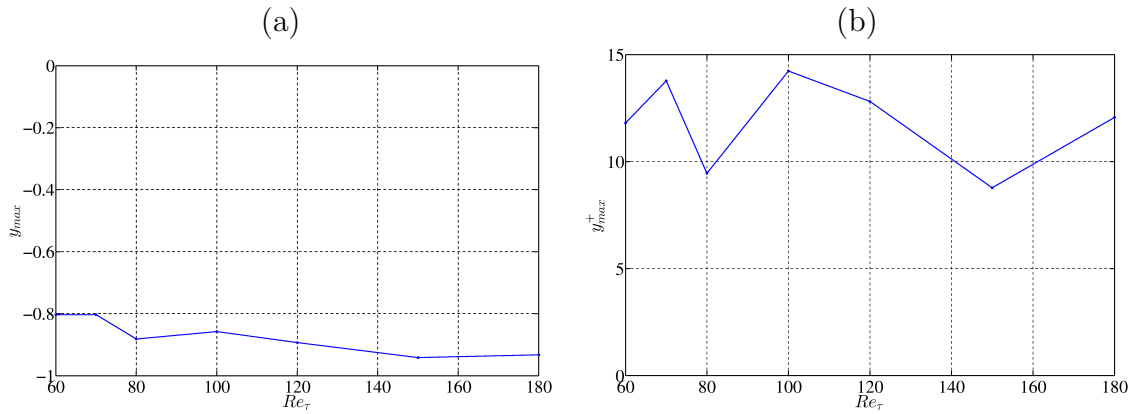

Figure 6.7: $y_{max}(Re_\tau)$ for the turbulent states, in (a) outer units and (b) inner units.

Fig. 6.6 shows that there is not a huge variation in the values of u_{max} with Re_τ, which is on expected lines since turbulent simulations are known to be self-similar. Similarly it can be seen from Fig. 6.7 that the range of y^+_{max} w.r.t. Re_τ is small, thereby confirming the inner scaling for the turbulent simulations in the inner units. The quantities u_{max} and y_{max} were also plotted for the edge states as a function of Re_τ in Figs. 6.8 and 6.9.

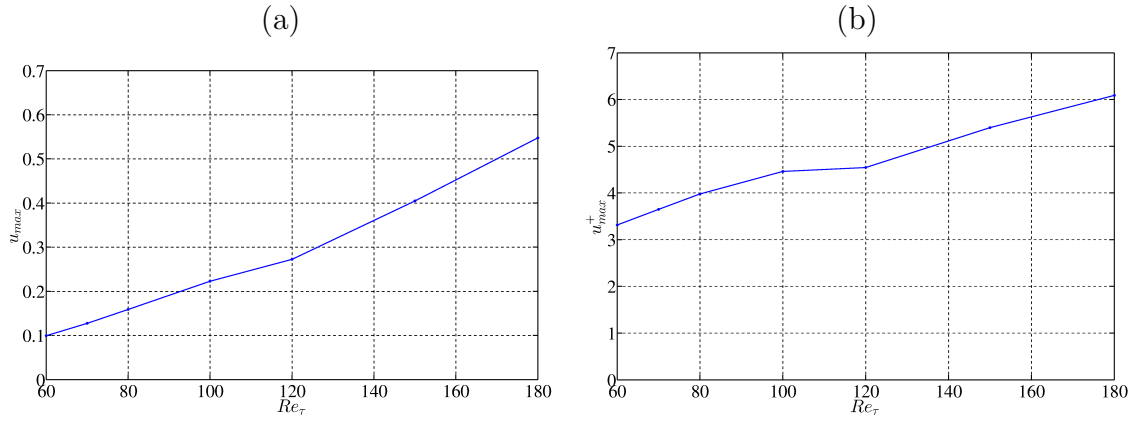

Figure 6.8: $u_{max} = max(< u^+_{rms} >)$ as a function of Re_τ for the edge states, in (a) outer units and (b) inner units.

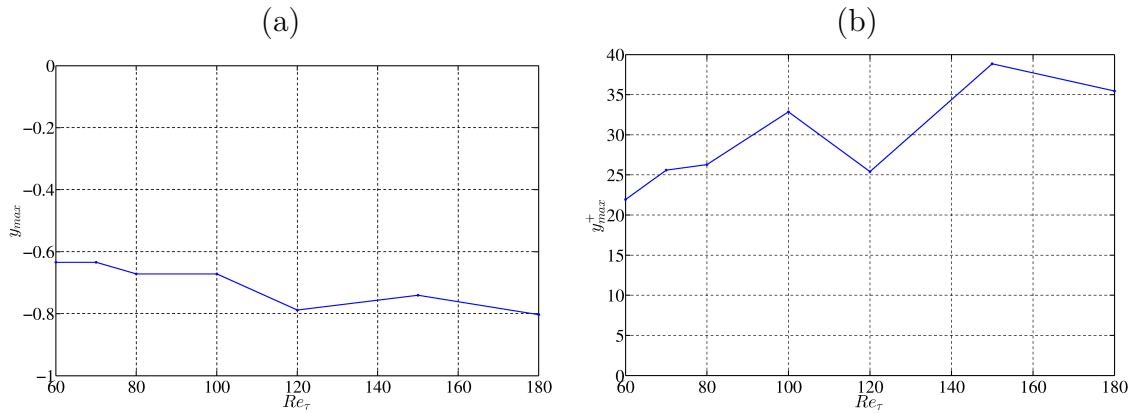

Figure 6.9: $y_{max} = y|_{u_{max}}$ as a function of Re_τ for the edge states, in (a) outer units and (b) inner units.

The results appear at first sight mixed : no clear independent values of y^+_{max} emerges from this parametric study, and no clear constant value of y_{max} either from Figs. 6.9. Instead the results point towards a mixed scaling relation : from Fig. 6.8, we see that $u^+_{max}(Re_\tau)$ varies over a range from 1 to 2 as Re_τ varies by a factor of 3, whereas $u_{max}(Re_\tau)$ varies by a factor from 1 to 6, which still suggests that the inner scaling has some relevance.

6.3 Conclusion

In conclusion, it is noted that one of the non-symmetric equilibrium regimes, i.e. the turbulent regime in a channel of M.F.U. dimensions were found to scale well in inner units. This matches well the earlier findings of Jimenéz and Moin [1]. Another equilibrium regime, the edge state for different Re_τ did not show as good a scaling in inner units as the turbulent states. In comparison, the edge states do not even show a good scaling in outer units as seems to be the case with the upper branch solutions of plane Couette flow of Rawat *et al.* [17] or Wang *et al.* [92]. Clearly the y-localised solutions obey a scaling different from that for the symmetric ones found by Rawat *et al.*. It is postulated

that this could be a result of the difference in the structure and span of the two solutions : whereas the upper branch solutions of plane Couette flow has a 3D structure spread throughout the domain, the edge states found in the M.F.U. domain of plane Poiseuille are localised near either of the walls. If the main difference between the the present edge states and the solutions of Rawat *et al.* is this property of y-localisation, it becomes only well-marked for increasing Re_τ , which suggests to push this investigation to higher values of Re_τ (requiring an increase of resolution in the y direction). We hence deduce from this analysis that y-localised equilibrium regimes, unlike symmetric ones, may well scale in inner units, keeping in mind that this hypothesis requires higher values of Re_τ for confirmation. It remains to be checked whether there is a "composite" scaling to be identified - the composite scaling could also be a small Re_τ effect. This hypothesis has important consequences for anyone desiring to push the investigation of the state space towards higher Reynolds numbers.

Chapter 7

Discussion, Perspectives, Conclusion

The present investigation of a Minimal Flow Unit (M.F.U.) of pressure-driven plane Poiseuille flow shows interesting features. We looked for exact coherent states that were neither laminar nor turbulent ("edge states"), so as to gain insights into the dynamics underlying the transition to turbulence. Edge states were found using the classical bisection algorithm for a range of values of Re_τ, with the edge states at lower Re_τ ($Re_\tau \leq 80$) being relative periodic orbits, and the edge states at higher Re_τ being chaotic. 3D visualisation of the edge states showed the presence of high speed and low speed streaks along with streamwise vortices, typical of other exact coherent states observed earlier in shear flows, strengthening the self-sustaining hypothesis of the transition process proposed by Waleffe [8]. The relative periodic orbits have a calm phase followed by a short burst phase followed by a spanwise shift of the streaks. The edge states and the turbulent trajectories were represented in a state space constructed using the asymmetry variables s_u, s_v and s_w. The state space seems organised around two repelling turbulent regimes symmetric of each other. The observed reversals involve visits to the $s = 0$ subspace built around one or several exact unstable symmetric solutions. One such solution was identified by recurrence analysis in the quotiented space, in the form of a nearly-symmetric travelling wave solution. The quotienting method which we introduced, worked well enough to spot visits to a travelling wave, but requires improvement in order to locate relative periodic orbits. It was verified that this travelling wave solution is not on the edge. Besides its unstable eigenvectors break the $s = 0$ symmetry, separating the state space into two symmetric basins. A self-similarity analysis was done in order to understand how the different solutions scaled. Since the solutions found in M.F.U. are generally localised near either of the walls, we introduced a conditional averaging based on the value of s_u. It was found that the turbulent solutions scaled perfectly in inner units, which is in line with earlier observations by Jimenéz and Moin [1]. The edge states were found not to scale as well in inner units as the turbulent solutions, nevertheless the inner units scaling was preferred to outer unit scaling even among the edge states when the values of u_{max} were plotted. It remains to be verified whether there is indeed a "composite scaling" to be identified by continuing the computations to much higher Re_τ.

This investigation should be seen as preliminary as it leaves many questions unanswered. A deterministic description of the phase space was given and an analysis of the scaling of the different solutions found in minimal plane Poiseuille flow has been carried out, but can the results be generalised for M.F.U. domains of all shear flows? Can the same be done at a scale which is not M.F.U. i.e. at intermediate and large scales? From a mechanical

point of view, why does confinement by the periodic boundary conditions lead to turbulent activity being restrained to one wall only? Another obvious hypothesis to be checked is to continue the travelling wave solution to higher Re_τ, and to check whether the travelling wave solutions also scale in inner units in the M.F.U.. From a dynamical point of view, many other invariant sets are expected to populate the phase space, among them other travelling waves, periodic orbits and connections between them [61].

Appendix A

In press for Fluid Dynamics Research

State space analysis of minimal channel flow

Shreyas Acharya Neelavara[1], Yohann Duguet[1] and François Lusseyran[1]

[1]LIMSI-CNRS, Campus Universitaire d'Orsay, Université Paris-Saclay, F-91405 Orsay, France

E-mail: acharya@limsi.fr

Abstract. Turbulence and edge states are investigated numerically in a plane Poiseuille flow driven by a fixed pressure gradient. Simulations are carried out within the minimal flow unit, a concept introduced by Jimenéz & Moin (1991) to unravel the dynamics of near-wall structures in the absence of outer large-scale motions. For both turbulent and edge regimes the activity appears to be localised near only one wall at a time, and the long term dynamics features abrupt reversals. The dynamics along one reversal is structured around the transient visit to a subspace of symmetric flow fields. An exact travelling wave solution is found to exist very close to this subspace. Additionally the self-similarity of the asymmetric states is addressed. Contrary to most studies focusing on symmetric solutions, the present study suggests that edge states, when localised near one wall, do not scale in outer units. The current study suggests a composite scaling.

Keywords: transition to turbulence, exact coherent solutions, wall turbulence, reversals

1. Introduction

The structure and dynamics of wall turbulence remains one of today's great challenges in fluid mechanics. It has long been known that the vicinity of the wall consists of organised coherent structures such as streamwise vortices and streaks, and that to a large extent they determine the mean drag exerted by the flow on the wall. For sufficiently large Reynolds numbers, it is also known that the turbulent flow as a whole accommodates a hierarchy of structures of different sizes. The popular picture of wall-attached eddies has been suggested by Townsend (Townsend 1980), according to which vortical structures originate from the wall and can be ranked in increasing size. For the case of a channel between two walls separated by a gap $2h$, driven by a fixed pressure difference Δp, the largest structures have a maximal wall-normal extent of $2h$. The smallest turbulent structures, in turn, are thought to be independent of the gap size. Their size depends only on the mean shear at the wall $\partial u/\partial y|_w$, which is statistically imposed by the pressure gradient. Together with the kinematic viscosity ν, it defines another length scale $l_\nu = \nu/u_\tau$, where $u_\tau = \sqrt{\nu \partial u/\partial y|_w}$ is a reference velocity scale. The hierarchy of scales is governed by the non-dimensional parameter $Re_\tau = u_\tau h/\nu = h/l_\nu$, which indicates the ratio of the largest to the smallest scales in the flow.

The multitude of scales obscures the specific energetic contribution of each scale, and though the non-local energy cascade couples all scales together, it is desirable to be able to investigate the dynamics of the wall structures nearest to the wall without the modulation effect (Mathis et al. 2009) by the outer motions of the log layer. Jimenéz and Moin (1991) suggested that direct numerical simulation in periodic boxes could offer a means to investigating small scales autonomously from the larger ones. By reducing, for a given value of Re_τ, the streamwise and spanwise dimensions of the numerical domain, they could identify the dimensions of a Minimal Flow Unit (MFU) below which turbulence could not be sustained. Importantly, the size of the MFU is independent of Re_τ when expressed in units of l_ν, also labelled 'inner' or 'wall' units (and marked with a $^+$ symbol). They furthermore demonstrated that the dynamics in the MFU is autonomous, i.e. the self-sustaining mechanism at play does not involve outer scales in any way (Jiménez & Pinelli 1999). This simplified system was very popular in the 1990s as the main research was aimed at understanding the minimal protagonists of the self-sustaining process, and the MFU framework provided a relatively cheap computational approach. More recent work has also focused on the autonomous properties of larger scales (Hwang & Cossu 2010, Rawat et al. 2015, Hwang & Bengana 2016, Hwang et al. 2016) by filtering out smaller scales using a subgrid model.

Largely inspired by the MFU approach, a growing body of literature has emerged in the context of plane Couette or fixed mass-flux cylindrical pipe flow, addressing the system as a deterministic nonlinear system of the generic form $d\boldsymbol{X}/dt = \boldsymbol{F}(\boldsymbol{X})$. The confinement by the boundary conditions indeed makes the original system spatially cor-

related, which justifies such an approach rather than a fully spatiotemporal approach. In this paradigmatic view, tools borrowed from dynamical systems theory have proven useful to describe accurately the structure of the associated state space (Cvitanović 2013). This state space is formally of infinite dimension, though in practice dissipation coupled with numerical truncation makes it a finite, yet very high-dimensional state space (Eckhardt et al. 2008). This accurate characterisation, more descriptive than truly quantitative, relies on the numerical identification of the most important invariant sets, among them fixed points, periodic orbits and their connecting manifolds (Kawahara et al. 2012). A technical obstacle is the consideration of all discrete and continuous symmetries of the system (Willis et al. 2013). Nevertheless, this paradigm has proven successful at making explicit in a deterministic manner some building blocks of the recurrent dynamics observed : for instance, (Kawahara & Kida 2001) identified in plane Couette flow an exact periodic orbit, which in physical space corresponds to the cyclic regeneration of streaks involving a bursting event and vorticity redistribution. Another successful concept is that of the *edge*, namely the state space manifold separating relaminarising trajectories from those experiencing transition to turbulence (Skufca et al. 2006, Schneider et al. 2007). This concept is crucial to explain transition in the absence of linear instability of the laminar base flow $\boldsymbol{u}_L = (1 - y^2, 0, 0)$. The edge supports relative attractors that can be fixed points, periodic orbits, or more complicated invariant sets, e.g. low-dimensional chaos. The edge state, i.e. the asymptotic attractor for trajectories confined to the edge, is not necessarily unique, but it is always unstable in the full state space. It is nevertheless an equilibrium regime of the flow in addition to the expected laminar and turbulent regimes. Behind the existence of fixed points, equilibria... remains the question of understanding which hydrodynamic mechanisms allow for non-trivial fluid motion to be self-sustained. Another crucial question, intrinsically linked with the issue of numerical confinement by boundary conditions, is the typical scale (in physical space) of the coherent structures associated with these (state-space) invariant sets. Originally, the literature on applications of dynamical systems to the problem of shear flow turbulence focused on near-wall structures, and on understanding the so-called near-wall cycle (Hamilton et al. 1995, Waleffe 1997, Jiménez et al. 2005), by selecting minimal domains and small Reynolds numbers. Paradoxically, using the same methodology the focus shifted within a few years towards the description of the large-scale structures of wall turbulence. Continuation of exact coherent structures in parameter space has been for instance almost invariably conducted using outer (h) rather than inner (l_ν) units (see e.g. (Wang et al. 2007)). This appears in total contradiction with the original investigations of near-wall coherent structures, for which most turbulent studies predict an inner scaling in units of l_ν, implying that near-wall eddies shrink with increasing pressure drop when measured in units of the gap h. Since the natural applications of wall turbulence theories aim at high Reynolds numbers, this overlooked distinction between inner and outer scaling is expected to matter, should further progress in the investigation of high Reynolds numbers using dynamical systems tools be achieved in the near future.

We report here a numerical investigation of the state space of the original MFU system in pressure-driven channel flow addressing the questions above. The plan of the paper is as follows : the numerical tools are described in Section 2, and simulations of edge and turbulent regimes as Re_τ increases are shown in Section 3. Finally, the issue of the self-similarity of both turbulent and edge regimes is addressed in Section 4.

2. Numerical system and observables

We consider the flow of incompressible viscous fluid driven in a channel geometry by a constant pressure gradient Δp. The mass flux is not fixed but depends on time and varies strongly between the laminar and turbulent regime. When non-dimensionalised in outer units of the mid-gap h, the governing Navier-Stokes equations for the flow read

$$\frac{\partial \boldsymbol{u}}{\partial t} + (\boldsymbol{u}\cdot\nabla)\boldsymbol{u} = -\nabla p + \frac{1}{Re}\nabla^2\boldsymbol{u} \tag{1}$$

$$\nabla\cdot\boldsymbol{u} = 0, \tag{2}$$

where $Re := u_{cl}h/\nu$, u_{cl} being the centreline velocity for the equivalent laminar base flow, ν the kinematic viscosity and h the half-gap between the two walls. The fluid density ρ has also been normalised to unity. The pressure difference $\Delta p < 0$ imposed to drive the flow is equilibrated by the drag at the wall, which fixes the value of $Re_\tau = \sqrt{-\Delta p}$ at equilibrium independently of the regime in which the flow operates (laminar, edge or turbulent). For the values of Re_τ considered in this paper, the laminar base flow is linearly stable.

The system (1,2) is simulated using the open-source spectral code channel flow.org (Gibson 2008). No-slip boundary conditions are imposed at the walls of the channels and periodic conditions with periods L_x and L_z respectively in the x (streamwise) and z (spanwise) directions:

$$\boldsymbol{u}(x,\pm 1,z) = 0, \tag{3}$$

$$\boldsymbol{u}(x+L_x,y,z) = \boldsymbol{u}(x,y,z), \tag{4}$$

$$\boldsymbol{u}(x,y,z+L_z) = \boldsymbol{u}(x,y,z). \tag{5}$$

The spectral decomposition of the flow field reads

$$\boldsymbol{u} = \sum_{k=-K}^{K}\sum_{m=-M}^{M}\sum_{n=0}^{N} T_n(y)\exp \mathrm{i}[k\alpha x + m\beta z]$$

where K, M and N are positive integers, $T_n(y)$ are Chebyshev polynomials, and (α,β) is the fundamental wave vector. The timestepping algorithm with variable time step combines a Crank-Nicolson scheme with a second order Adams-Bashforth scheme for the nonlinear terms, and the maximum timestep is fixed to $= 0.02$ in units of h/u_{cl}.

As mentioned in the introduction, the original concept of MFU implies that L_x and L_z depend on the value of Re_τ. In agreement with both the original study and all

Re_τ	L_x	L_z	$N_x \times N_y \times N_z$
60	3.33	1.67	$32 \times 65 \times 32$
70	2.86	1.43	$32 \times 65 \times 32$
80	2.5	1.25	$32 \times 65 \times 32$
100	2	1	$32 \times 65 \times 32$
120	1.67	0.83	$32 \times 129 \times 32$
150	1.33	0.67	$32 \times 129 \times 32$
180	1.11	0.56	$32 \times 129 \times 32$

Table 1. Numerical parameters and domain size in outer units.

studies of wall turbulence ever since, we set $L_z = 100 l_\nu/h$ which stands for the width of a pair of streaks. Given the definition of Re_τ, this is equivalent to imposing in non-dimensional outer units $L_z = 100/Re_\tau$. The minimal value of L_x, corresponding to the actual length of turbulent streaks, is harder to identify and is usually considered to lie in the range 300–1000. We found by inspection that turbulence could still be sustained over long yet finite times by choosing L_x as low as $200 l_\nu/h$, i.e. $L_x = 200/Re_\tau$. Because of non-zero relaminarisation probabilities, the exact minimal values of $L_x^+ = L_x \times Re_\tau$ and $L_z^+ = L_z \times Re_\tau$ able to sustain non-trivial motion appear dependent on the observation time and this question is not really addressed here. All simulations are performed with $(N_x, N_y, N_z) = (32, 65, 32)$, and $(32, 129, 32)$ for $Re_\tau \geq 120$. The values of Re_τ considered here (from 60 to 180) are listed in Table 1 together with the domain size reported in outer units.

If the perturbation to the laminar base flow $\boldsymbol{u}_L$ reads $\boldsymbol{u}' = (u, v, w)$, one of the usual observables is the kinetic energy of the flow

$$E(t) = 1/2 \int_0^{Lx} \int_0^{Lz} \int_{-1}^{1} |\boldsymbol{u}'|^2 dx dz dy. \tag{6}$$

It is sometimes useful to consider as well the energy contained in the wall-normal component by

$$E_v(t) = 1/2 \int_0^{Lx} \int_0^{Lz} \int_{-1}^{1} v^2 dx dz dy, \tag{7}$$

which vanishes for the laminar base flow.

In order to quantify the temporal reversals of the perturbation velocity field, we introduce the following time-dependent observable

$$s_u = \frac{I^- u - I^+ u}{I^- u + I^+ u}, \tag{8}$$

where

$$I^- u = \int_{-1}^{0} u_{rms}(y) dy, \tag{9}$$

$$I^+u = \int_0^1 u_{rms}(y)dy, \tag{10}$$

and *rms* denotes the spatial root-mean square values after averaging in the x and z directions. Similar observables s_v (resp. s_w) can be constructed for the component v (resp. w). Visualisations in the (s_u, s_v, s_w) space are interpreted as phase portraits of the dynamics. We sometimes use the compact vector $\boldsymbol{s} = (s_u, s_v, s_w)$. Such observables show the advantage of being insensitive to spatial shifts in x and z. We also define the mirror symmetry M_y acting on $\boldsymbol{u}$ by

$$M_y : [u, v, w](x, y, z) = [u, -v, w](x, -y, z). \tag{11}$$

Applying M_y to any state only results in a change of sign of s_u, s_v and s_w. States invariant by M_y are also labelled 'symmetric', while states with $\boldsymbol{s} \neq 0$ are 'asymmetric'. Note that while all symmetric states satisfy $s_u = s_v = s_w = 0$, the converse is not true, hence using these notations there exists states which are neither symmetric nor asymmetric. Two states that can be mapped into each other by the application of M are sometimes labelled 'symmetry-related'.

The system in Eq. (1) together with the boundary conditions in Eq. (5) is also equivariant with respect to other discrete and continuous symmetries : any translation σ_x (resp. σ_z) in x (resp. in z), as well as the reflection M_z about the $z = 0$ plane leave the system unchanged. As a consequence the symmetry group of the present system is generated by M_y, M_z and the continuous translations σ_x and σ_z, see also (Gibson & Brand 2014).

Edge states are computed using the standard algorithm of bisection introduced in (Skufca et al. 2006) : the amplitude of an arbitrary initial condition is rescaled until the flow reaches neither laminar nor turbulent level for a sufficiently long observation time. The process is re-started once machine precision is reached. The observable chosen to diagnose between relaminarising and transitioning trajectories is the wall-normal energy E_v introduced in Eq. (7). The Newton-Krylov algorithm included in channelflow.org, augmented by the Hook-Step globalisation technique (Viswanath 2007), has been used to successfully converge travelling-wave solutions within an accuracy of $O(10^{-12})$.

3. Structure of the state space

We illustrate first the properties of the MFU system by reproducing the dynamics originally observed by Jimenéz & Moin (1991) but with $L_z = L_x/2 = 100l_\nu$. Turbulent signals are displayed in Fig. 1 using the energy observable E_v. It is noteworthy that all trajectories eventually relaminarise for times less than 5000 in units of h/u_{cl}, whereas for equivalent Reynolds numbers in larger domains turbulent lifetimes are higher by several orders of magnitude (Hof et al. 2008). This is interpreted as a confinement effect

due to the small value of L_x^+. Three-dimensional visualisations of instantaneous velocity fields are reported in Fig. 2 for several values of Re_τ, together with visualisations of isovalues of the Q-criterion revealing vortical structures, with $Q = \boldsymbol{\nabla}^2 p/2$. As is known from the prior literature, the turbulent activity is clearly localised near one wall only most of the time (Jiménez & Moin 1991), corresponding to a given sign of s_u. It features a unique low-speed streak flanked with streamwise vortices on its side. The temporal dynamics of s_u is reported in Fig. 3. Reversals of s_u correspond to the turbulent activity migrating from one wall to the next, with a transient featuring a short but noticeable phase where $s_u \approx 0$. It is very tempting to relate those observations to other physical systems displaying reversals, such as the Earth's magnetic field. In particular, such systems are usually modelled as potential systems of the form $dX_i/dt = -\partial V/\partial X_i + \eta(t)$ featuring both a noise term $\eta(t)$ and symmetry in the structure of V. In such systems, the dynamics randomly hops from one potential well to the next back and forth, and the residence times usually obey Kramers' law (Coffey et al. 2004). The present system differs by its entirely deterministic nature, the role of the noise being played by the (non-small) turbulent fluctuations themselves.

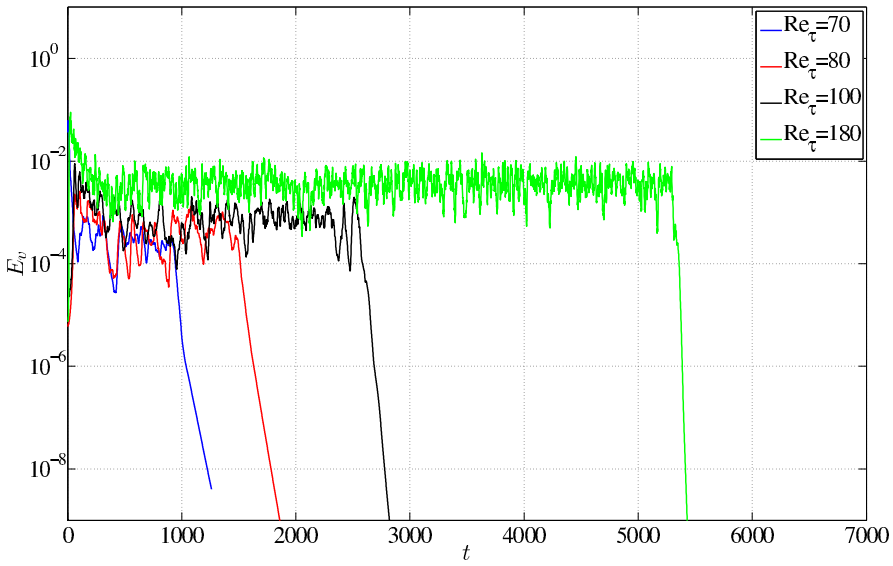

Figure 1. Signals of $E_v(t)$ for various values of Re_τ (t in units of h/u_{cl}).

Edge states are computed for the parameters in Table 1, starting usually from a turbulent velocity field as initial condition for the bisection algorithm. Signals of $E_v(t)$ are displayed in Fig. 4. The energetic dynamics on the edge appears as periodic for $Re_\tau \leq 80$ and chaotic above. Analysis of the periodic regimes shows that the edge state is actually relative periodic, i.e. $\boldsymbol{u}(x, y, z, t + T) = \boldsymbol{u}(x + \sigma_x, y, z + \sigma_z, t)$ with σ_x and σ_z spatial shifts in the x and z directions. The associated period T observed in Fig. 4 is around $1700h/u_{cl}$ for the parameters chosen here. We found that $\sigma_z = L_z/2$ so that the edge state is actually relative periodic with a shift in x only, and a true period of

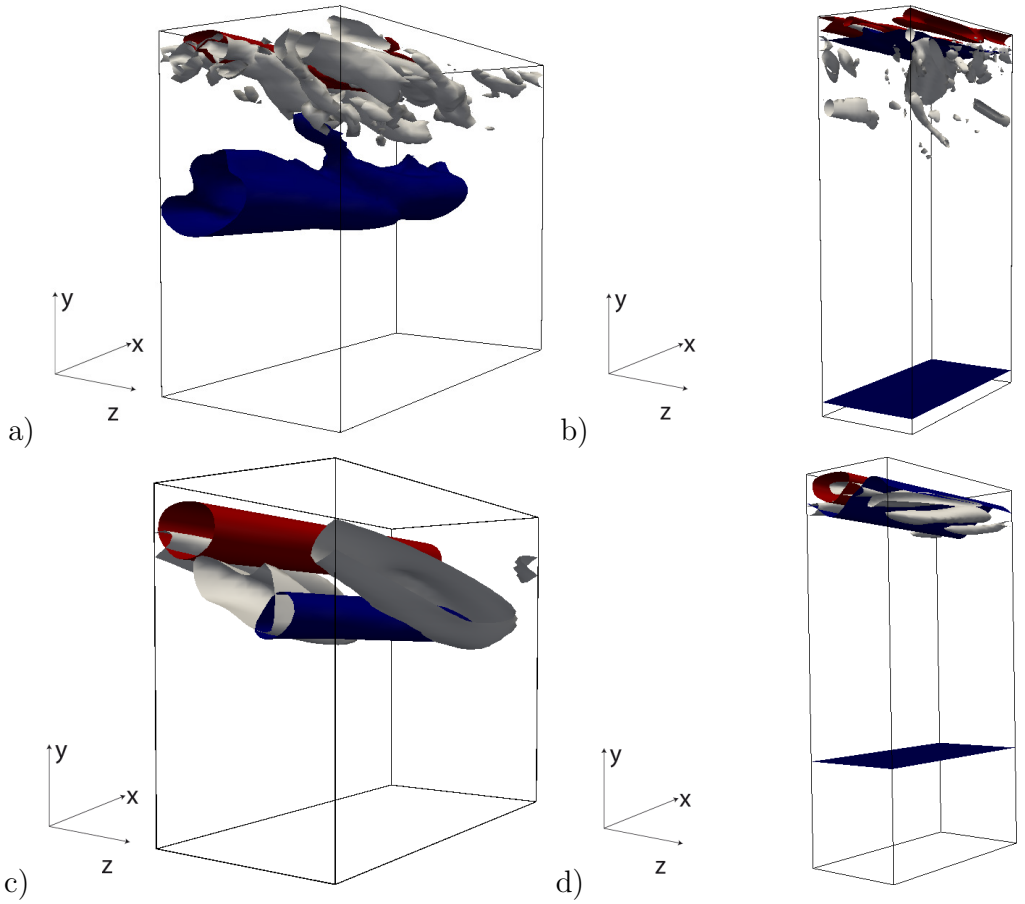

Figure 2. Three-dimensional visualisations of snapshots in the turbulent regime at Re_τ=80 (a) and 180 (b) and for the edge regime for Re_τ = 80 (c) and 180 (d). Blue : iso-u'=-0.5. Red : iso-u'=+0.5 (edge +0.1). Grey : iso-Q=7 (edge 0.03). Flow in the positive x direction.

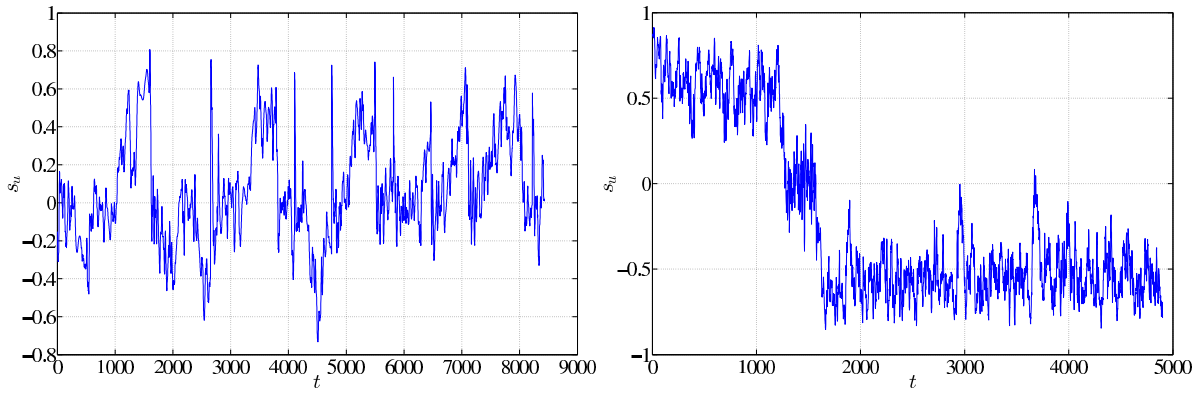

Figure 3. Typical turbulent time series of $s_u(t)$ for Re_τ=80 (left) and 180 (right).

$2T$. At each instant, the non-trivial flow activity is also localised near one wall as in the turbulent regime. It was verified that this feature is independent of the initial condition in the edge bisection algorithm. Along one period, the low-speed streak travels down-

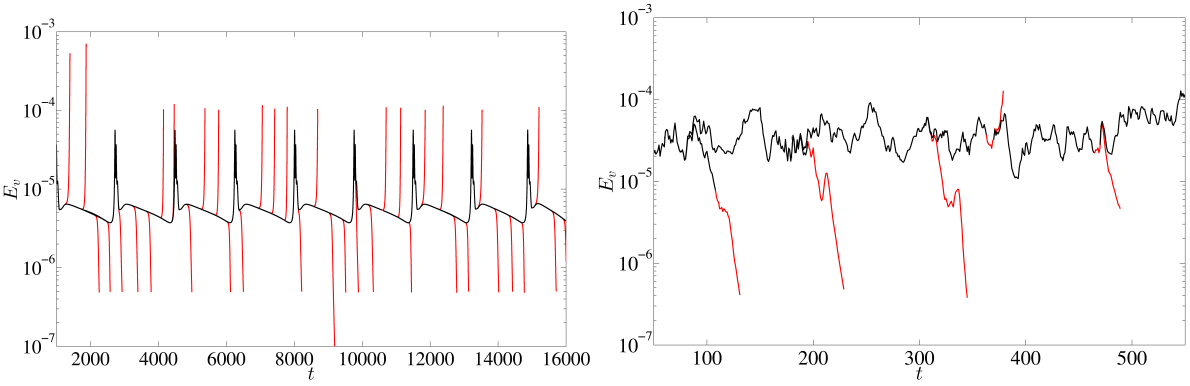

Figure 4. Black lines : Wall-normal energy signal $E_v(t)$ for the edge state at Re_τ=80 (left) and 180 (right). Red lines : $E_v(t)$ for trajectories bracketing the edge trajectory, all generated during the bisection process.

stream while the streamwise vortices on its sides grow in amplitude. When the vortices become strong enough, they cross and push fluid down rather than lift it up, turning the low-speed streak into a high-speed one. Consequently, the whole structure moves also in z by half a spanwise wavelength (therefore the value $\sigma_z = L_z/2$) before the cycle starts again. A completely similar dynamics has been already identified for edge states in fixed mass flux channels (Toh & Itano 2003, Zammert & Eckhardt 2014, Rawat et al. 2014) as well as in the asymptotic suction boundary layer flow (Kreilos et al. 2013, Khapko et al. 2013, Khapko et al. 2016) -but not in plane Couette or cylindrical pipe flow. Scrutizing the chaotic dynamics of edge states for $Re_\tau \geq 100$ reveals a similar sequence of events yet with the time periodicity lost. In one of the cases ($Re_\tau = 100$), a reversal analogous to the ones found in the turbulent regime was observed. It is likely that longer edge tracking in these chaotic regimes would result in more reversal events, whereas reversals have not been observed in the time-periodic case.

Phase portraits in (s_u, s_v, s_w) for turbulent trajectories are displayed in Fig. 5, together with the edge states of the system. A typical organisation of the state space emerges using these variables : two connected symmetry-related blobs appear for either $s_u,\ s_v,\ s_w > 0$ or < 0. The two symmetry-related edge states bound the turbulent dynamics. Finally, the laminar state lies at the origin $\boldsymbol{s} = (0, 0, 0)$ together with all possible states satisfying $\boldsymbol{s} = 0$. The density of points is high near $\boldsymbol{s} = 0$ suggesting that the origin attracts many trajectories before repelling them away to one of the two wells. Strictly speaking, because turbulent lifetimes appear finite (see Fig. 1), the only true attractor in the system is the laminar base flow which also lies at $s_u = s_v = s_v = 0$.

In a deterministic context, the recurrent visits to the subspace $\boldsymbol{s} = 0$ suggest the presence of exact solutions characterised by a relatively small number of unstable directions. The simplest solutions are travelling waves of the form $\boldsymbol{u}(x, y, z, t) = \boldsymbol{u}_{TW}(x - ct, y, z)$, given the equivariance of Eq. (1) with respect to streamwise transla-

tions and the net global advection. A long turbulent signal at $Re_\tau = 80$ was carefully analysed by monitoring $r(t, \Delta x) = |\boldsymbol{u}(x + \Delta x, y, z, t) - \boldsymbol{u}(x, y, z, t + \Delta t)|$ as in (Duguet et al. 2008, Gibson et al. 2008). A clear minimum of r was identified over an interval of values of t with a duration of ≈ 200 time units. The associated velocity field was converged easily using the Newton-Krylov algorithm into an exact travelling wave (TW) solution. Monitoring the state-space distance $d(t) = dist(\boldsymbol{X}(t), \boldsymbol{u}_{TW})$ to the TW along the original turbulent trajectory in Fig. 6 also shows a strong dip near $t \approx 1530$. This demonstrates that the neighbourhood of the TW is indeed visited by the original trajectory. The associated time series of $s_u(t)$ during this visit demonstrates that the time of closest approach coincides with the change of sign of s_u. This suggests that the visit to the exact solution occurs during a reversal. The resulting exact travelling wave solution has a three-dimensional structure displayed in Fig. 7, a phase velocity $c = 0.295$ in units of u_{cl}, and no propagation in z. It consists of streaks located at both walls. It satisfies exactly $\boldsymbol{s} = 0$ whereas the M_y symmetry defined in Eq. (11) is not exactly satisfied as $|M_y\boldsymbol{u} - \boldsymbol{u}|/|\boldsymbol{u}| \approx 2.10^{-3}$ using the energy norm. The stability of the travelling wave has been investigated using an Arnoldi algorithm with an observation time $T = 20$. The complex eigenspectrum is displayed in Fig. 8, where the ansatz $e^{\lambda t}$ has been used (so that an unstable eigenvalue λ satisfies $\mathrm{Re}(\lambda)>0$). As anticipated, it possesses a small number of unstable eigenvalues : only 11 unstable eigenvalues, including 3 real ones and 4 pairs of complex conjugate eigenvalues. It cannot be an edge state itself, which would require only one single real eigenvalue. It was checked by perturbing along each eigendirection with either sign that no trajectory was directly connected to the laminar state. This shows that the solution is not embedded in a more complicated edge state either, at least when no discrete symmetry is imposed as is the case here. Each associated eigenfunction breaks the approximate $\boldsymbol{s} = 0$ symmetry. Perturbing the travelling wave solution in one of its unstable directions thus leads either to turbulence at the top wall ($s_u > 0$) or at the bottom wall ($s_u < 0$). The flow rate (not shown) is relatively low during the approach to the $\boldsymbol{s} = 0$ subspace, suggesting a high activity, whereas the edge is characterised by low perturbation energy and higher flow rate. This also excludes the hypothesis that the approach to the TW corresponds to so-called hibernation events (Xi & Graham 2010). Several other (symmetric) travelling wave solutions have been recently identified numerically, among them (Nagata & Deguchi 2013, Gibson & Brand 2014, Park & Graham 2015, Wall & Nagata 2016). Proper continuation in parameter space would be required to claim that these are the same solutions as the one identified here.

4. Self-similarity of exact solutions

As mentioned in the introduction, while the original focus of the search for exact solutions of the Navier-Stokes equation in wall-bounded shear flows was on near-wall streaks, it shifted mainly towards large-scale structures (of size comparable to outer scales $O(h)$).

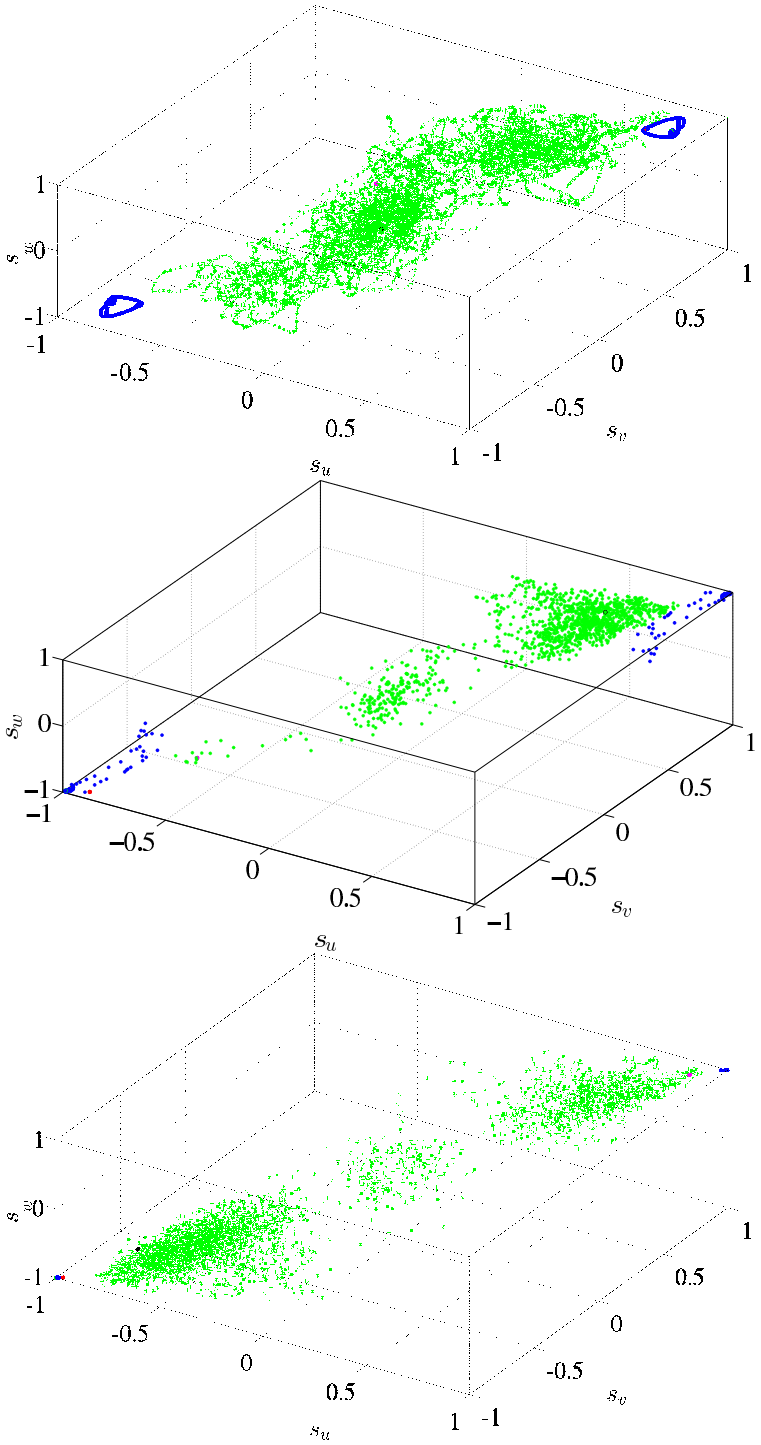

Figure 5. Phase portraits using (s_u, s_v, s_w) variables for Re_τ=80 (top), 150 (middle) and 180 (bottom). Green : turbulent trajectory, blue : edge state. Trajectories are sampled every time unit h/u_{cl}.

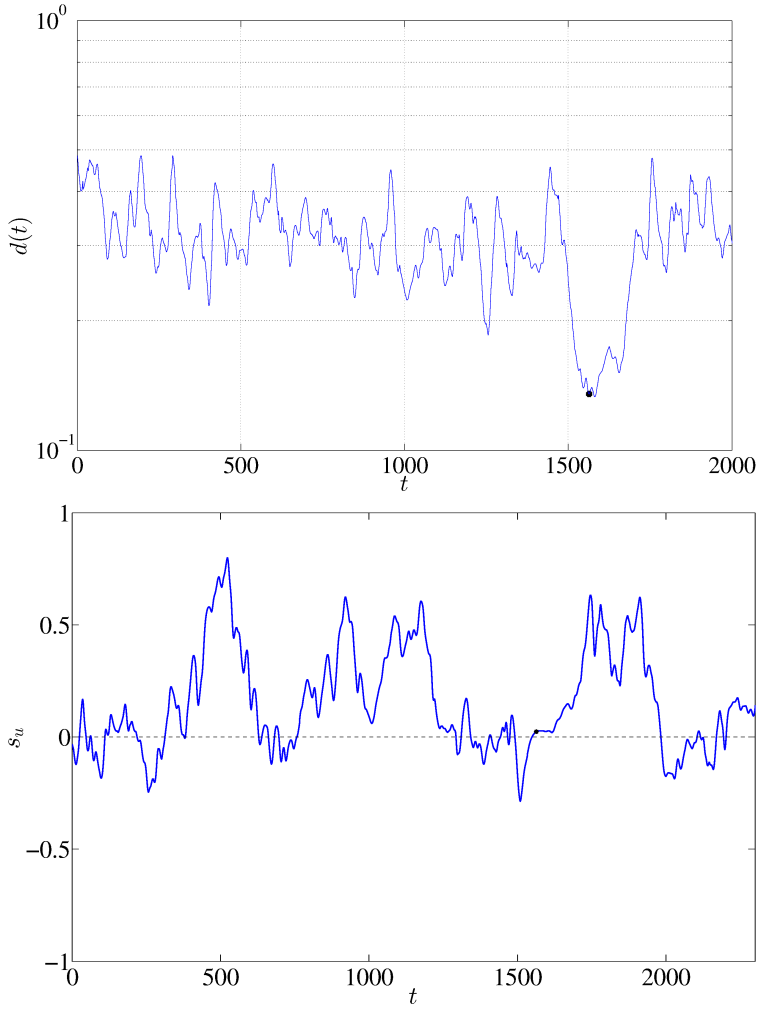

Figure 6. Top : State space distance $d(t)$ to the TW solution along the visiting trajectory (blue). Bottom : associated time series of $s_u(t)$. The filled black circle at $t \approx 1530$ in both plots corresponds to the global minimum of $r(t, 1)$ and also indicates the initial condition for the Newton algorithm.

Steady states of minimal plane Couette flow, which are actually edge states, were successfully continued towards increasing Re in a numerical domain with dimensions fixed in units of h (Wang et al. 2007). Most Re-continuations by Zammert & Eckhardt in Poiseuille flow were also performed inside a periodic domain of size $O(h)$ (Zammert & Eckhardt 2015). There have been efforts to continue exact solutions by considering a fixed domain but modifying locally the wavelength, though the process is mainly applicable to spatially localised solutions (Gibson & Brand 2014). More recently, (Rawat et al. 2015) suggested continuation of an upper branch steady state of plane Couette flow in Re_τ (rather than in the bulk Reynolds number) by imposing L_x^+ and L_z^+ fixed in inner units. This state satisfies for all values of Re_τ the so-called shift-and-reflect symmetry and would verify $\boldsymbol{s} = 0$ according to the current notations. Although continuation was successful, the mean velocity profiles obtained did not exhibit any self-similarity,

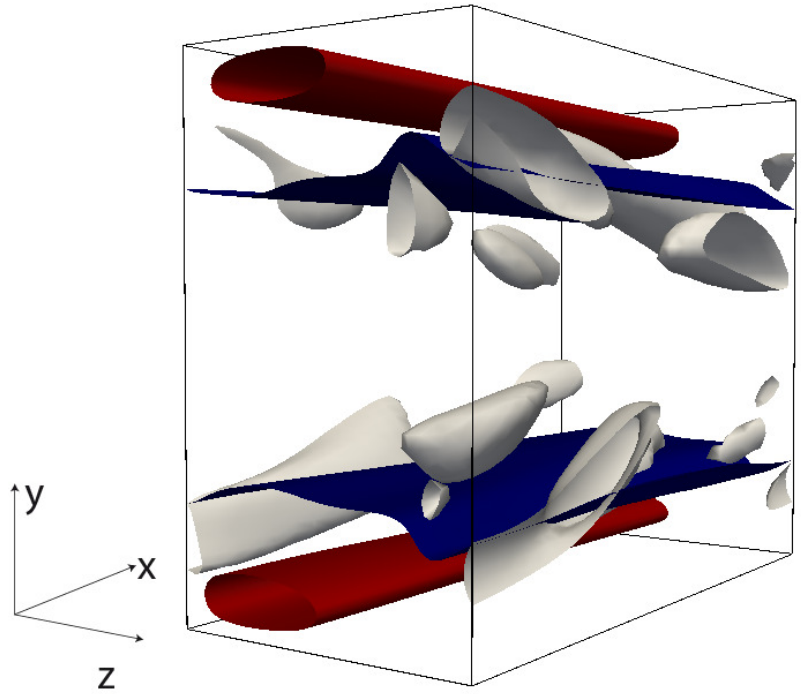

Figure 7. Three-dimensional visualisation of the travelling wave solution. $Re_\tau = 80$. Blue : iso-u'=-0.5. Red : iso-u'=+0.04 Grey : iso-Q=0.15

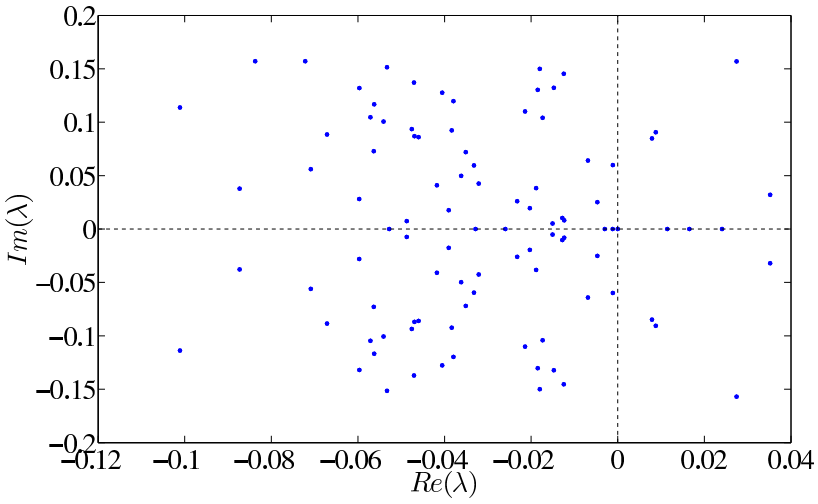

Figure 8. Eigenspectrum of the linearised problem around the travelling wave solution. $Re_\tau = 80$. Unstable eigenvalues lie in the right half-plane.

indicating that the 'natural' scaling of such solutions was rather with outer units $O(h)$. In the present investigation we have identified a nearly-symmetric travelling wave as well as several non-symmetric equilibrium regimes with unsteady dynamics, namely the turbulent and edge regimes. Whereas we expect the nearly-symmetric travelling wave to obey a scaling similar to the findings of Rawat *et al* for plane Couette flow, the wall-localisation of asymmetric solutions highly suggests that an $O(l_\nu)$ scaling could still be

relevant. We verify in Fig. 9, although it is a well-established fact, that the turbulent regime in the MFU scales in inner units. This is accomplished by conditionally averaging in time the streamwise velocity profiles that are localised on one given wall (with the practical condition $s_u > 0.2$). It is clear from Fig. 9, 10 and 11, that if the maximum u_{max} of u is located at $y = y_{max}(Re_\tau)$, y^+_{max} is roughly independent of Re_τ even for the low values of Re_τ investigated here. A similar analysis was performed for the edge states for the same values of Re_τ. The results appear at first sight mixed : for instance no clear unique value of y^+_{max} emerges from this parametric study, and no clear unique value of y_{max} either, see Figs. 12, 13. Instead the results point towards a mixed scaling relation. $u^+_{max}(Re_\tau)$ varies over a range from 1 to 2 as Re_τ varies by a factor of 3, whereas $u_{max}(Re_\tau)$ varies by a factor from 1 to 6, which still favours a $O(l_\nu)$ scaling. What stands out, however, is the comparison with the results of (Rawat et al. 2015), for which the $O(l_\nu)$ scaling is completely ruled out for a similar range of values of Re_τ. Clearly the y-localised solutions with $\boldsymbol{s} \neq 0$ obey a scaling different from that for the solutions with $\boldsymbol{s} = 0$. Furthermore, if the main difference between the present edge states and the solutions of Rawat *et al* is the property of y-localisation, the fact that this localisation property becomes only evident for increasing Re_τ suggests this investigation should be pushed to higher values of Re_τ (requiring an increase of resolution in the y direction). Recent results in this direction for steady solutions of plane Couette flow have appeared this year (Zammert & Eckhardt 2017). We deduce from the present analysis that y-localised equilibrium regimes, unlike statistically symmetric ones, scale either with inner units or with a composite outer/inner units, keeping in mind that this hypothesis requires higher values of Re_τ for confirmation. This finding is important for anyone desiring to push the investigation of the state space towards higher Reynolds numbers.

5. Conclusions

The present investigation of a Minimal Flow Unit (MFU) of pressure-driven plane Poiseuille flow has shown interesting features. The state space seems organised around two repelling turbulent regimes that are related by a reflection about the mid-plane. The observed reversals involve visits to the $s = 0$ subspace built around one -or several- exact unstable solution(s). One such solution was identified by recurrence analysis in the form of a (nearly) symmetric travelling wave solution. This solution is not an edge state and its unstable eigenvectors all break the $s = 0$ symmetry, separating the state space into two symmetric basins (noting that trajectories can also escape from these basins within a finite time). Finally, self-similarity analysis suggests that the y-localised regimes typical of the MFU do not scale in bare outer units for increasing Re_τ. Instead a composite scaling involving both outer and inner units would seem more relevant but requires confirmation at much higher values of Re_τ. This investigation should be seen as preliminary as it leaves many questions unanswered. From a dynamical point of view,

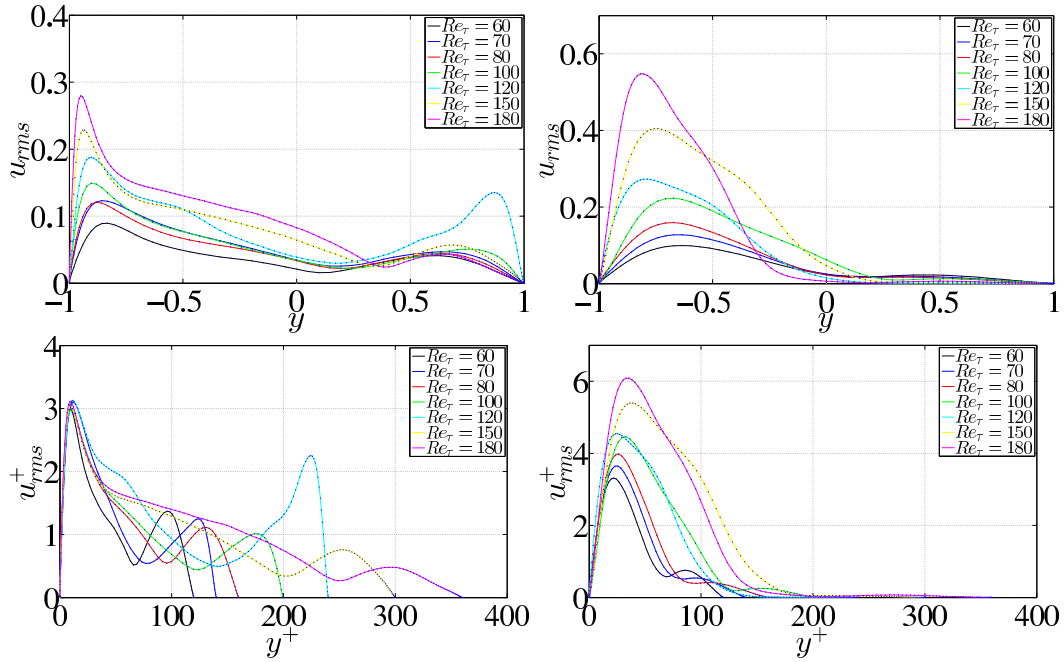

Figure 9. Mean conditional streamwise velocity profiles parametrised by Re_τ for the turbulent regime in outer units (top left) and inner units (bottom left), and for the edge regime in outer units (top right) and inner units (bottom right).

many other invariant sets are expected to populate the phase space, among them other travelling waves, periodic orbits and connections between them (Cvitanović 2013). From a mechanical point of view, why does confinement by the periodic boundary conditions lead to turbulent activity being restrained to one wall only? Could a statistical analysis reveal more about the different possible ways to achieve symmetry reversals? The fate of these solutions in the asymptotic limit $Re_\tau \to \infty$ is also of interest. Presumably, the increasing localisation property could allow new solutions in the high-Re_τ limit to be constructed, by combining nonlinearly different solutions with different localisation properties. If so, this would make MFU solutions relevant even in numerical domains that are not laterally confined. We hope that this preliminary study will trigger new developments in these directions.

S.A.N. would like to thank the French Ministère de l'Education, de la Recherche et de l'Enseignement Supérieur for the doctoral grant. Stefan Zammert is gratefully acknowledged for useful discussions. J. F. Gibson is also acknowledged for developing and sharing his code channeflow.org.

References

Coffey W, Kalmykov Y P & Waldron J 2004 *Chemistry and Electrical Engineering. World Scientific* .
Cvitanović P 2013 *Journal of Fluid Mechanics* **726**, 1–4.
Duguet Y, Willis A P & Kerswell R R 2008 *Journal of Fluid Mechanics* **613**, 255–274.

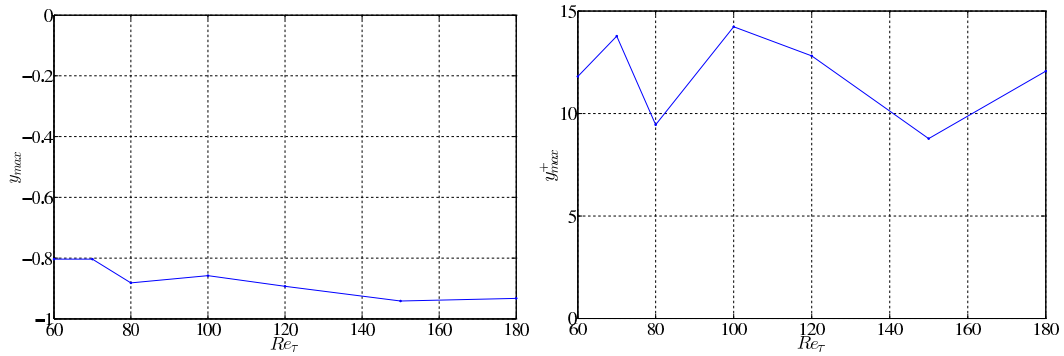

Figure 10. Dependence of y_{max} on Re_τ in outer (left) and inner units (right) for the turbulent regime.

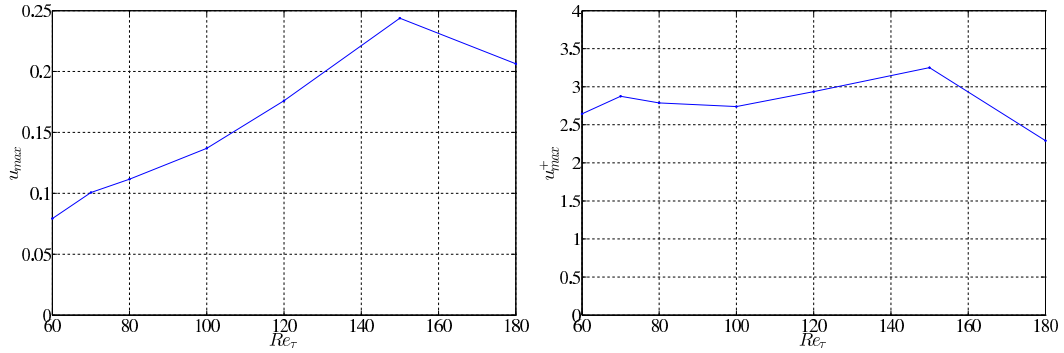

Figure 11. Dependence of u_{max} on Re_τ in outer (left) and inner units (right) for the turbulent regime.

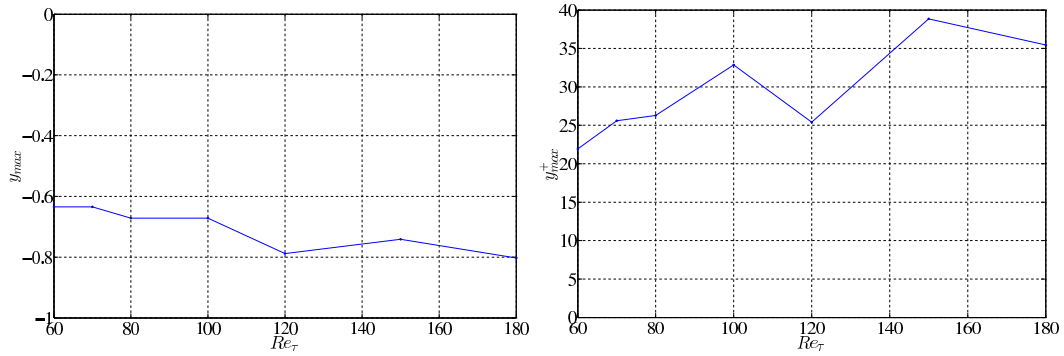

Figure 12. Dependence of y_{max} on Re_τ in outer (left) and inner units (right) for the edge regime.

Eckhardt B, Faisst H, Schmiegel A & Schneider T M 2008 *Phil. Trans. R. Soc. A* **366**, 1297–1315.
Gibson J F 2008 'Channelflow: a spectral navier-stokes simulator in c++'.
Gibson J F & Brand E 2014 *Journal of Fluid Mechanics* **745**, 25–61.
Gibson J F, Halcrow J & Cvitanović P 2008 *Journal of Fluid Mechanics* **611**, 107–130.
Hamilton J M, Kim J & Waleffe F 1995 *Journal of Fluid Mechanics* **287**, 317–348.
Hof B, de Lozar A, Kuik D J & Westerweel J 2008 *Phys. Rev. Lett.* **101**(21), 214501.
Hwang Y & Bengana Y 2016 *Journal of Fluid Mechanics* **795**, 708–738.
Hwang Y & Cossu C 2010 *Physical review letters* **105**(4), 044505.

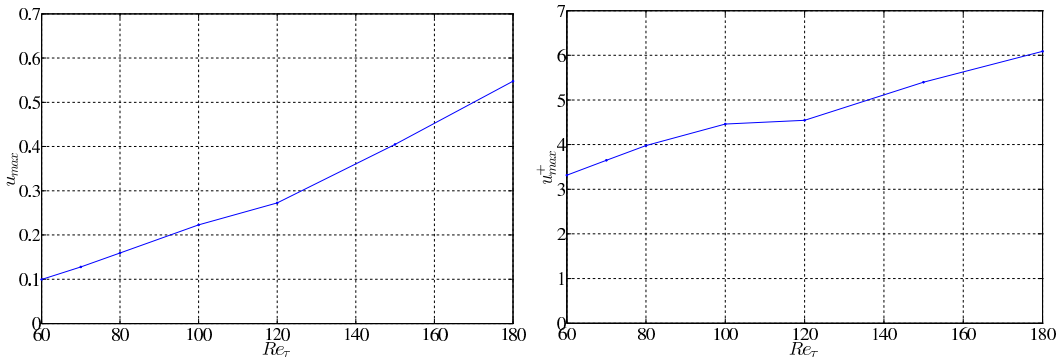

Figure 13. Dependence of u_{max} on Re_τ in outer (left) and inner units (right) for the edge regime.

Hwang Y, Willis A P & Cossu C 2016 *Journal of Fluid Mechanics* **802**, R1–1.

Jiménez J, Kawahara G, Simens M P, Nagata M & Shiba M 2005 *Physics of Fluids (1994-present)* **17**(1), 015105.

Jiménez J & Moin P 1991 *Journal of Fluid Mechanics* **225**, 213–240.

Jiménez J & Pinelli A 1999 *J. Fluid Mech* **389**, 335359.

Kawahara G & Kida S 2001 *Journal of Fluid Mechanics* **449**, 291–300.

Kawahara G, Uhlmann M & van Veen L 2012 *Annu. Rev. Fluid Mech.* **44**, 203–225.

Khapko T, Kreilos T, Schlatter P, Duguet Y, Eckhardt B & Henningson D S 2013 *Journal of Fluid Mechanics* **717**, R6.

Khapko T, Kreilos T, Schlatter P, Duguet Y, Eckhardt B & Henningson D S 2016 *Journal of Fluid Mechanics* **801**, R2.

Kreilos T, Veble G, Schneider T M & Eckhardt B 2013 *Journal of Fluid Mechanics* **726**, 100–122.

Mathis R, Hutchins N & Marusic I 2009 *Journal of Fluid Mechanics* **628**, 311–337.

Nagata M & Deguchi K 2013 *Journal of Fluid Mechanics* **735**, R4.

Park J & Graham M 2015 *J. Fluid Mech* **782**, 430–454.

Rawat S, Cossu C, Hwang Y & Rincon F 2015 *Journal of Fluid Mechanics* **782**, 515–540.

Rawat S, Cossu C & Rincon F 2014 *Comptes Rendus Mécanique* **342**(8), 485–489.

Schneider T M, Eckhardt B & Yorke J A 2007 *Physical review letters* **99**(3), 034502.

Skufca J D, Yorke J A & Eckhardt B 2006 *Physical review letters* **96**(17), 174101.

Toh S & Itano T 2003 *Journal of Fluid Mechanics* **481**, 67–76.

Townsend A A 1980 *The structure of turbulent shear flow* Cambridge university press.

Viswanath D 2007 *Journal of Fluid Mechanics* **580**, 339–358.

Waleffe F 1997 *Phys. Fluids* **9**, 883–900.

Wall D & Nagata M 2016 *Journal of Fluid Mechanics* **788**, 444–468.

Wang J, Gibson J & Waleffe F 2007 *Physical review letters* **98**(20), 204501.

Willis A P, Cvitanović P & Avila M 2013 *Journal of Fluid Mechanics* **721**, 514–540.

Xi L & Graham M D 2010 *Physical review letters* **104**(21), 218301.

Zammert S & Eckhardt B 2014 *Fluid Dynamics Research* **46**(4), 041419.

Zammert S & Eckhardt B 2015 *Physical Review E* **91**(4), 041003.

Zammert S & Eckhardt B 2017 Coherent structures in boundary layers in the quasilinear approximation. Recurrence, Self-Organization, and the Dynamics Of Turbulence, Santa Barbara, KITP, January 2017.

Bibliography

[1] J. Jiménez and P. Moin, "The minimal flow unit in near-wall turbulence," *Journal of Fluid Mechanics*, vol. 225, pp. 213–240, 4 1991.

[2] O. Reynolds, "An experimental investigation of the circumstances which determine whether the motion of water shall be direct or sinuous, and of the law of resistance in parallel channels.," *Proceedings of the Royal Society of London*, vol. 35, no. 224-226, pp. 84–99, 1883.

[3] D. R. Carlson, S. E. Widnall, and M. F. Peeters, "A flow-visualization study of transition in plane Poiseuille flow," *Journal of Fluid Mechanics*, vol. 121, pp. 487–505, 1982.

[4] F. Alavyoon, D. S. Henningson, and P. H. Alfredsson, "Turbulent spots in plane Poiseuille flow–flow visualization," *Physics of Fluids (1958-1988)*, vol. 29, no. 4, pp. 1328–1331, 1986.

[5] M. Sano and K. Tamai, "A universal transition to turbulence in channel flow," *Nature Physics*, 2016.

[6] G. Lemoult, K. Gumowski, J.-L. Aider, and J. E. Wesfreid, "Turbulent spots in channel flow: An experimental study," *The European Physical Journal E*, vol. 37, no. 4, pp. 1–11, 2014.

[7] P. J. Schmid and D. S. Henningson, *Stability and transition in shear flows*, vol. 142. Springer Science & Business Media, 2012.

[8] F. Waleffe, "On a self-sustaining process in shear flows," *Physics of Fluids (1994-present)*, vol. 9, no. 4, pp. 883–900, 1997.

[9] T. Kreilos, *Turbulence Transition in Shear Flows and Dynamical Systems Theory*. PhD thesis, Philipps-Universitat Marburg, 2014.

[10] P. Cvitanović, R. Artuso, R. Mainieri, G. Tanner, and G. Vattay, *Chaos: Classical and Quantum*. Copenhagen: Niels Bohr Inst., 2016.

[11] A. P. Willis, K. Y. Short, and P. Cvitanović, "Symmetry reduction in high dimensions, illustrated in a turbulent pipe," *Physical Review E*, vol. 93, no. 2, p. 022204, 2016.

[12] C. C. Pringle, Y. Duguet, and R. R. Kerswell, "Highly symmetric travelling waves in pipe flow," *Philosophical Transactions of the Royal Society of London A: Mathematical, Physical and Engineering Sciences*, vol. 367, no. 1888, pp. 457–472, 2009.

[13] T. Khapko, *Edge states and transition to turbulence in boundary layers*. PhD thesis, KTH Royal Institute of Technology, 2016.

[14] J. F. Gibson, J. Halcrow, and P. Cvitanović, "Visualizing the geometry of state space in plane Couette flow," *Journal of Fluid Mechanics*, vol. 611, pp. 107–130, 009 2008.

[15] A. Lozano-Durán and J. Jiménez, "Time-resolved evolution of coherent structures in turbulent channels: characterization of eddies and cascades," *Journal of Fluid Mechanics*, vol. 759, pp. 432–471, 2014.

[16] Y. Hwang, "Statistical structure of self-sustaining attached eddies in turbulent channel flow," *Journal of Fluid Mechanics*, vol. 767, pp. 254–289, 2015.

[17] S. Rawat, C. Cossu, Y. Hwang, and F. Rincon, "On the self-sustained nature of large-scale motions in turbulent Couette flow," *Journal of Fluid Mechanics*, vol. 782, pp. 515–540, 10 2015.

[18] J. L. M. Poiseuille *et al.*, *Experimental investigations upon the flow of liquids in tubes of very small diameter*, vol. 1. 1840.

[19] J. L. M. Poiseuille *et al.*, "Recherches expérimentales sur le mouvement des liquides dans les tubes de très petits diamètres," *Comptes Rend., Paris*, 1840.

[20] R. R. Kerswell, "Recent progress in understanding the transition to turbulence in a pipe," *Nonlinearity*, vol. 18, no. 6, p. R17, 2005.

[21] K. Avila, D. Moxey, A. de Lozar, M. Avila, D. Barkley, and B. Hof, "The onset of turbulence in pipe flow," *Science*, vol. 333, no. 6039, pp. 192–196, 2011.

[22] T. Tsukahara, Y. Seki, H. Kawamura, and D. Tochio, "DNS of turbulent channel flow at very low reynolds numbers," in *TSFP DIGITAL LIBRARY ONLINE*, Begel House Inc., 2005.

[23] Y. Duguet and P. Schlatter, "Oblique laminar-turbulent interfaces in plane shear flows," *Physical review letters*, vol. 110, no. 3, p. 034502, 2013.

[24] M. Chantry, L. S. Tuckerman, and D. Barkley, "Turbulent–laminar patterns in shear flows without walls," *Journal of Fluid Mechanics*, vol. 791, p. R8, 2016.

[25] P. Drazin and L. Howard, "Hydrodynamic stability of parallel flow of inviscid fluid," *Advances in applied mechanics*, vol. 9, pp. 1–89, 1966.

[26] S. A. Orszag, "Accurate solution of the Orr-Sommerfeld stability equation," *Journal of Fluid Mechanics*, vol. 50, no. 04, pp. 689–703, 1971.

[27] T. Chen and D. Joseph, "Subcritical bifurcation of plane Poiseuille flow," *Journal of Fluid Mechanics*, vol. 58, no. 02, pp. 337–351, 1973.

[28] J.-P. Zahn, J. Toomre, E. Spiegel, and D. Gough, "Nonlinear cellular motions in Poiseuille channel flow," *Journal of Fluid Mechanics*, vol. 64, no. 02, pp. 319–346, 1974.

[29] J. Jimenez, "Transition to turbulence in two-dimensional Poiseuille flow," *Journal of Fluid Mechanics*, vol. 218, pp. 265–297, 1990.

[30] I. Soibelman and D. I. Meiron, "Finite-amplitude bifurcations in plane Poiseuille flow: two-dimensional Hopf bifurcation," *Journal of Fluid Mechanics*, vol. 229, pp. 389–416, 1991.

[31] Y. Duguet, C. C. Pringle, and R. R. Kerswell, "Relative periodic orbits in transitional pipe flow," *Physics of Fluids (1994-present)*, vol. 20, no. 11, p. 114102, 2008.

[32] A. P. Willis, P. Cvitanović, and M. Avila, "Revealing the state space of turbulent pipe flow by symmetry reduction," *Journal of Fluid Mechanics*, vol. 721, pp. 514–540, 4 2013.

[33] E. Hopf, "A mathematical example displaying features of turbulence," *Communications on Pure and Applied Mathematics*, vol. 1, no. 4, pp. 303–322, 1948.

[34] B. Eckhardt, T. M. Schneider, B. Hof, and J. Westerweel, "Turbulence transition in pipe flow," *Annu. Rev. Fluid Mech.*, vol. 39, pp. 447–468, 2007.

[35] B. Hof, C. W. van Doorne, J. Westerweel, F. T. Nieuwstadt, H. Faisst, B. Eckhardt, H. Wedin, R. R. Kerswell, and F. Waleffe, "Experimental observation of nonlinear traveling waves in turbulent pipe flow," *Science*, vol. 305, no. 5690, pp. 1594–1598, 2004.

[36] E. Ott, *Chaos in dynamical systems*. Cambridge university press, 2002.

[37] G. Kawahara and S. Kida, "Periodic motion embedded in plane couette turbulence: regeneration cycle and burst," *Journal of Fluid Mechanics*, vol. 449, pp. 291–300, 2001.

[38] M. Nagata, "Three-dimensional finite-amplitude solutions in plane couette flow: bifurcation from infinity," *J. Fluid Mech*, vol. 217, pp. 519–527, 1990.

[39] U. Ehrenstein and W. Koch, "Three-dimensional wavelike equilibrium states in plane Poiseuille flow," *Journal of fluid mechanics*, vol. 228, pp. 111–148, 1991.

[40] F. Waleffe, "Exact coherent structures in channel flow," *Journal of Fluid Mechanics*, vol. 435, pp. 93–102, 06 2001.

[41] F. Waleffe, "Homotopy of exact coherent structures in plane shear flows," *Physics of Fluids (1994-present)*, vol. 15, no. 6, pp. 1517–1534, 2003.

[42] M. Nagata and K. Deguchi, "Mirror-symmetric exact coherent states in plane Poiseuille flow," *Journal of Fluid Mechanics*, vol. 735, p. R4, 2013.

[43] E. Brand and J. F. Gibson, "A doubly localized equilibrium solution of plane couette flow," *Journal of Fluid Mechanics*, vol. 750, p. R3 (12 pages), 7 2014.

[44] S. Zammert and B. Eckhardt, "Periodically bursting edge states in plane Poiseuille flow," *Fluid Dynamics Research*, vol. 46, no. 4, p. 041419, 2014.

[45] S. Zammert and B. Eckhardt, "Streamwise and doubly-localised periodic orbits in plane Poiseuille flow," *Journal of Fluid Mechanics*, vol. 761, pp. 348–359, 2014.

[46] S. Rawat, C. Cossu, and F. Rincon, "Relative periodic orbits in plane Poiseuille flow," *Comptes Rendus Mécanique*, vol. 342, no. 8, pp. 485–489, 2014.

[47] J. D. Skufca, J. A. Yorke, and B. Eckhardt, "Edge of chaos in a parallel shear flow," *Physical review letters*, vol. 96, no. 17, p. 174101, 2006.

[48] J. M. Hamilton, J. Kim, and F. Waleffe, "Regeneration mechanisms of near-wall turbulence structures," *Journal of Fluid Mechanics*, vol. 287, pp. 317–348, 04 2006.

[49] T. Itano and S. Toh, "The dynamics of bursting process in wall turbulence," *Journal of the Physical Society of Japan*, vol. 70, no. 3, pp. 703–716, 2001.

[50] T. M. Schneider, J. F. Gibson, M. Lagha, F. De Lillo, and B. Eckhardt, "Laminar-turbulent boundary in plane couette flow," *Physical Review E*, vol. 78, no. 3, p. 037301, 2008.

[51] Y. Duguet, P. Schlatter, and D. S. Henningson, "Localized edge states in plane couette flow," *Physics of Fluids (1994-present)*, vol. 21, no. 11, p. 111701, 2009.

[52] T. M. Schneider, D. Marinc, and B. Eckhardt, "Localized edge states nucleate turbulence in extended plane couette cells," *Journal of Fluid Mechanics*, vol. 646, pp. 441–451, 2010.

[53] Y. Duguet, A. P. Willis, and R. R. Kerswell, "Transition in pipe flow: the saddle structure on the boundary of turbulence," *Journal of Fluid Mechanics*, vol. 613, pp. 255–274, 2008.

[54] Y. Duguet, A. Willis, and R. Kerswell, "Slug genesis in cylindrical pipe flow," *Journal of Fluid Mechanics*, vol. 663, pp. 180–208, 2010.

[55] S. Toh and T. Itano, "A periodic-like solution in channel flow," *Journal of Fluid Mechanics*, vol. 481, pp. 67–76, 04 2003.

[56] T. M. Schneider, B. Eckhardt, and J. A. Yorke, "Turbulence transition and the edge of chaos in pipe flow," *Physical review letters*, vol. 99, no. 3, p. 034502, 2007.

[57] Y. Duguet, P. Schlatter, D. S. Henningson, and B. Eckhardt, "Self-sustained localized structures in a boundary-layer flow," *Physical review letters*, vol. 108, no. 4, p. 044501, 2012.

[58] S. Cherubini, P. De Palma, J.-C. Robinet, and A. Bottaro, "Edge states in a boundary layer," *Physics of Fluids (1994-present)*, vol. 23, no. 5, p. 051705, 2011.

[59] T. Khapko, T. Kreilos, P. Schlatter, Y. Duguet, B. Eckhardt, and D. S. Henningson, "Localized edge states in the asymptotic suction boundary layer," *Journal of Fluid Mechanics*, vol. 717, 002 2013.

[60] T. Khapko, T. Kreilos, P. Schlatter, Y. Duguet, B. Eckhardt, and D. S. Henningson, "Edge states as mediators of bypass transition in boundary-layer flows," *Journal of Fluid Mechanics*, vol. 801, 007 2016.

[61] P. Cvitanović, "Recurrent flows: the clockwork behind turbulence," *Journal of Fluid Mechanics*, vol. 726, pp. 1–4, 2013.

[62] B. Eckhardt, H. Faisst, A. Schmiegel, and T. M. Schneider, "Dynamical systems and the transition to turbulence in linearly stable shear flows," *Philosophical Transactions of the Royal Society of London A: Mathematical, Physical and Engineering Sciences*, vol. 366, no. 1868, pp. 1297–1315, 2008.

[63] G. Kawahara, M. Uhlmann, and L. Van Veen, "The significance of simple invariant solutions in turbulent flows," *arXiv preprint arXiv:1108.0975*, 2011.

[64] J. C. Del Álamo, J. Jimenez, P. Zandonade, and R. D. Moser, "Self-similar vortex clusters in the turbulent logarithmic region," *Journal of Fluid Mechanics*, vol. 561, pp. 329–358, 2006.

[65] A. A. Townsend, *The structure of turbulent shear flow*. Cambridge university press, 1980.

[66] A. Perry, S. Henbest, and M. Chong, "A theoretical and experimental study of wall turbulence," *Journal of Fluid Mechanics*, vol. 165, pp. 163–199, 1986.

[67] C. D. Tomkins and R. J. Adrian, "Spanwise structure and scale growth in turbulent boundary layers," *Journal of Fluid Mechanics*, vol. 490, pp. 37–74, 2003.

[68] O. Flores, J. Jimenez, and J. C. Del Alamo, "Vorticity organization in the outer layer of turbulent channels with disturbed walls," *Journal of Fluid Mechanics*, vol. 591, pp. 145–154, 2007.

[69] J. H. Lee, H. J. Sung, and P.-Å. Krogstad, "Direct numerical simulation of the turbulent boundary layer over a cube-roughened wall," *Journal of Fluid Mechanics*, vol. 669, pp. 397–431, 2011.

[70] Y. Hwang and C. Cossu, "Self-sustained process at large scales in turbulent channel flow," *Physical review letters*, vol. 105, no. 4, p. 044505, 2010.

[71] Y. Hwang and C. Cossu, "Self-sustained processes in the logarithmic layer of turbulent channel flows," *Physics of Fluids (1994-present)*, vol. 23, no. 6, p. 061702, 2011.

[72] C. Smith and S. Metzler, "The characteristics of low-speed streaks in the near-wall region of a turbulent boundary layer," *Journal of Fluid Mechanics*, vol. 129, pp. 27–54, 1983.

[73] J. F. Gibson, "Channelflow: A spectral Navier-Stokes simulator in C++," tech. rep., U. New Hampshire, 2014. `Channelflow.org`.

[74] D. Viswanath, "Recurrent motions within plane couette turbulence," *Journal of Fluid Mechanics*, vol. 580, pp. 339–358, 2007.

[75] P. Cvitanović, D. Borrero-Echeverry, K. M. Carroll, B. Robbins, and E. Siminos, "Cartography of high-dimensional flows: A visual guide to sections and slices," *Chaos: An Interdisciplinary Journal of Nonlinear Science*, vol. 22, no. 4, p. 047506, 2012.

[76] N. B. Budanur, P. Cvitanović, R. L. Davidchack, and E. Siminos, "Reduction of so (2) symmetry for spatially extended dynamical systems," *Physical review letters*, vol. 114, no. 8, p. 084102, 2015.

[77] C. W. Rowley and J. E. Marsden, "Reconstruction equations and the karhunen–loève expansion for systems with symmetry," *Physica D: Nonlinear Phenomena*, vol. 142, no. 1, pp. 1–19, 2000.

[78] T. Kreilos, S. Zammert, and B. Eckhardt, "Comoving frames and symmetry-related motions in parallel shear flows," *Journal of Fluid Mechanics*, vol. 751, pp. 685–697, 006 2014.

[79] J. Ahrens, B. Geveci, C. Law, C. Hansen, and C. Johnson, "36-paraview: An end-user tool for large-data visualization," 2005.

[80] V. Kolář, "Vortex identification: New requirements and limitations," *International Journal of Heat and Fluid Flow*, vol. 28, no. 4, pp. 638 – 652, 2007. Including Special Issue of Conference on Modelling Fluid Flow (CMFF'06), Budapest13th event of the international conference series in fluid flow technologies: conference on modelling fluid flow.

[81] R. D. Moser, J. Kim, and N. N. Mansour, "Direct numerical simulation of turbulent channel flow up to re= 590," *Phys. Fluids*, vol. 11, no. 4, pp. 943–945, 1999.

[82] B. Hof, A. de Lozar, D. J. Kuik, and J. Westerweel, "Repeller or attractor? selecting the dynamical model for the onset of turbulence in pipe flow," *Physical review letters*, vol. 101, no. 21, p. 214501, 2008.

[83] T. Kreilos, G. Veble, T. M. Schneider, and B. Eckhardt, "Edge states for the turbulence transition in the asymptotic suction boundary layer," *Journal of Fluid Mechanics*, vol. 726, pp. 100–122, 005 2013.

[84] S. Zammert, *Localized states in the transition to turbulence in plane Poiseuille flow and thermal boundary layers*. PhD thesis, Philipps-Universität Marburg, 2015.

[85] T. Khapko, Y. Duguet, T. Kreilos, P. Schlatter, B. Eckhardt, and D. S. Henningson, "Complexity of localised coherent structures in a boundary-layer flow," *The European Physical Journal E*, vol. 37, no. 4, pp. 1–12, 2014.

[86] F. Mellibovsky, A. Meseguer, T. M. Schneider, and B. Eckhardt, "Transition in localized pipe flow turbulence," *Physical review letters*, vol. 103, no. 5, p. 054502, 2009.

[87] L. Xi and M. D. Graham, "Active and hibernating turbulence in minimal channel flow of newtonian and polymeric fluids," *Physical review letters*, vol. 104, no. 21, p. 218301, 2010.

[88] J. S. Park and M. D. Graham, "Exact coherent states and connections to turbulent dynamics in minimal channel flow," *Journal of Fluid Mechanics*, vol. 782, pp. 430–454, 2015.

[89] D. Wall and M. Nagata, "Exact coherent states in channel flow," *Journal of Fluid Mechanics*, vol. 788, pp. 444–468, 2016.

[90] R. Mathis, N. Hutchins, and I. Marusic, "Large-scale amplitude modulation of the small-scale structures in turbulent boundary layers," *Journal of Fluid Mechanics*, vol. 628, pp. 311–337, 2009.

[91] J. Jiménez and A. Pinelli, "The autonomous cycle of near-wall turbulence. submitted to," *J. Fluid Mech*, 1998.

[92] J. Wang, J. Gibson, and F. Waleffe, "Lower branch coherent states in shear flows: transition and control," *Physical review letters*, vol. 98, no. 20, p. 204501, 2007.

[93] S. Zammert and B. Eckhardt, "Bypass transition and subcritical turbulence in plane Poiseuille flow," in *Proceedings of TSFP-9*, 2015.

université PARIS-SACLAY

ÉCOLE DOCTORALE
Sciences mécaniques et énergétiques, matériaux et géosciences (SMEMAG)

Titre : Étude numérique des régimes turbulents au sein d'un écoulement de Poiseuille plan

Mots clefs : turbulence, canal plan, transition, structures coherentes exactes

Résumé : Cette thèse présente une étude numérique des régimes turbulents au sein d'un écoulement de Poiseuille plan forcé par un gradient de pression constant. L'effort numérique a porté principalement sur le concept d'Unité Minimale.
Dans la première partie, des simulations en régime turbulent ont été conduites en géométrie périodique. Les DNS en Unité Minimale montrent que, l'activité turbulente se trouve localisée à proximité d'une des parois, et que la dynamique aux temps longs s'organise autour de renversements abrupts.
Dans la seconde partie, on recherche par le calcul les états cohérents exactes en particulier les états dits frontière. Ces états frontière, obtenus par dichotomie, sont caractérisés par tourbillons longitudinaux et une paire unique de stries toujours localisées à proximité d'une seule paroi. Des représentations de la dynamique dans l'espace des phases sont reconstruites à l'aide de divers observables. La dynamique d'un renversement s'articule autour de visites transitoires vers un espace de solutions quasi-symétriques. Une onde progressive exacte, instable et quasi-symetrique a ainsi été identifiée. L'analyse de stabilité révèle que ses vecteurs propres séparent l'espace des phases en deux basins distincts.
La dernière partie remet en question l'auto-similarité des différents régimes d'équilibre d'écoulement. Contrairement aux études récentes qui se concentrent sur les solutions à structure symétrique imposée, nos résultats suggèrent que les unités de parois sont également pertinentes pour les états frontière lorsqu'ils sont localisés près d'une paroi, même si l'auto-similarité n'est pas aussi flagrante que pour les régimes turbulents.

Title : Numerical study of transition to turbulence in plane Poiseuille flow

Keywords : turbulence, plane channel, transition, exact coherent structures

Abstract : This thesis numerically investigates the dynamics of turbulence in plane Poiseuille flow driven by a fixed pressure gradient. The focus is especially on computations carried out within the minimal flow unit (M.F.U.).
In the first part, turbulent simulations are carried out in spatially periodic channels. In the M.F.U. simulations, the turbulent activity appears to be localised near one wall and the long term dynamics features abrupt reversals.
In the next part, we look numerically for exact coherent states in the M.F.U. system. Edge states, which are computed using bisection exhibit streamwise vortices and a single pair of streaks localised near only wall at all times. Different state space representations and phase portraits were constructed using appropriately chosen variables. The dynamics along a turbulent reversal is organised around transient visits to a subspace of (almost) symmetric flow fields. A nearly-symmetric exact travelling wave (TW) solution was found in this subspace. Stability analysis of the TW revealed that its unstable eigenvectors separate the state space into two symmetric basins.
In the last part of this thesis, the self-similarity of the different non-trivial equilibrium flow regimes computed in this work, is addressed. Contrarily to most studies focusing on symmetric solutions, the present study suggests that inner scaling is relevant for the description of edge regimes as well although the self-similarity is not as satisfactory as for the turbulent regimes.

Université Paris-Saclay
Espace Technologique / Immeuble Discovery
Route de l'Orme aux Merisiers RD 128 / 91190 Saint-Aubin, France